NUMERICAL SIMULATIONS OF THERMAL SYSTEMS – APPLICATIONS TO FUEL CHEMISTRY, NANOFLUID HEAT TRANSFER AND AEROSOL PARTICLE TRANSPORT

by

Kuang-Chuan Lin

A dissertation submitted in partial fulfillment
of the requirements for the degree of
Doctor of Philosophy
(Mechanical Engineering)
in The University of Michigan
2011

Doctoral Committee:

    Associate Professor Angela Violi, Chair
    Professor Arvind Atreya
    Professor John R. Barker
    Associate Professor Hong G. Im

I dedicate this dissertation to my family, especially…
to Dad, Mom and younger brother Rung for their endless supply of love and support.
to Grandmas, Aunt Gillian, Aunt Jing-Rung for encouragement.

ACKNOWLEDGEMENTS

This dissertation would not have been possible without the help of my dissertation committee members. My deepest gratitude is to Professor Violi, my advisor and committee chair for her patience and guidance from the preliminary to the completion of my Ph.D. study. I'm fortunate to have an advisor who gave me the freedom to explore my own interests and provided me the opportunities to develop the problem-solving skills required for academic success. I want to thank the committee members, Professor Atreya, Professor Barker and Professor Im for their invaluable time and in-depth reviews to help me accomplish this wonderful feat. I would also like to extend my gratitude to Professor Barker. His Air Pollution Chemistry class opened up the world of chemical kinetic modeling to me.

I am heartily thankful to Professor Violi and Professor Pipe for giving me a wonderful opportunity to learn teaching skills by working with them as a Graduate Student Instructor in their Thermodynamics classes. The experience I gained not only made my understanding of thermodynamics greater in depth, but I believe will also enhance my ability to communicate with people.

Finally, I appreciate the Ph.D. fellowship, Graduate Student Research Assistantship and Teaching Assistantship offered by the National Science

Council in Taiwan, Professor Violi's Research Group and Department of Mechanical Engineering, respectively.

Last but not least, I would like to thank everyone who ever helped me during my Ph.D. study at the University of Michigan, Ann Arbor. Also, I want to express my deepest apologies for not thanking everyone individually in this relatively short statement.

TABLE OF CONTENTS

LIST OF FIGURES

LIST OF TABLES

GLOSSARY

CHAPTER 1

Roman symbols

P	Pressure (atm)
T	Temperature (K)
t	Dimensional time (s)

Greek symbols

ϕ	Equivalence ratio
σ	Sensitivity coefficient
τ_{id}	Ignition delay time

Superscripts

*	Dimensionless scale

CHARPTER 2

Roman symbols

c	Empirical constant
c_p	Specific heat at constant pressure (KJ kg^{-1} K^{-1})
D_f	Fractal dimension

d_f	Fluid molecular diameter (m)
d_{avg}	Mean nanoparticle diameter (m)
Gr	Grashof number $g\beta_f\left(T_H^* - T_L^*\right)H^3/\upsilon_f^2$
g	Gravitational acceleration (m s^{-2})
H	Dimensional cavity height (m)
h	Heat convection coefficient (W m^{-2} K^{-1})
k	Thermal conductivity of pure fluid (W m^{-1} K^{-1})
L	Dimensional cavity width (m)
Nu	Local Nusselt number
$\overline{Nu}$	Average Nusselt number
Pr	Prandtl number, υ_f/α_f
R	Ratio of minimum to maximum nanoparticles d_{min}/d_{max}
Ra	Rayleigh number $Pr \cdot Gr$
T	Dimensionless temperature
t	Dimensionless time
u, v	Dimensionless velocity components along (x, y) axes
x, y	Dimensionless Cartesian coordinates

Greek symbols

α	Thermal diffusivity (m^2 s^{-1})
β	Thermal expansion coefficient (K^{-1})
ε, η	Empirical constant
θ	Dependent variables (u, v, p, T, ψ)
ϕ	Solid volume fraction
υ_f	Kinematic viscosity (m^2 s^{-1})

ω	Vorticity (s^{-1})
Ω	Dimensionless vorticity, $\omega H^{2}/\alpha_{f}$
ψ	Dimensionless stream function
ρ	Density (kg m^{-3})
μ	Dynamic viscosity (kg m^{-1} s^{-1})

Superscripts

*	Dimensional scale

Subscripts

c	Caused by heat convection
eff	Effective
f	Fluid
H	Hot
k	Grid point
L	Cold
max	Maximum
min	Minimum
nf	Nanofluid
p	Nanoparticle
s	Solid

CHARPTER 3

Roman symbols

B	Width of a square prism (m)
C	Cunningham correction factor

c	Streaming speed (m/s)
c_s	Sound speed (m/s)
d_p	Aerosol particle diameter (m)
e_α	Lattice velocity vector
F_B	Brownian force (kg m s^{-2})
F_L	Lift force (kg m s^{-2})
f	Frequency of vortex shedding (Hz)
G_1, G_2	Independent Gaussian random numbers
g	Gravitational acceleration (m s^{-2})
H	Channel height (m)
L	Longitudinal spacing between the centers of two obstacles (m)
M_g	Molecular mass of air (kg kmol^{-1})
N	Number of blocks
O_1	Node on the boundary
O_2	First node inside the boundary
P	Gas pressure (kpa)
p_α	Pressure distribution function
$p_{\tilde{\alpha}}^{out}$	Outgoing distribution functions
p_α^{in}	Incoming distribution functions
R	Universal gas constant (J K^{-1} mol^{-1})
Re	Reynolds number, $u_{max} \cdot B / \upsilon_g$
Stk	Stokes number, $t_p / t_g = d_p^2 \varepsilon \, \mathrm{Re}/(18B^2)$

Str	Strouhal number, $f \cdot B / u_{\mathrm{max}}$
T	Transverse spacing between the centers of two obstacles (m)
T_{g}	Gas temperature (K)
t_g	Characteristic flow time (s)
t_p	Particle response time (s)
Δt	Time step (s)
U_1, U_2	Uniform random numbers between 0 and 1
u, v	Dimensionless gas velocity components along (x, y) axes
$\boldsymbol{u}$	Gas velocity, $[u, v]$
V_p	Volume of a single particle (m^3)
w_α	Weighting coefficient
Δx	Lattice grid spacing
x, y	Dimensionless Cartesian coordinates

Greek symbols

ε	Ratio of particle density to gas density
η	Particle deposition efficiency
λ_g	Mean free path of air molecules (m)
κ	Boltzmann constant (J/K)
μ	Dynamic viscosity (kg m^{-1} s^{-1})
ρ	Density (kg m^{-3})
υ_{f}	Kinematic viscosity (m^2 s^{-1})

τ_f	Dimensionless relaxation time
Ω	Dimensionless vorticity (s^{-1})

Superscripts

*	Dimensional scale

Subscripts

α	Lattice direction
g	gas
p	particle

ABSTRACT

In this dissertation, three topics in thermal systems are investigated: 1) the effect of methyl-ester content on combustion chemistry of a biodiesel surrogate; 2) the effects of non-uniform particle sizes and fluid temperature on heat transfer characteristics of liquid water containing alumina nanoparticles; 3) the effects of obstacle arrangements on transport of aerosol particles in channel flows. The investigation focuses on computational modeling and analysis in the above problems.

In the first study, a kinetic modeling comparison of methyl butanoate and n-butane, its corresponding alkane, contrasts the combustion of methyl esters and normal alkanes, with the aim of understanding the effect of the methyl ester moiety. A fuel-breakdown model [J. Org. Chem. 2008, 73, 94; J. Phys. Chem. A 2008, 112, 51] is added to existing chemical kinetic mechanisms to improve the prediction of CO_2 formation from MB decomposition. Sensitivity and reaction pathway analysis show that the absence of negative temperature coefficient behaviors and reduction of soot precursors can be ascribed to the effect of the methyl ester.

The second study analyzes the heat transfer and fluid flow of natural convection in a cavity filled with Al_2O_3/water nanofluid that operates within differentially heated walls. The Navier-Stokes and energy equations are solved numerically, coupling the model of effective thermal conductivity [J. Phys. D 2006, 39, 4486] and model of effective dynamic viscosity [Appl. Phys. Lett.

2007, 91, 243112]. The numerical simulations explore the range where the heat transfer uncertainties can be affected by the operating conditions of the nanoparticles. Furthermore, the suppressed heat transfer phenomena are in good agreement with the latest experimental data of Ho et al. [Int. J. Therm. Sci. 2010, 49, 1345].

Finally, by using a simple lattice Boltzmann model coupled with a Lagrangian formalism, this study investigates the dispersion and deposition of aerosol particles over staggered obstacles in a two-dimensional channel flow. Particle motion mechanisms considered in the particle phase equation include drag, gravity, lift and Brownian forces. In this study, the results highlight the range of particle dimensions where the particle deposition can be affected by the arrangement of blocks placed in the channel flow.

INTRODUCTION

Computer modeling has become a powerful tool for assisting in design and optimization of thermal systems. In order to define thermal system operating conditions and interpret experimental findings, accurate computational models are now considered as an efficient way of structuring new and detailed knowledge coming from thermal sciences. A classic example can be seen in internal combustion (IC) engines. Nowadays, IC engines are designed to optimize thermal efficiency while meeting emission requirements and minimizing fuel consumption. Therefore, thermal systems in combustion engines, such as fuel, cooling and exhaust systems have to be performed properly especially in the current environmental issues.

In terms of fuel systems, the ubiquitous use of fossil fuels as a primary energy source in IC engines has led to critical societal issues, namely security of supply and climate change; these issues have thus motivated a strong interest in using Computational Chemistry to assist researchers developing alternative fuels to a growing demand for energy.

In order to increase fuel economy, automobile manufacturers have been attempting to lower the weight of vehicles. One of the possible strategies to approach this goal is to reduce the size of coolant systems that remove engine heat. Improving heat transfer performance of engine coolants can provide a means to achieve such a reduction in size. In analysis, Computational Fluid

Dynamics (CFD) can provide insight into the factors controlling the nature of flow and temperature within a cooling system.

To meet the requirements of future stringent emission legislation worldwide, research and development on advanced exhaust emission control technologies will be necessary. One of the methods to reduce emissions is to design better filters for the trapping of particulate matter emissions. Therefore, CFD can be used to provide an assessment of how arrangements of obstacles and protrusions in filters can operate effectively, efficiently and economically.

Motivated by these considerations, in the present study, I have attempted to use three computational techniques to investigate and explore possible solutions for the design of thermal systems. In the study of alternative fuels, kinetic modeling is used to analyze combustion characteristics of biodiesel fuels. In the study of coolant performance, computational fluid dynamics is applied to develop a new mathematical model to describe heat transfer characteristics for one of next generation coolants. In the study of aerosol particle trapping, a lattice Boltzmann method is used to develop a new mathematical model to understand how particles such as soot, are captured in obstructed channel flows. The present results and implications, however, are not limited to the application of IC engines.

CHAPTER 1

KINETIC MODELING OF BIODIESEL COMBUSTION

1.1. Introduction

Fuel security and anthropogenic carbon dioxide emissions, which are associated with climate change, arise from fossil fuel use for energy generation. The relentless growth in demand for energy has exacerbated these issues and has thus driven a search for sustainable alternatives to fossil fuels. One attractive option is biodiesel, which consists of the methyl esters of fatty acids, usually derived from plant oils, although other sources including animal fat are possible. The fatty acyl chains are chemically similar to the aliphatic hydrocarbons, which make up the bulk of the molecules found in petrol and diesel. Fatty acid methyl esters (FAMEs) have a formula of R-(C=O)-O-CH$_3$ where R is a carbon chain of alkyl or alkenyl with as many as 16-18 carbon atoms.

As combustion technologies continue to evolve towards greater efficiency and reduced pollution, their development requires a comprehensive understanding of the combustion behavior of fuels. Kinetic modeling is one way to gain this knowledge through the examination of the oxidation characteristics of fuels and can greatly increase the efficiency of studying a variety of combustion systems. Due to the complexity of biodiesel and the size of its constituent molecules, direct modeling of its combustion has historically

been unfeasible. Instead, a common practice is the use of surrogate molecules or blends that match the characteristics of the real fuel but have much lower computational requirements[1]. Therefore, simpler molecules have instead served as surrogates for the study of biodiesel combustion.

a   b
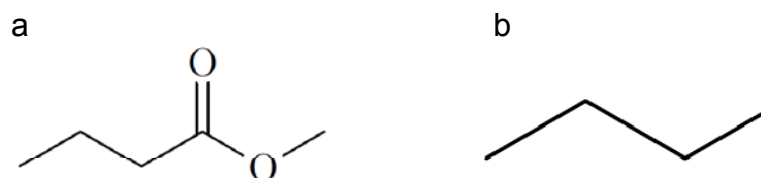
Figure 1.1. Molecule structure of (a) MB; (b) n-butane.

Methyl butanoate (MB), $CH_3CH_2CH_2(C=O)-O-CH_3$ (Figure 1.1a) contains the essential chemical structure of the long-chain fatty acids, i.e., the methyl ester termination and a shorter, but similar, alkyl chain[2-7]. MB was thus chosen initially as a fuel surrogate to produce a manageable chemical kinetic mechanism. Other researchers have recently described kinetic mechanisms for MB, as well as other methyl esters and biofuels, in detail[8,9]. Briefly, Fisher et al. at the Lawrence Livermore National Laboratory (LLNL) created the first MB mechanism, containing 279 species and 1259 reactions[2], which formed a basis for future mechanism development. Metcalfe et al.[4] and Dooley et al.[7] each developed this mechanism further and verified it with a range of experiments, including high temperature shock tube and rapid compression machine studies. Gaïl et al.[3] also modified and validated the LLNL mechanism against opposed diffusion flame and variable pressure flow reactors.

Biodiesel FAMEs contain two oxygen atoms per molecule. This more oxygenated chemical structure of biodiesel fuels alters their combustion and

leads to differences in macro scale performance factors, such as reactivity and pollutant formation, when compared to conventional diesel fuels.

Several important combustion features of methyl esters have been studied, especially in the context of methyl butanoate combustion[8]. One of the most important combustion features that have been studied is autoignition behavior, especially the absence of a negative temperature coefficient (NTC) region in methyl butanoate combustion. The NTC region exhibits a decrease in reactivity over a given intermediate temperature range, typically around 700K to 1000K. Alkylperoxy radical isomerizations are generally associated with this region, as subsequent reaction pathways lead to either chain propagation or branching[10], which determines the reactivity of the system. The decrease in reactivity associated with the NTC region manifests itself, corresponding with the change of the primary reaction pathways from these radicals from chain branching to propagation with increasing temperature.

Fisher et al.[2] predicted a region of NTC behavior for methyl butanoate using their model for homogeneous, isothermal, constant volume combustion. Subsequent studies, however, did not predict similar behavior in other environments. Gaïl et al.[3] did not observe a NTC region in either simulations or experiments for variable pressure flow reactor (VPFR) combustion. Similarly, Dooley et al.[7] did not find NTC for either of flow reactor or rapid compression machine (RCM) experiments or modeling. In contrast, n-butane (Figure 1.1b) does exhibit NTC behavior[11], which implies that the presence of the methyl ester has a significant effect on reactivity. Since the NTC region is ascribed to alkylperoxy radical isomerization, the lack of NTC behavior in MB oxidation suggests that the methyl ester inhibits these reaction pathways; however, as

larger molecules do exhibit an NTC region, this effect diminishes with alkyl chain length. The unique pathways that influence this effect are of substantial interest, insofar as we wish to understand the role of the methyl ester in combustion.

CO$_2$ formation which occurs relatively early in combustion as a consequence of fuel-bound oxygen is a characteristic feature of methyl butanoate oxidation, in contrast with non-oxygenated fuels. Several researchers[6,12] have observed that the primary channels for this CO$_2$ production involve the butanoic acid (BAOJ) and methoxy formyl (CH$_3$OCO) radicals. These pathways are a direct result of the methyl ester moiety in methyl butanoate. Beyond simply noting the existence of this phenomenon, the formations of oxygenated species, such as CO$_2$ and CO have implications on the production of soot precursors such as acetylene. Studies involving both simulation and experiment have noted a decrease in soot formation when utilizing oxygenated fuels[13-15]. For example, an engine modeling study performed by Westbrook et al.[6] found that displacing an oxygenated diesel surrogate, n-heptane, with oxygenated molecules lowered the overall formation of soot precursors. The mechanism for this reduction is thought to be due to the strength of the carbon-oxygen bond that is higher as compared with carbon-carbon or carbon-hydrogen bonds, as noted by Osmont et al.[16]. Ostensibly, the carbon-oxygen bond persists throughout the combustion process, which removes at least one carbon from a pool of carbon atoms that may form soot precursors. In the case of MB, Westbrook et al.[6] suggest that the fuel-bound oxygen atoms remain bonded to one carbon, forming mainly carbon dioxide. Arguably, the formation of CO$_2$ effectively wastes an oxygen

atom that could potentially prevent a different carbon atom from forming a soot precursor; however, the exact mechanism by which the methyl ester moiety reduces soot precursor formation has not yet been fully analyzed. A more detailed analysis of this phenomenon will provide more insight into this mechanism.

In this work, we develop a new kinetic mechanism for MB (MBUMv2) to simulate the formation of carbon dioxide in the pyrolysis of MB in a shock tube[12]. Utilizing MBUMv2, we contrast the oxidation characteristics of MB in a shock tube with its corresponding normal alkane, n-butane. As MB and n-butane differ only by the methyl ester moiety in MB, the results of this study will isolate the effect of this moiety on combustion parameters, namely reactivity, as well as the formation of carbon dioxide, carbon monoxide, acetylene (C_2H_2), an important soot precursor[17], and the related species ethylene (C_2H_4).

1.2. Methodology

The MBUMv2 mechanism is derived from the kinetic mechanism presented by Fisher et al.[2] together with the addition of the newly found reaction pathways for the breakdown of MB[5], six-centered unimolecular elimination reaction that yields ethylene and methyl acetate[4,18] and LLNL detailed n-heptane mechanism[19] which is for the consistency in shared reactions between MB and n-butane.

The kinetic mechanism is first validated in oxidation regimes against experimental data for MB and liquefied propane gas (LPG) blend mixtures in a Jet Stirred Reactor (JSR)[3,20] and ignition delay times of MB and n-butane in a

Table 1.1. Molecule abbreviations for methyl butanoate species used throughout this study.

Molecule	Abbreviation
BAOJ	$CH_3CH_2CH_2C(=O)O$
$C_5H_7O_2$	$CH_2=CHCHCOOCH_3$
MB	$CH_3CH_2CH_2C(=O)OCH_3$
MB2J	$CH_3CH_2CHC(=O)OCH_3$
MB3J	$CH_3CHCH_2C(=O)OCH_3$
MB4J	$CH_2CH_2CH_2C(=O)OCH_3$
MBMJ	$CH_3CH_2CH_2C(=O)OCH_2$
MB2D	$CH_3CH=CHC(=O)OCH_3$
MB3D	$CH_2=CHCH_2C(=O)OCH_3$
ME2J	$CH_2C(=O)OCH_3$
MP3J	$CHCH_2C(=O)OCH_3$
MP2D	$CH=CH_2C(=O)OCH_3$
MP2D3J	$CH=CHC(=O)OCH_3$

shock tube[7,21]. For validating the prediction of autoignition characteristics, we define ignition delay time as the time between the beginning of the simulation and the maximum rate of increase in OH concentration[7], $\frac{d[OH]}{dt}$.

Analysis is performed for oxidation in a shock tube, focusing on ignition delay, as well as the production of CO, CO_2, C_2H_2 and C_2H_4, employing both rate of production (ROP) and sensitivity analyses to investigate fuel chemistry. In sensitivity analyses, the sensitivity coefficient, σ, is defined as $\sigma = \frac{\tau'_{id} - \tau_{id}}{\tau_{id}}$, where τ_{id} is the ignition delay of the unperturbed mechanism and τ'_{id} is that of the adjusted mechanism by increasing the A-factors of the forward and reverse rate constants of a reaction or class of reactions by a factor of 2. A positive sensitivity coefficient signifies an increase in ignition delay, while a negative one indicates a decrease[7,22].

Simulations are performed using the CHEMKIN 4.1 software package[23]. Table 1.1 enumerates some relevant molecule abbreviations used in the mechanism and throughout this study.

1.3. Mechanism Validation

1.3.1. Oxidation of MB and LPG in a Jet Stirred Reactor

Figure 1.2 and Figure 1.3 show the experimental[3,20] and predicted mole fraction profiles of fuels, carbon dioxide, and acetylene in the JSR combustion of MB and LPG. The modeling results are in good agreement with the experimental values except for acetylene from MB, for which a similar discrepancy can be seen in the previous studies[7,24].
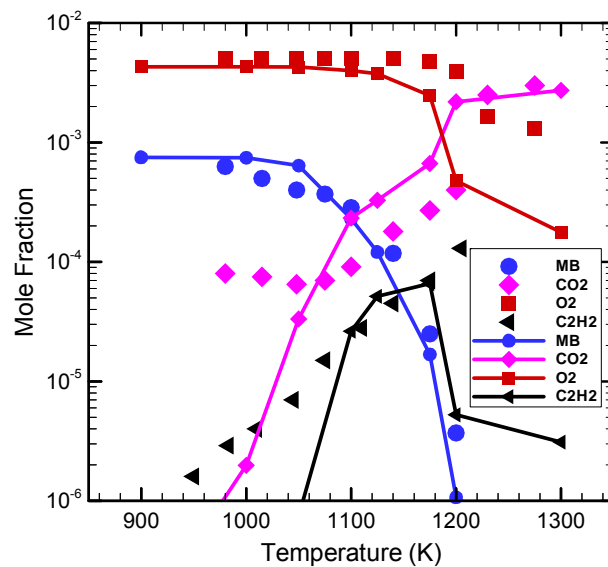
Figure 1.2. Mole fraction profiles of MB, O_2, CO_2, C_2H_2 for MB oxidation as a function of temperature with ϕ of 1.13 (0.075% MB, 0.43% O_2, and 99.945% N_2), a residence time of 0.7 s, and P = 1 atm in a JSR. Symbols are experimental data[3] and lines with symbols are modeling results.
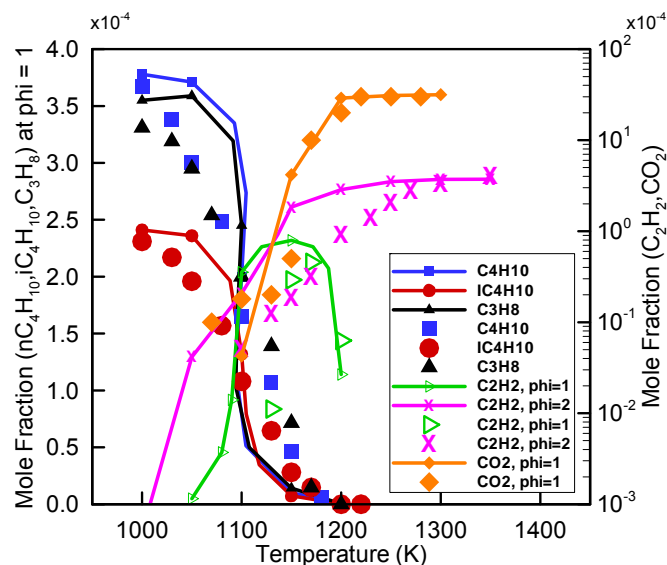
Figure 1.3. Mole fraction profiles of nC_4H_{10}, iC_4H_{10}, C_3H_8, C_2H_2, and CO_2 for LPG (36.2% C_3H_8, 24.8% iC_4H_{10}, and 39% nC_4H_{10}) oxidation as a function of temperature with a residence time of 0.12 s, 0.1% LPG, $\phi = 1$, and P = 1 atm in a JSR. Symbols are experimental data[20] and lines with symbols are modeling results.

1.3.2. Ignition delay times of MB and n-butane in a shock tube

Figure 1.4 and Figure 1.5 present the results of calculated ignition delay
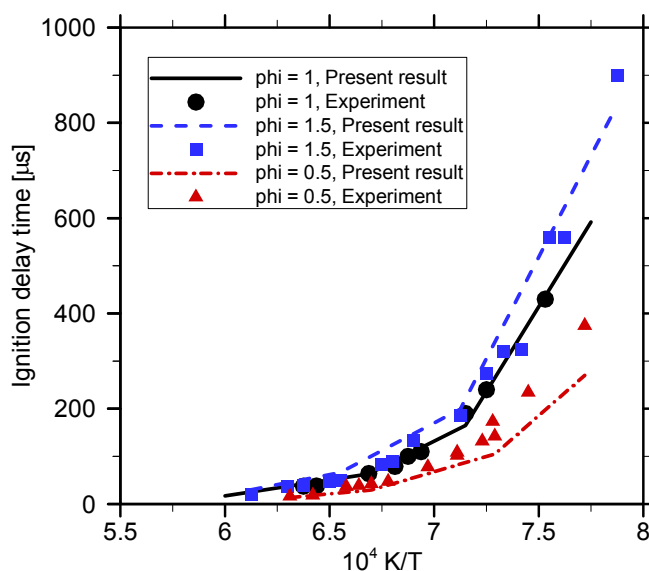
Figure 1.4. Calculated and measured ignition delay times of MB/O_2/Ar mixtures versus temperature for ϕ of 0.5, 1, and 1.5 at pressure of 4 atm. Experimental data are taken from Dooley et al.[7].

10
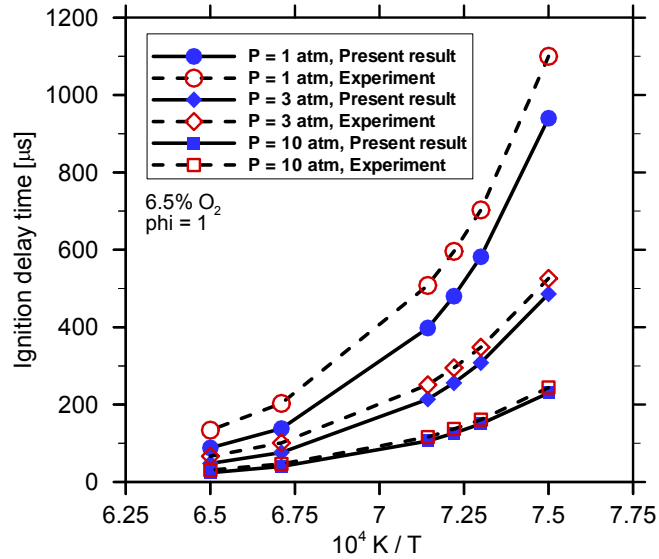
Figure 1.5. Calculated and measured ignition delay times of n-butane/O_2/Ar mixtures versus temperature for different pressures at ϕ of 1 (1% C_3H_8, 6.5% O_2, 92.5% N_2). Experimental data are taken from Horning et al.[21].

times of MB/O_2/Ar and n-butane/O_2/Ar mixtures in a shock tube at different operational parameters, together with the experimental data from the literature[7,21]. The MBUMv2 mechanism successfully reproduced autoignition features as a function of temperature.

1.4. Results and discussion

1.4.1. Prediction of CO$_2$ formation in MB pyrolysis

The MBUMv2 mechanism is used to study the formation of CO_2 in the MB pyrolysis in a shock tube. The experimental data have been recently obtained by the research group of Prof. Hanson at Stanford[12]. The reactor is fed with 2% MB in Ar, and two conditions are analyzed: (i) T = 1260 K and P = 1.702 atm and (ii) T = 1426 K and P = 1.578 atm. The comparison between the experimental data and the computed results for the concentration of CO_2 is reported in Figure 1.6. The newly assembled kinetic model gives a very good
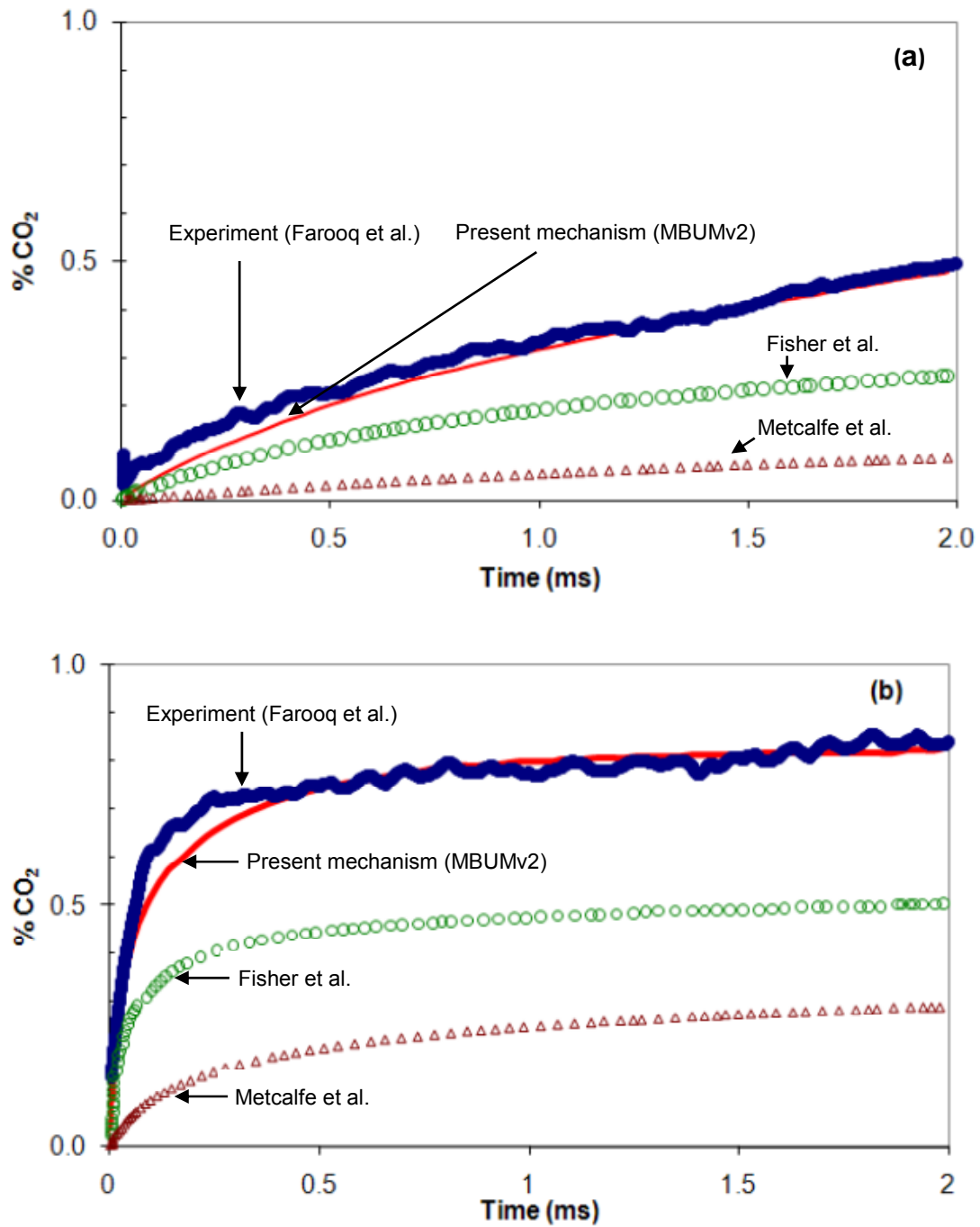
Figure 1.6. Mole fraction profiles of CO_2 for MB pyrolysis (2% MB in Ar) as a function of time at reflected shock conditions: (a) T = 1260 K and P = 1.702 atm and (b) T = 1426 K and P = 1.578 atm. The experimental data are taken from Farooq et al.[12]. The computer simulation results are also compared with the kinetic modeling solutions of Fisher et al.[2] and Metcafe et al.[4].

agreement with the experimental CO_2 profiles for the two cases. The error is

within 10% of the experimental data for the whole residence time.
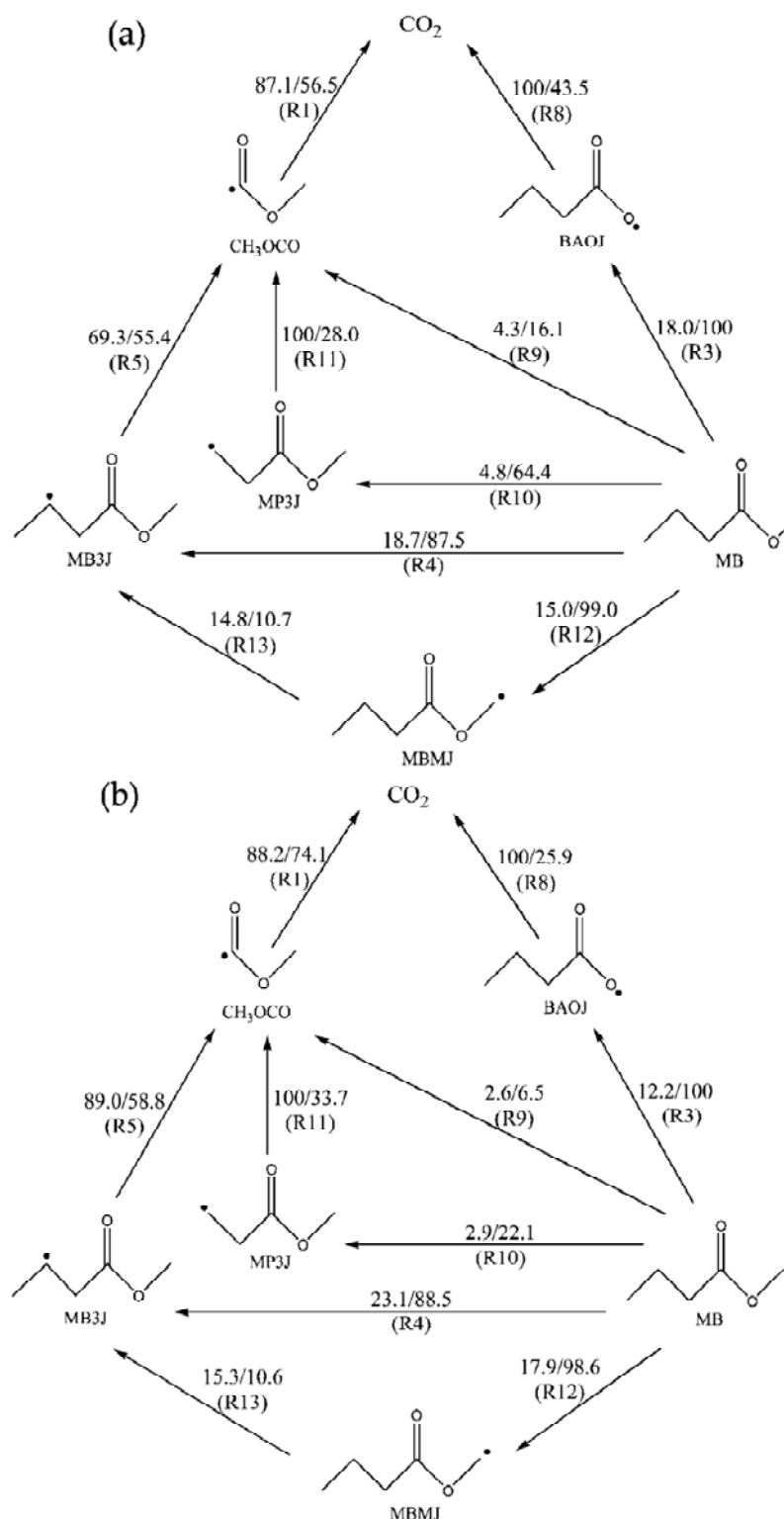
Figure 1.7. Flux analyses for the formation of CO_2 during the MB pyrolysis at T = 1426 K and P = 1.578 atm in the shock tube. The analyses are carried out with the MBUMv1 mechanism at different residence times: (a) t = 0.1 ms and (b) t = 0.4 ms. The most important reactions involved in each pathway are given in parentheses. The notation "A/B" means A% reactant produces B% product in the considered channel.

To understand the formation of CO_2 during the MB breakdown, flux analyses are carried out using the MBUMv2 mechanism. Table 1.2 lists the main reactions involved in the formation of CO_2 for the shock tube simulations. Figure 1.7 shows the flux analyses for CO_2 formation in the shock tube ($T = 1426$ K and $P = 1.578$ atm) at a residence time of 0.1 ms (Figure 1.7a) and 0.4 ms (Figure 1.7b). In both cases, CO_2 is produced by two main pathways involving β-scission reactions. At $t = 0.1$ ms, 87.1% CH_3OCO (through reaction R1) and 100% BAOJ (through reaction R8) are responsible for 56.5% and 43.5% CO_2 formation, respectively. As the simulation proceeds, the CH_3OCO channel becomes more important, accounting for 74.1% of CO_2 formation compared to 25.9% for the BAOJ channel at $t = 0.4$ ms.

Table 1.2. Main reactions for the formation of CO_2 during MB pyrolysis.

Reactions	No.
$CH_3OCO = CH_3 + CO_2$	(R1)
$CH_3OCO = CH_3O + CO$	(R2)
$CH_3CH_2CH_2COO$ (BAOJ) + CH_3 = MB	(R3)
MB + H = $CH_3CHCH_2COOCH_3$ (MB3J) + H_2	(R4)
$CH_3CHCH_2COOCH_3$ (MB3J) = $CH_3OCO + C_3H_6$	(R5)
MB + H = $CH_2CH_2CH_2COOCH_3$ (MB4J) + H_2	(R6)
$CH_2CO_2CH_3 + C_2H_5$ = MB	(R7)
$CH_3CH_2CH_2COO$ (BAOJ) = $n\text{-}C_3H_7 + CO_2$	(R8)
MB = $n\text{-}C_3H_7 + CH_3OCO$	(R9)
MB = $CH_3 + CH_2CH_2COOCH_3$ (MP3J)	(R10)
$CH_2CH_2COOCH_3$ (MP3J) = $C_2H_4 + CH_3OCO$	(R11)
MB + H = $CH_3CH_2CH_2COOCH_2$ (MBMJ) + H_2	(R12)
$CH_3CH_2CH_2COOCH_2$ (MBMJ) = $CH_3CHCH_2COOCH_3$ (MB3J)	(R13)

CH_3OCO can be formed from MB directly through the unimolecular decomposition reaction (reaction R9) or indirectly through the hydrogen abstraction reactions to create MB3J and MP3J (reactions R4 and R10, respectively) and the combination between hydrogen abstraction and

hydrogen migration from MBMJ (reaction R12 and R13). For convenience in discussion, the net flux ratio between the two channels from CH_3OCO to CO_2 and CO can be denoted as ($CH_3OCO \rightarrow CO_2$) and ($CH_3OCO \rightarrow CO$), respectively. The net flux is the sum of the forward and reverse flux for each channel. As the time elapses, the CO_2 dissociation channel becomes more and more important; particularly, the ($CH_3OCO \rightarrow CO_2$)/($CH_3OCO \rightarrow CO$) ratio is 6.7 and 7.4 at $t = 0.1$ and $t = 0.4$ ms, respectively.

1.4.2. Oxidation of MB and n-butane in a shock tube

1.4.2.1. Ignition characteristics

We study shock tube oxidation of stoichiometric mixtures of each fuel and air for a range of temperatures from 750K to 1300K and pressures of 12.5 atm and 40 atm (values after reflected shock). These pressures are chosen in accordance with a study by Hoffman et al.[25] comparing several fuel surrogates in homogeneous charge compression ignition (HCCI) engine conditions. Additionally, we investigate the effect of changing the absolute amount of fuel and oxygen in the system while maintaining stoichiometric conditions.

The simulations are performed for oxygen concentrations (mole fraction) of 6.5% and 19.5%, or 1% and 3% fuel respectively. Figure 1.8 shows the computed ignition delay times for both fuels under these conditions. The effect of the absolute amount of fuel and oxygen is insignificant, so further discussion will be limited to the 19.5% O_2 case. The primary difference in combustion, as expected, is the strong NTC behavior of n-butane that is not matched by methyl butanoate, which occurs between 740K and 890K at 12.5 atm or 750K and 920K at 40 atm. At temperatures above these regions, the two fuels show

similar autoignition characteristics. We subsequently conduct sensitivity analysis to identify important reactions governing autoignition.
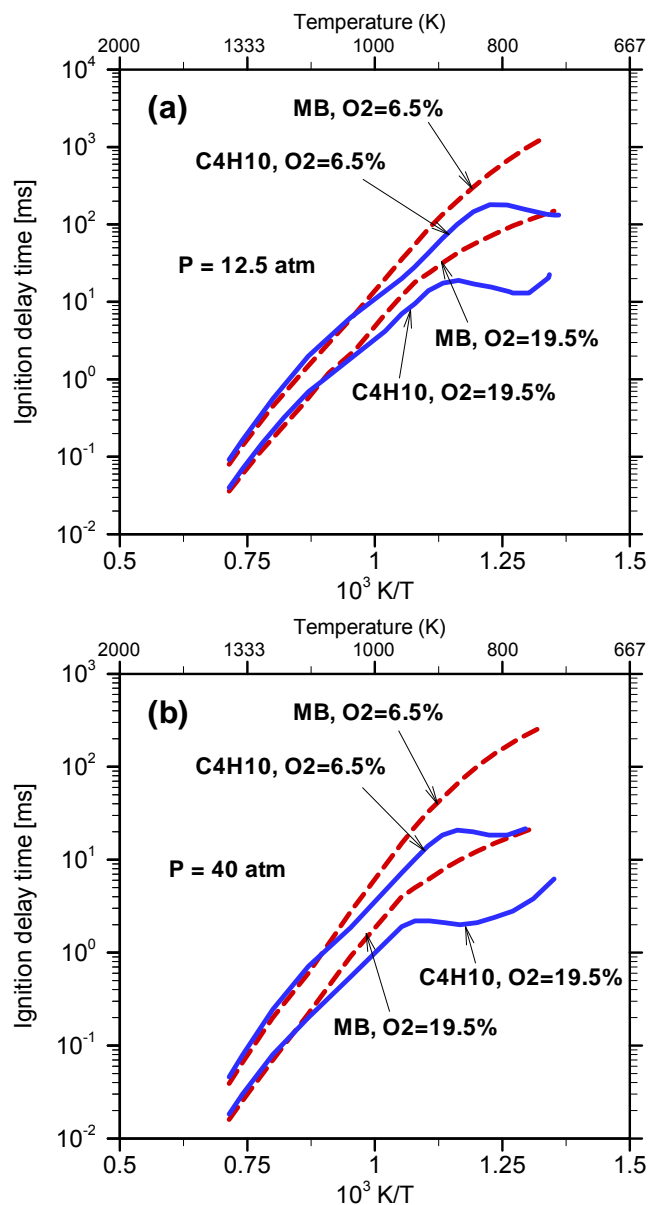
Figure 1.8. Calculated ignition delay times for stoichiometric mixtures of MB/O_2/Ar and C_4H_{10}/O_2/Ar versus temperature at pressure of (a) 12.5 atm and (b) 40 atm. 1% Fuel, 6.5% O_2, 92.5% N_2; 3% Fuel, 19.5% O_2, 77.5% N_2.

Since the results are similar between both studied pressures, we will only discuss the results at 12.5 atm. The results of this analysis are shown in Figures 1.9 and Figure 1.10, for the temperatures 1400K and 780K

respectively and for a pressure of 12.5 atm. At 1400K, analogous sensitivity results reflect the similarity in ignition delay between both fuels; each fuel's ignition properties are sensitive to similar types of reactions.
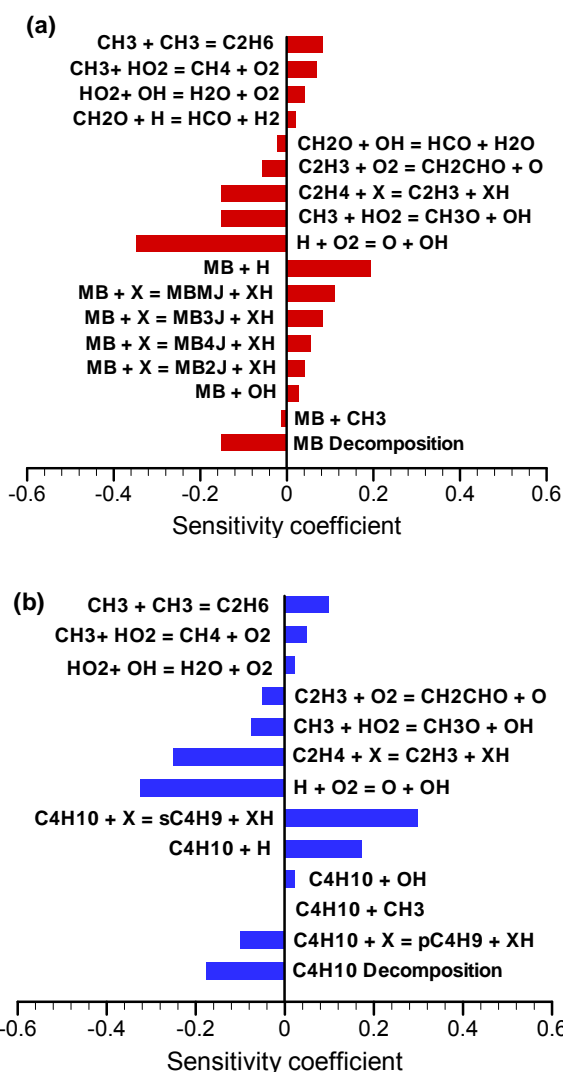
Figure 1.9. Ignition delay sensitivity results at T = 1400K, P = 12.5 atm, for mixtures of 3% Fuel, 19.5% O_2 and 77.5% N_2. (a) methyl butanoate; (b) n-butane. The symbol 'X' denotes the combined sensitivity to reactions by the radicals H, OH and CH_3.

Figure 1.10 shows the differences in sensitivity results between both fuels at 780K. A major feature of the results is the dependence of autoignition on reactions that involve HO_2 or OH. The hydroperoxyl radical HO_2 negatively
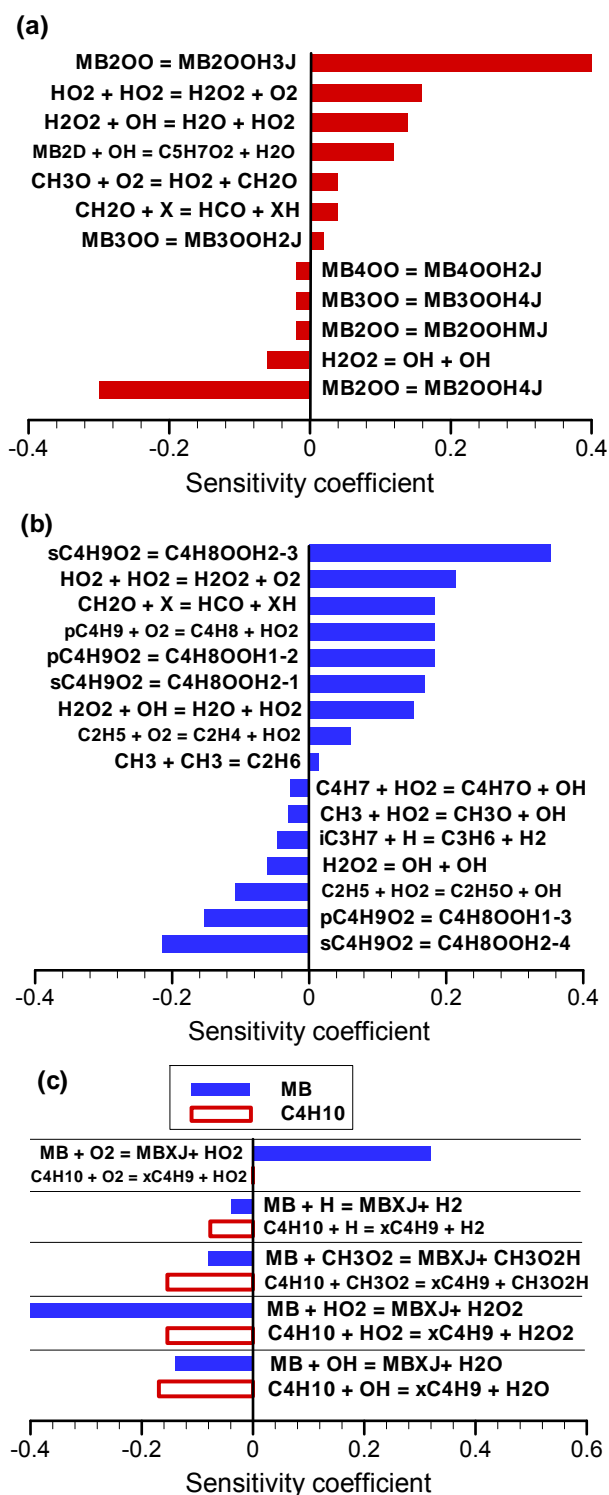
Figure 1.10. Ignition delay sensitivity results at T = 780K, P = 12.5 atm, for mixtures of 3% Fuel, 19.5% O_2 and 77.5% N_2. (a) methyl butanoate; (b) n-butane; (c) sensitivity of ignition delay to hydrogen abstraction reactions. The symbols 'X' and 'x' denote the combined sensitivity to reactions at possible abstraction sites for MB and n-butane, respectively.

affects the concentration of hydroxyl radical OH, which governs the reactivity of the system. Specifically, the recombination reaction $HO_2 + HO_2 = H_2O_2 + O_2$ is a chain termination reaction; moreover, H_2O_2 further consumes OH through the reaction $H_2O_2 + OH = HO_2 + HO_2$, which forms a radical consuming cycle. Consequently, reactions that produce HO_2 significantly reduce reactivity.

Extending this concept further, any reactions involved in pathways that form either HO_2 or OH will influence the autoignition properties of their respective fuels. For example, at 1400K (Figure 1.9), hydrogen abstractions from MB increase ignition delays, as these reactions consume radicals such as H, OH, or CH_3. In particular, hydrogen abstraction from MB by H-atoms decreases reactivity through competition with the branching reaction $H + O_2 = O + OH$. Conversely, as the importance of this branching reaction decreases with temperature, hydrogen abstractions increase reactivity at lower temperatures, shown for 780K in Figure 1.10. This result illustrates the indirect effect that reactions can have on reactivity, without involving OH or HO_2 directly.

Table 1.3. The most important reactions involved in direct methyl butanoate and n-butane consumption in our autoignition study.

MB	C_4H_{10}
R25. $MB + HO_2 = MB3J + H_2O_2$	R738. $C_4H_{10} + H = pC_4H_9 + H_2$
R35. $MB + CH_3O_2 = MB2J + CH_3O_2H$	R739. $C_4H_{10} + H = sC_4H_9 + H_2$
R36. $MB + HO_2 = MB2J + H_2O_2$	R740. $C_4H_{10} + OH = pC_4H_9 + H_2O$
R371. $MB + H = MB4J + H_2$	R741. $C_4H_{10} + OH = sC_4H_9 + H_2O$
R373. $MB + OH = MB4J + H_2O$	R745. $C_4H_{10} + HO_2 = sC_4H_9 + H_2O_2$
R379. $MB + H = MB3J + H_2$	
R381. $MB + OH = MB3J + H_2O$	
R385. $MB + H = MB2J + H_2$	
R387. $MB + OH = MB2J + H_2O$	
R403. $MB + H = MBMJ + H_2$	
R405. $MB + OH = MBMJ + H_2O$	

Table 1.4. Proportions of consumed fuel by specific reactions in our auto-ignition study. Normalized rates of production are computed at 2%, 33% and 50% fuel consumption (0.006s, 0.084s and 0.096s). $T = 780K$; $P = 12.5$ atm; $\phi = 1$.

Time (s)	Reaction consuming MB (%)					
	R25	R35	R36	R371	R373	R379
0.006	-	-14.8	-15.8	-	-14.8	-
0.084	-6.4	-8.5	-30.5	-7.1	-5.9	-7.5
0.096	-	-	-18.8	-13.3	-5.3	-13.0
Time (s)	Reaction consuming MB (%)					
	R381	R385	R387	R403	R405	
0.006	-18.2	-	-15.3	-	-10.2	
0.084	-6.1	-6.4	-6.1	-	-	
0.096	-10.9	-	-5.4	-7.0	-	
Time (s)	Reaction consuming n-C$_4$H$_{10}$ (%)					
	R738	R739	R740	R741	R745	
0.003	-	-	-32.7	-58.4	-	
0.0106	-	-11.2	-24.0	-40.9	-62.0	
0.0126	-5.5	-17.1	-23.8	-39.8	-	

Consequently, the reaction pathways involved in the decomposition of MB and n-butane to either HO$_2$ or OH will help to elucidate the effect of the methyl ester on the NTC region. Therefore, for shock tube oxidation of both fuels at 780K, we perform rate of production (ROP) or flux analysis at times throughout the simulation, namely 2%, 33% and 50% fuel consumption, or 0.006s, 0.084s and 0.096s respectively. The most important reactions in the consumption of each fuel are shown in Table 1.3.

Table 1.4 lists the proportions of the fuel that form each alkylester or alkyl radical for combustion of methyl butanoate and n-butane. The evolution of these radicals ultimately influences the autoignition behavior of their corresponding fuels; in the low temperature region, these radicals react with O$_2$ to form RO$_2$ radicals, which isomerize and subsequently lead to the formation of either HO$_2$ or OH and thus significantly affect ignition delay.

Figure 1.11 and Figure 1.12 illustrate the primary decomposition pathways
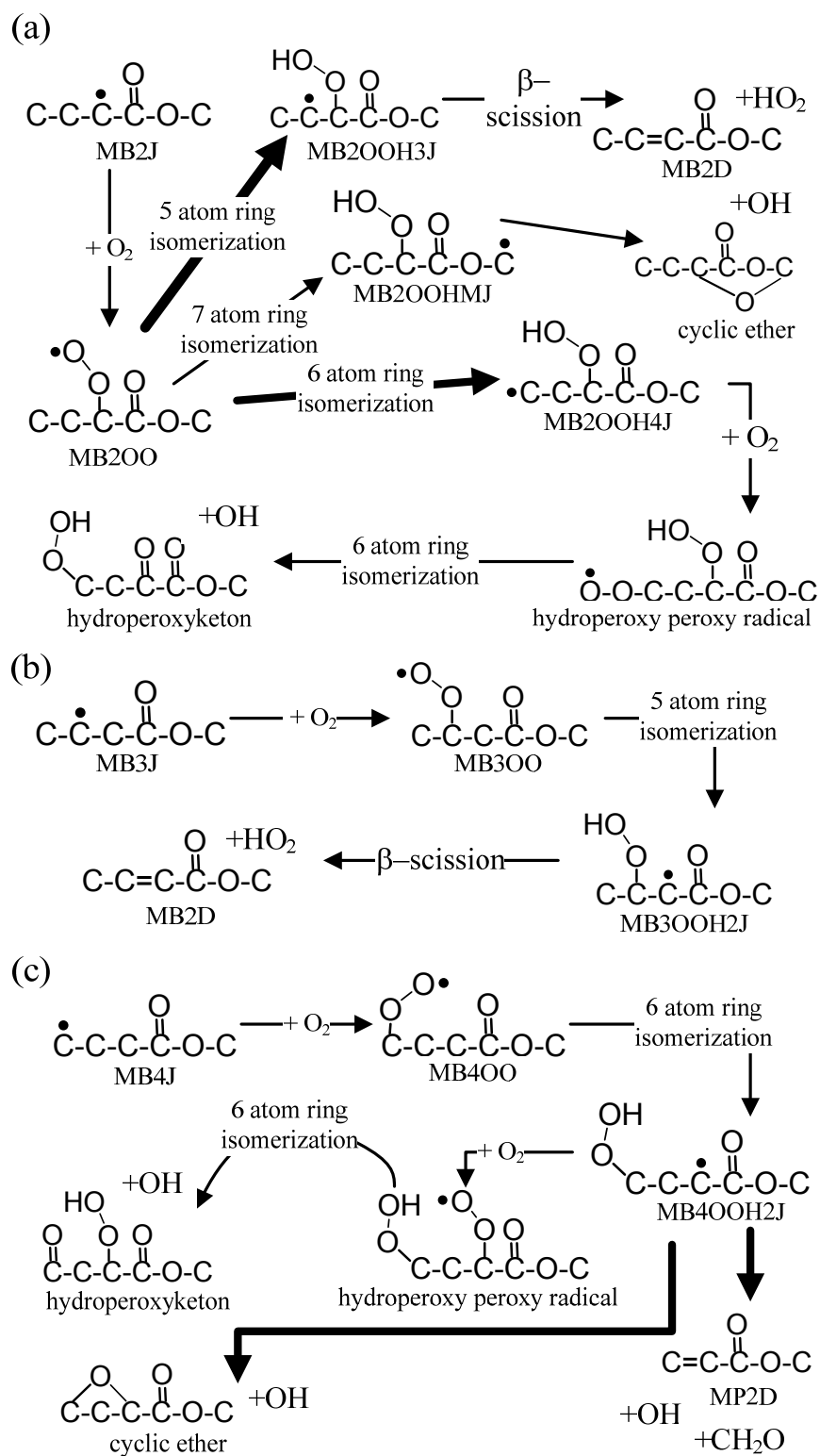
Figure 1.11. Decomposition pathways at 33% fuel consumption for primary fuel alkylester radicals (methyl butanoate) at T = 780K, P = 12.5 atm, ϕ = 1. (a) MB2J; (b) MB3J; (c) MB4J.
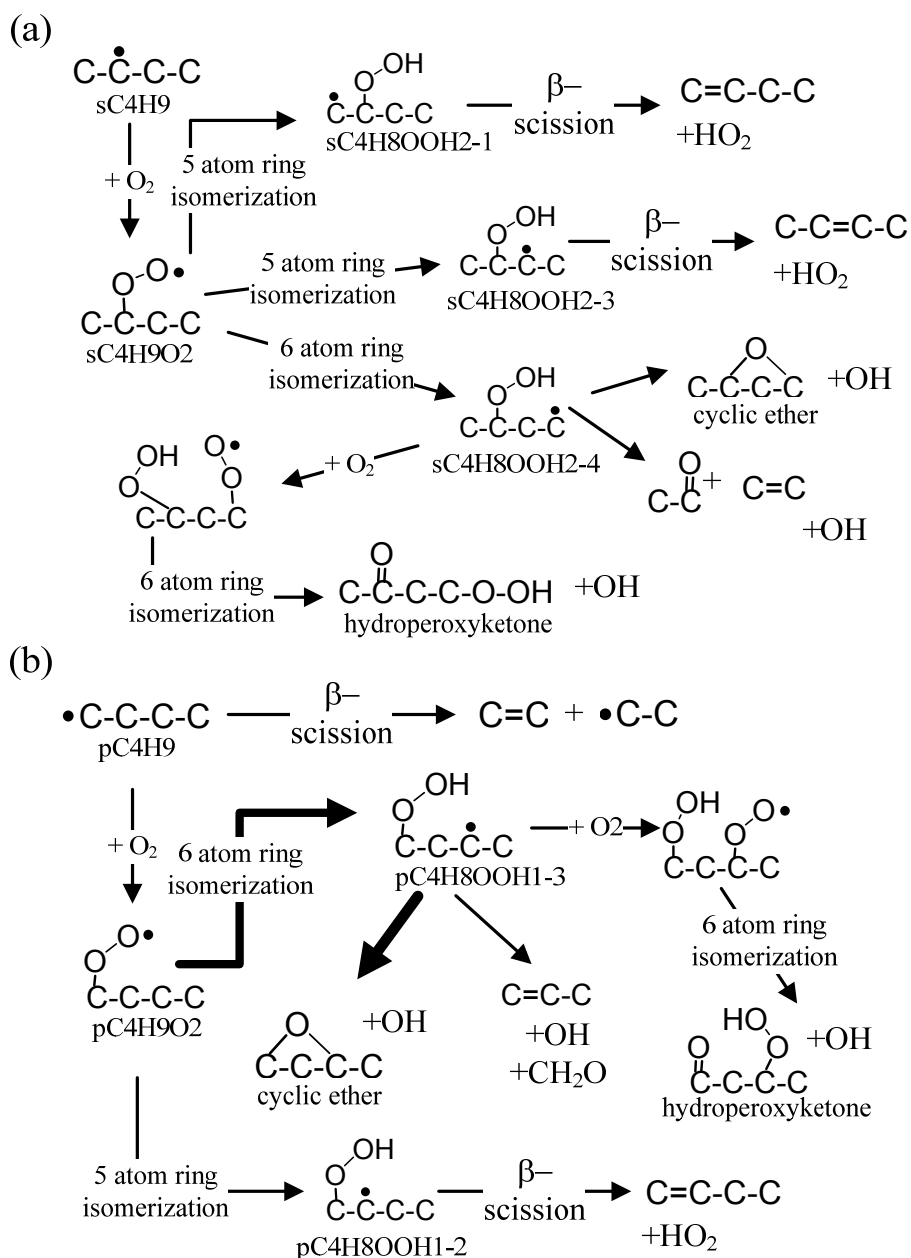
Figure 1.12. Decomposition pathways at 33% fuel consumption for primary fuel alkyl radicals (n-butane) at T = 780K, P = 12.5 atm, ϕ = 1. (a) sC_4H_9; (b) pC_4H_9.

for the fuel alkylester or alkyl radicals of both fuels, derived from flux analysis at 33% fuel consumption. The radical MB2J (Figure 1.11a) reacts to form MB2OO, which subsequently isomerizes through 5-, 6- and 7- membered transition states to form the hydroperoxy alkylester radicals MB2OOH3J, MB2OOH4J and MB2OOHMJ respectively. The most important channels in

this case are the 5-membered and 6-membered reactions, which lead to the formation of HO_2 and OH respectively. This result corroborates our sensitivity analysis, where the reaction MB2OO = MB2OOH3J, with a 5-membered transition state, increases ignition delay, while the reaction MB2OO = MB2OOH4J, with a 6-membered transition state, decreases ignition delay. The radical MB3J forms MB3OO, and then primarily through a 5-membered ring, leading to the formation of HO_2. MB4J mainly follows a 6-membered ring pathway, leading to the formation of OH.

Table 1.5. Percentages of each fuel forming specific alkylester (methyl butanoate) or alkyl (n-butane) radicals. $T = 780K$; $P = 12.5$ atm; $\phi = 1$.

Time (s)	Alkylester radical (% MB)			
	MB2J	MB3J	MB4J	MBMJ
0.006	46	18	15	10
0.084	52	20	13	-
0.096	24	24	19	7
Avg.	40	20	16	6
Time (s)	Alkyl radical (% C_4H_{10})			
	pC_4H_9	sC_4H_9		
0.003	33	58		
0.0106	24	58		
0.0126	29	57		
Avg.	29	58		

Similarly, the fuel alkyl radicals of n-butane, sC_4H_9 and pC_4H_9, can react through 5- or 6- membered ring pathways. The radical sC_4H_9 behaves similarly to the radical MB2J, where the 5- and 6- membered pathways lead to HO_2 and OH respectively. The sensitivity analysis in Figure 1.10 reflects the effect of these pathways, where the 5-membered reaction $sC_4H_9O_2 = C_4H_8OOH_{2-3}$ inhibits reactivity, whereas the 6-membered reaction $sC_4H_9O_2 = C_4H_8OOH_{2-4}$ enhances reactivity. The radical pC_4H_9 mainly reacts through pathways leading

to the formation of OH, namely through the reaction $pC_4H_9O_2 = C_4H_8OOH_{1-3}$, a 6-membered isomerization.

These results demonstrate how the methyl ester moiety changes the low temperature oxidation of methyl butanoate in contrast to its corresponding normal alkane, n-butane. Table 1.5 shows that, over the time period that we studied, an average of 58% of n-butane and 40% of MB react through sC_4H_9 and MB2J respectively, radicals which behave similarly. Due to the methyl ester, however, MB3J behaves differently than MB2J; namely, in the case of n-butane, the positions of these carbons are symmetrically equivalent and the corresponding radicals are not treated differently. In the same way, the radical pC_4H_9 is formed from two symmetrically equivalent carbons on either end of n-butane; in methyl butanoate, one of these carbons is bonded as part of the methyl ester moiety. This asymmetry also explains the result that considerably more of n-butane, an average of 29%, reacts through the reactivity enhancing pathway involving pC_4H_9, compared with an average of 16% of MB following the analogous pathway through MB4J. The methyl ester therefore reduces the amount of fuel that follows channels that enhance reactivity and also enables the reactivity inhibiting pathway through MB3J. This effect offers an explanation for the absence of NTC behavior in MB combustion. Ostensibly, the alkyl chain of MB is too short to overcome this effect, which is consistent with previous observations by Walton et al.[26]. As well, the asymmetry of the methyl ester moiety can be expected to decrease in significance as the alkyl chain increases in length. This theory is therefore consistent with observed NTC behavior in the combustion of larger methyl esters[27].

1.4.2.2. Formation of oxygenated species

To investigate the production of oxygenated species from fuel-bound oxygen, we investigate shock tube oxidation of stoichiometric mixtures of both fuels at temperatures of 1100K and 1600K and a pressure of 4 atm. These conditions are chosen to match the range of conditions studied by Dooley et al.[7]. Using the shock tube model allows us to capture the time dependence of CO_2 or CO formation from methyl butanoate oxidation and contrast it with that of n-butane. Clearly, n-butane contains no fuel-bound oxygen; therefore understanding the formation of oxygenated species from n-butane will facilitate the identification of reaction channels unique to the methyl ester. Our chosen stoichiometric conditions allow oxidation of either fuel that is unconstrained by
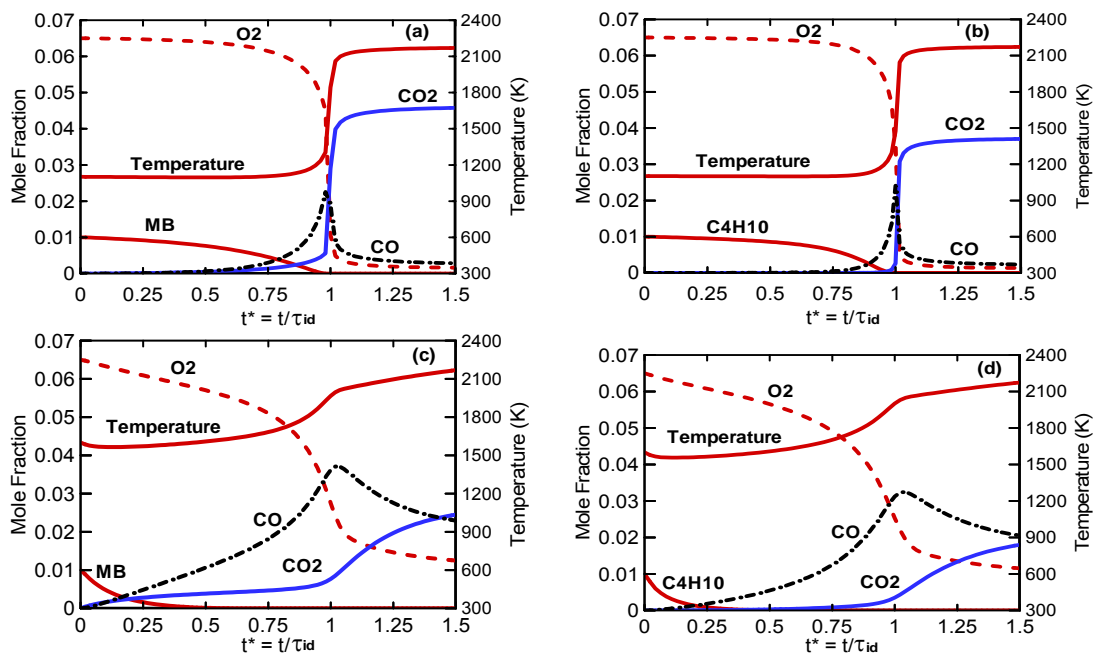
Figure 1.13. Temperature and concentration profiles of selected species for shock tube oxidation at P = 4 atm, ϕ = 1 (1% Fuel, 6.5% O_2, 92.5% N_2): $t^* = t /\tau_{id}$; (a) MB at T = 1100K, τ_{id} = 0.0075s; (b) n-butane at T = 1100K, τ_{id} = 0.00945s; (c) MB at T = 1600K, τ_{id} = 2.8×10^{-5} s (d) n-butane at T = 1600K, τ_{id} = 2.3×10^{-5} s.

the amount of environmental oxygen. Figure 1.13 compares n-butane and methyl butanoate combustion, at both 1100K and 1600K; the plots show temperature profiles, as well as the concentration profiles of MB, C_4H_{10}, O_2, CO and CO_2 plotted as a function of normalized residence time $t^* = t / \tau_{id}$. Methyl butanoate combustion produces a substantial amount of CO_2 prior to ignition ($t^* = 1$), in comparison to that of n-butane, which is typically ascribed to the effect of the methyl ester, or specifically fuel-bound oxygen.

We seek to capture the effect of this fuel-bound oxygen and conduct ROP analysis to elucidate the pathways involved in both CO and CO_2 production from both fuels. The flux analysis focuses on reaction pathways at $t^* = 0.8$ and $t^* = 0.2$ for the temperatures 1100K and 1600K respectively. These times are chosen to be approximately at the intersection of the concentration curves of MB decomposition and CO_2 production. In this way, we ensure that there will be sufficient amounts of species such that we can find pathways connecting the fuel and oxygenated species.

Under these conditions, the first step in the formation of oxygenated species is the formation of fuel alkylester or alkyl radicals from each fuel. The

Table 1.6. The most important reactions involved in methyl butanoate and n-butane consumption in our oxygenated species study.

Reactions of MB	Reactions of C_4H_{10}
R5. MB (+M) = MP3J + CH_3 (+M)	R724. C_4H_{10} = C_2H_5 + C_2H_5
R6. BAOJ + CH_3 = MB	R738. C_4H_{10} + H = pC_4H_9 + H_2
R7. MB (+M) = ME2J + C_2H_5 (+M)	R739. C_4H_{10} + H = sC_4H_9 + H_2
R371. MB + H = MB4J + H_2	R740. C_4H_{10} + OH = pC_4H_9 + H_2O
R379. MB + H = MB3J + H_2	R741. C_4H_{10} + OH = sC_4H_9 + H_2O
R385. MB + H = MB2J + H_2	
R403. MB + H = MBMJ + H_2	

Table 1.7. Proportions of consumed fuel by specific reactions in our oxygenated species study. Normalized rates of production are computed at P = 4 atm and ϕ = 1.

T (K)	t^*	Reaction Consuming Methyl Butanoate (%)						
		R5	R6	R7	R371	R379	R385	R403
1100	0.8	-	-	-	-25	-21	-18	-14
1600	0.2	-1	-22	-5	-20	-13	-10	-12
T (K)	t^*	Reaction Consuming n-Butane (%)						
		R724	R738	R739	R740	R741		
1100	0.8	-	-13	-37	-15	-25		
1600	0.2	-20	-20	-37	-6	-9		

main reactions involved in this process are listed in Table 1.6; as well, the proportions of each fuel forming each radical are listed in Table 1.7 for both 1100K and 1600K. As mentioned in our analysis of reactivity, methyl butanoates asymmetric structure leads to four distinct alkylester radicals, compared with two in the case of n-butane. The effect of increasing temperature from 1100K to 1600K is to enhance the importance of unimolecular reactions for both fuels. Thus, at 1600K, increased proportions of the fuel follow reactions R5, R6 and R7 from MB, and reaction R724 from n-butane.

1.4.2.2.1. Carbon monoxide

The next step in the formation of oxygenated species involves the decomposition of these fuel radicals. The reaction pathways that connect alkyl ester radicals to carbon monoxide at 1100K are shown in Figure 1.14. The alkylester radicals MB4J, MB3J, and MB2J contribute the most to CO formation. In particular, the pathway beginning with MB4J illustrates a mechanism for direct CO production from MB. MB4J undergo a β-scission reaction to form the methyl ethanoate radical (ME2J). ME2J further decom-

Figure 1.14. Reaction pathways from fuel alkylester radicals (methyl butanoate) to carbon monoxide. T = 1100K; t^* = 0.8s; P = 4 atm; ϕ = 1.

poses to CH_2CO and CH_3O. Similarly, MB3J forms $C_5H_7O_2$, which subsequently produces CH_3O. Table 1.8 lists the reactions and their relative proportions that directly contribute to CO formation at 1100K and 1600K. The majority of CO is formed from reactions involving either HCO or CH_3CO. Figure 1.14 shows that CH_3O primarily forms CH_2O and then HCO; additionally, CH_2CO forms CH_3CO through hydrogen addition. Consequently, a significant amount of CO formation in these conditions is directly traceable fuel-bound oxygen.

Table 1.8. Proportions of carbon monoxide formed by specific reactions. Normalized rates of production are computed at $P = 4$ atm and $\phi = 1$

| Fuel | t^* | Reactions at T = 1100 K (%) | | | | |
		R377	R466	R497	R1840	R2024
MB	0.8	11	11	52	9	5
C_4H_{10}	0.8	6	11	55	24	-

| Fuel | t^* | Reactions at T = 1600 K (%) | | | | | |
		R377	R466	R491	R497	R2024	R2326
MB	0.2	18	26	6	20	9	6
C_4H_{10}	0.2	23	24	6	19	-	12

Reaction number definitions	
R377	$CH_3CO = CH_3 + CO$
R466	$HCO + M = H + CO + M$
R491	$HCO + CH_3 = CH_4 + CO$
R497	$HCO + O_2 = CO + HO_2$
R1840	$CH_2CHO + O_2 => CH_2O + CO + OH$
R2024	$nC_3H_7CO = nC_3H_7 + CO$
R2326	$CH_2(s) + O_2 => CO + OH + H$

In contrast, at 1100K, n-butane produces CO through the radical sC_4H_9, which decomposes to C_3H_6 and CH_3. The methyl radical, CH_3, reacts with HO_2 to form CH_3O and OH. CH_3O then forms CH_2O which leads to HCO and finally CO. The oxygen involved in this process obviously originates from the environment, which is demonstrated by this pathways dependence on the reaction of CH_3 with HO_2. Similar trends apply at 1600K, where a significant portion of CO formed from MB is via the radical ME2J, which links fuel-bound oxygen to CO formation. CO formation from n-butane again is clearly dependent on environmental oxygen.

1.4.2.2.2. Carbon dioxide

Table 1.9 enumerates important reactions in carbon dioxide formation both before and after ignition. Unique pathways involved in CO_2 formation from fuel-bound oxygen in methyl butanoate are easily identified, as n-butane produces negligible amounts of CO_2 at the time of our flux analysis, namely t^*

Table 1.9. Proportions of carbon dioxide formed by specific reactions. Normalize rates of production are computed at $P = 4$ atm; $\phi = 1$.

Fuel	t^*	Reactions at T = 1100 K (%)					
		R383	R1893	R465	R1893	R2316	R2318
MB	0.8	63	28	-	-	-	-
	1	-	-	98	-	-	-
C_4H_{10}	1	-	-	67	15	6	6

Fuel	t^*	Reactions at T = 1600 K (%)		
		R54	R383	R1893
MB	0.2	40	38	20

Reaction number definitions	
R54	$BAOJ = CO_2 + nC_3H_7$
R383	$CH_3OCO = CO_2 + CH_3$
R465	$CO + OH = CO_2 + H$
R518	$CH_2 + O_2 = CO_2 + 2H$
R1893	$HCCO + O_2 = CO_2 + HCO$
R2316	$HOCHO + OH = H_2O + CO_2 + H$
R2318	$HOCHO + H = H2 + CO_2 + H$

Table 1.10. Reactions forming specific proportions of HCCO. $T = 1100K$; $t^* = 0.8$; $P = 4$ atm; $\phi = 1$.

Reaction		HCCO formed (%)
R100	$CH_2CHCHCO + H = HCCO$	17
R101	$CH_2CHCHCO + OH = HCCO + CH_3CHO$	29
R534	$CH_2CO + OH = HCCO + H_2O$	20
R535	$CH_2CO + H = HCCO + H_2$	28

= 0.8 at 1100K and $t^* = 0.2$ at 1600K. At ignition, both fuels produce CO_2 via common pathways, namely through CO, that are less readily linked to fuel-bound oxygen. Prior to ignition, however, MB produces a substantial amount of CO_2 that is traced to the oxygenated methyl ester moiety. At 1100K, fuel-bound oxygen in MB produces CO_2 primarily through the thermal decomposition of the methoxy formyl radical, CH_3OCO, to CO_2 and CH_3, and to a lesser extent the reaction of HCCO with oxygen. The decomposition of MB through fuel alkyl radicals produces CH_3OCO, which connects this CO_2 production with the oxygen in the methyl ester moiety.
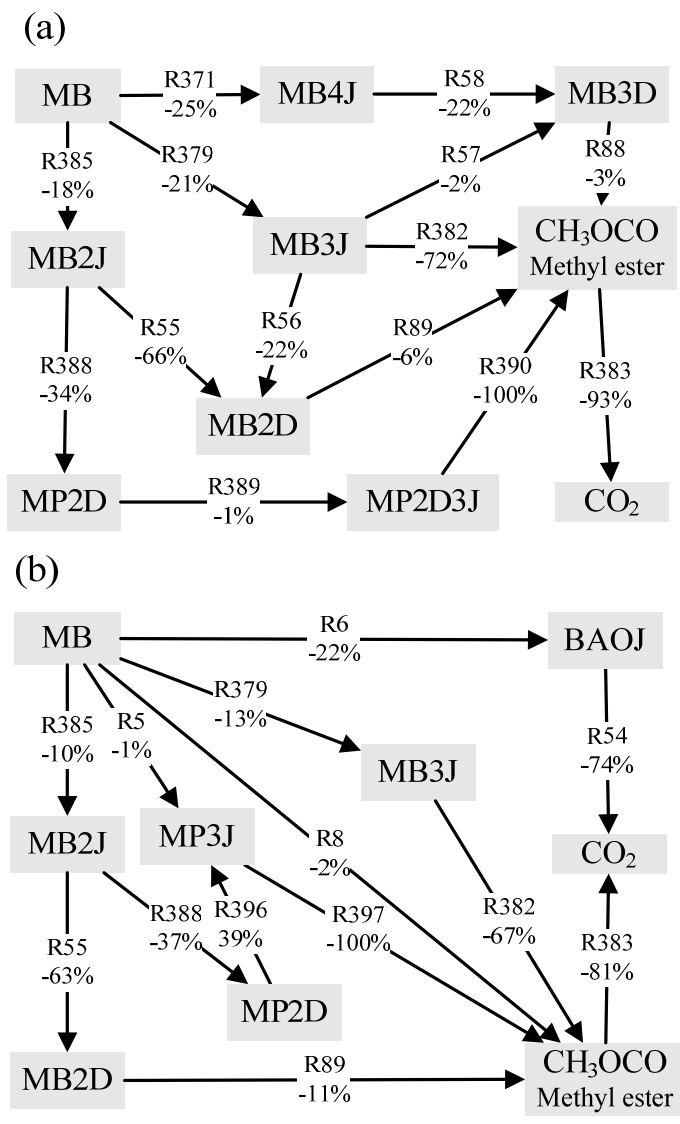
Figure 1.15. Reaction pathways from methyl butanoate to carbon dioxide. $P =$ 4 atm; $\phi = 1$. (a) $T = 1100K$ and $t^* = 0.8s$; (b) $T = 1600K$ and $t^* = 0.2s$.

Also at 1100K, the pathway through HCCO represents another link to fuel-bound oxygen. ME2J, which we have discussed in the context of CO formation, decomposes to CH_3O and CH_2CO, which form CO. CH_2CO also forms HCCO via hydrogen abstraction by OH (R534) and H (R535). Similarly, $C_5H_7O_2$ decomposes to CH_3O, which forms CO, as well as $CH_2CHCHCO$. $H_2CHCHCO$ reacts with H (R100) and OH (R101) to form HCCO. Table 1.10 summarizes the proportions of HCCO that each of these reactions formed. At

1600K, the higher temperature enables the reaction pathway through the butanoic acid radical (BAOJ). 22% of MB forms BAOJ at this temperature, which subsequently forms 40% of CO_2 at this temperature through thermal decomposition. This channel also connects CO_2 production to the methyl ester.

Previous studies[6,17] have suggested that methyl butanoate 'wastes' oxygen by directly forming carbon dioxide from both fuel-bound oxygen atoms, instead of splitting this oxygen between different carbon atoms. We evaluate this notion by examining CO_2 formation directly from both fuel bound oxygen atoms. Figure 1.15 illustrates the reaction pathways that directly link both oxygen atoms in MB to CO_2 formation at both 1100K and 1600K. These pathways involve the radicals CH_3OCO and BAOJ, which is consistent with one of our previous studies[28].

For each reaction in a given pathway, Figure 1.15 denotes the percentage of each reactant forming each product. The mathematical product of these percentages gives the proportion of MB that forms CO_2 through that channel. Summing these proportions gives the amount of methyl butanoate that forms carbon dioxide using both fuel oxygen atoms. The results of this study show that 15% and 28% of MB formed CO_2 in this manner at 1100K and 1600K, respectively. Further discussion of these results involves examining their consequences in the context of the formation of soot precursors.

1.4.2.3. Implications on acetylene and ethylene formation

We choose to study the formation of acetylene (C_2H_2), an important species that is a component of the hydrogen abstraction acetylene addition

(HACA) soot formation mechanism. Based on prior studies and our analysis of oxygenated species, the formation of CO and CO_2 in the breakdown of methyl butanoate should inhibit the formation of soot precursors, so we seek to understand the relationships between the pathways that form these species from the breakdown of MB and n-butane.

We investigate soot precursor formation under similar conditions as we do for oxygenated species. To iterate, our analysis focuses on shock tube oxidation of both fuels at a pressure of 4 atm and temperatures of 1100K and 1600K. However, to enhance the amount of acetylene production in the system, we choose an equivalence ratio of 3, consistent with a prior soot formation study performed by Westbrook et al.[6].
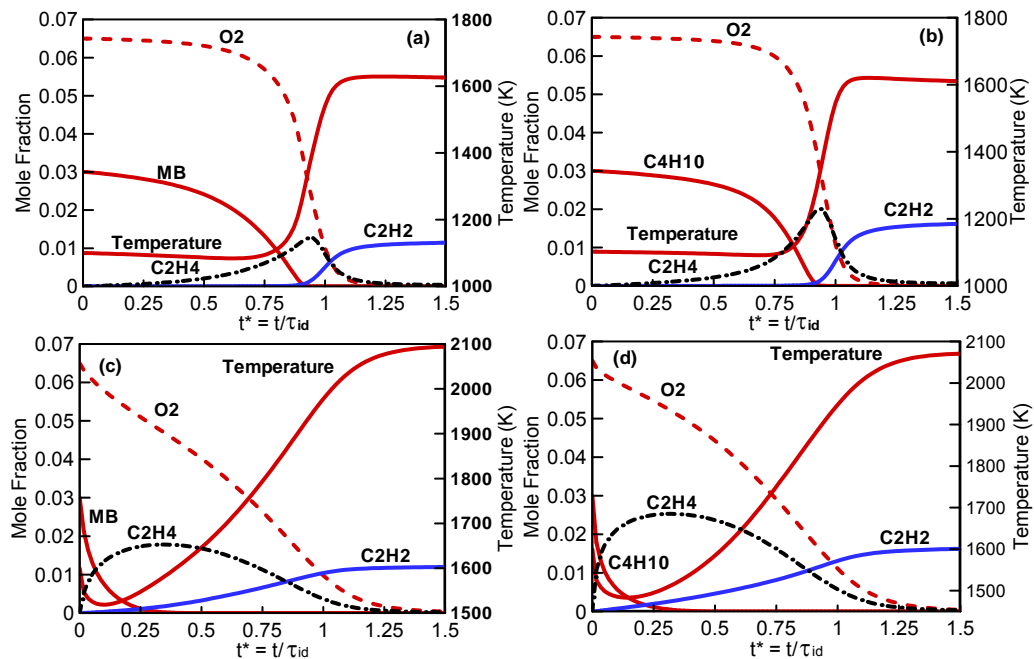
Figure 1.16. Temperature and concentration profiles of selected species for shock tube oxidation at P = 4 atm, ϕ = 3 (1% Fuel, 6.5% O2, 92.5% N2): t^* = t/τ_{id}; (a) MB at T = 1100K, τ_{id} = 0.00615s; (b) n-butane at T = 1100K, τ_{id} = 0.00645s; (c) MB at T =1600K, τ_{id} = 8.6×10^{-5}s (d) n-butane at T = 1600K, τ_{id} = 8.8×10^{-5}s .

Figure 1.16 compares the oxidation of n-butane and methyl butanoate at 1100K and 1600K; the plots show the time history of the temperature of the system, as well as the concentration of fuel, oxygen, ethylene and acetylene. Ethylene is an important species because it yields acetylene through hydrogen abstraction reactions. At 1100K, there is insignificant acetylene production until around the time of ignition. However, the concentration of ethylene grows significantly prior to ignition; subsequently, the ethylene mole fraction decreases on the same time scale as the increase in acetylene concentration. Rate of production analysis at $t^* = 1$ shows that ethylene forms a significant portion of acetylene by hydrogen abstraction through the ethenyl radical (C_2H_3); specifically, $C_2H_4 + H = C_2H_3 + H_2$ (R504), followed by $C_2H_3 + H = C_2H_2 + H_2$ (R503).

Thus, the reaction pathways forming ethylene from the decomposition both fuels are keys in the context of soot precursor formation. Figures 1.17 and 1.18 show these pathways for both fuels at 1100K and 1600K, respectively. For both fuels, the decomposition of fuel alkylester or alkyl radicals, themselves created by hydrogen abstraction, contributes the most to ethylene formation. In the case of MB, these radicals are MB4J, MBMJ and MB2J, while in the case of n-butane, these radicals are pC_4H_9 and sC_4H_9. The effect of fuel-bound oxygen is apparent in the decomposition of these radicals, inasmuch as the pathways that lead to ethylene from MB are related to those that form oxygenated species. For example, MB follows a pathway through MB2J that leads to ethylene, but which also produces the methoxy formyl radical (CH_3OCO). We previously observed that CH_3OCO produces CO_2 from fuel-bound oxygen and thus has a role in soot reduction. This channel is consistent

with previously postulated and observed soot reduction channels[6]. Figure 1.17 also shows that MB4J undergoes β-scission to form ME2J and C_2H_4 and that analogously, pC_4H_9 forms C_2H_5 and C_2H_4. As we have discussed, ME2J leads to CO and CO_2, but C_2H_5 produces C_2H_4 via hydrogen abstraction. Therefore, the net effect of the methyl ester is to divert the production of C_2H_5 to ME2J, leading to oxygenated products. In this way, this result illustrates another soot reducing mechanism of the methyl ester structure.
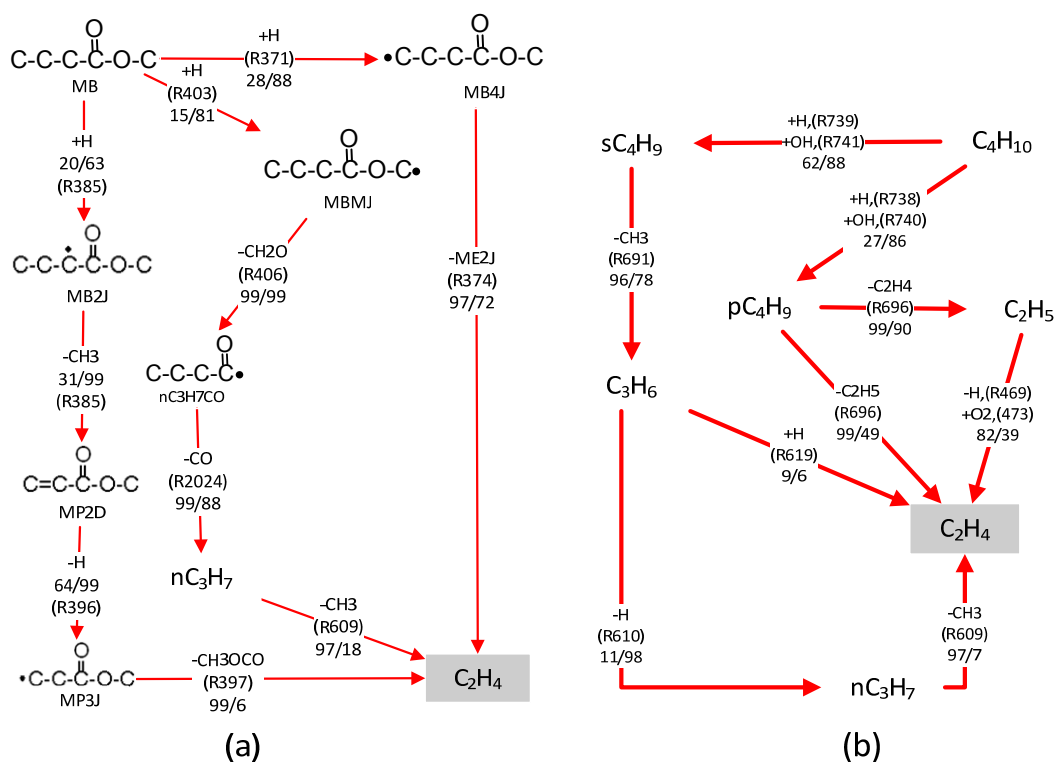
Figure 1.17. Reaction pathways forming ethylene from each fuel at T = 1100K and 30% fuel consumption. (a) methyl butanoate; (b) n-butane. The notation "A/B" denotes that A% of the reactant produces B% of the product in the specified reaction channel.

Reaction pathways at 1600K, shown in Figure 1.18, illustrate additional pathways for soot production that reflect the enhancement of unimolecular decomposition reactions by temperature. Similarly to observations at 1100K, a
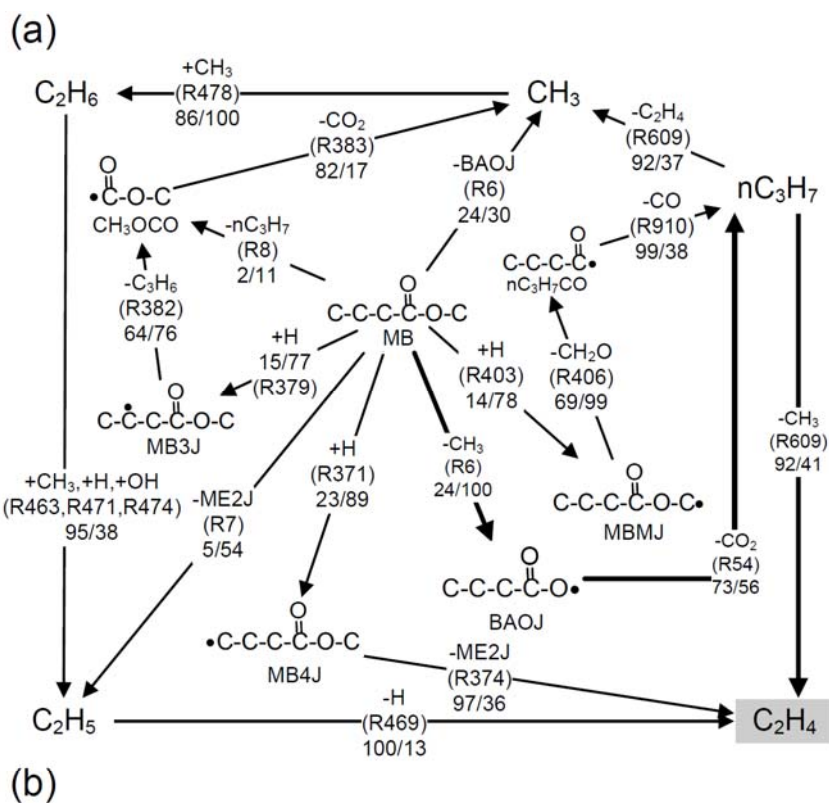
Figure 1.18. Reaction pathways forming ethylene from each fuel at T = 1600K and 30% fuel consumption. (a) methyl butanoate; (b) n-butane. The notation "A/B" denotes that A% of the reactant produces B% of the product in the specified reaction channel.

portion of MB follows a pathway through ME2J, indicating that some fuel

carbon is diverted from soot precursor formation. As well, the methoxy formyl radical is also involved at this temperature. The butanoic acid radical (BAOJ) becomes important at this temperature and directly forms CO_2 and nC_3H_7 via a bond breaking reaction (R54). This formation of CO_2 removes potential fuel carbon for available soot precursor formation, which is another pathway that has been previously observed.

A consequence of these pathways is the formation of the methyl radical, CH_3. The methyl radical is produced from: thermal decomposition of CH_3OCO to CO_2 and CH_3; and the decomposition of MB to BAOJ and CH_3; and β-scission of nC_3H_7 to form C_2H_4 and CH_3. The abundance of CH_3 enhances the recombination reaction $2CH_3 = C_2H_6$. Ethane (C_2H_6) undergoes successive hydrogen abstraction abstractions to form ethylene. Thus, fuel carbons in alkylester radicals that are not bonded directly to oxygen may still manifest in soot emissions through this pathway.

Our analysis elucidates the mechanism for soot precursor reduction in MB oxidation. Previous literature has suggested that MB wastes fuel-bound oxygen through direct CO_2 formation, as ideally, each fuel-bound oxygen should remove one carbon atom from soot precursor formation. In our discussion of the results of Figure 1.15, direct CO_2 production certainly represents a substantial portion of fuel-originated oxygenated species, but the classification as wasteful is merely a matter of perspective. Moreover, we observe additional reaction channels, namely those that produce CO, which split fuel-bound oxygen between two different carbons. Ultimately, MB represents a significant amount of soot precursor reduction when compared with n-butane, which is unequivocally positive.

1.5. Conclusions

The MBUMv2 mechanism is able to correctly predict the concentration profiles of CO_2 in pyrolysis conditions as well as ignition delay time in oxidation conditions, thus giving a better chemical insight of combustion/pyrolysis of MB. Such results are encouraging, and this mechanism can be used as a basis for future implementations of the kinetics of biodisel esters.

The kinetic modeling comparison of methyl butanoate and n-butane has illustrated a number of phenomena that can be ascribed to the oxygenated group present in methyl butanoate and other methyl esters. The methyl ester moiety changes the pathways that occur during methyl butanoate oxidation compared with n-butane. Most notably, methyl butanoate does not exhibit a region of NTC behavior, in contrast with n-butane. Sensitivity and reaction pathway analysis in the low temperature regime show that this phenomenon can be ascribed to the effect of the methyl ester, whose asymmetrical structure enables 5-membered isomerization pathways that inhibit reactivity.

As well, we observe that the fuel-bound oxygen contained in the methyl ester moiety leads to significant production of both carbon monoxide and carbon dioxide, which cannot occur in the combustion of n-butane. In addition to previously studied pathways that formed CO_2, we also find an additional pathway through the methyl ethanoate radical that leads to the formation of carbon monoxide. These reaction channels, as expected, are related to those that lead to the formation of soot precursors, namely ethylene and acetylene. These pathways account for the reduction in soot precursor production associated with methyl butanoate oxidation when compared to n-butane. Production of oxygenated radicals, such as methyl ethanoate radicals (ME2J),

displaces the production of alkyl radicals when compared to n-butane. Since these oxygenated radicals preferentially form oxygenated species, a reduction in soot precursor formation logically follows.

In the future, it will be useful to know how these predictions scale with molecule size, as the effects of the methyl ester moiety will be expected to decrease with increasing alkyl chain length. Other studies, for example, have predicted NTC behavior for larger methyl esters such as methyl decanoate[29]. Larger methyl esters and biodiesel have exhibited lower soot emissions, which suggest that the methyl ester continues to have a beneficial effect. Ultimately, contrasting biodiesel combustion with conventional hydrocarbon fuels will help to elucidate the changes in performance as biodiesel displaces conventional diesel in fuel blends. Understanding these changes will ideally facilitate the design of combustion technologies.

CHAPTER 2

COMPUTATIONAL FLUID DYNAMICS STUDY OF NANOFLUID HEAT TRANSFER

2.1. Introduction

Heat transfer materials like water, ethylene glycol, engine oil, alumina, copper, and silver as cooling or heating process have been widely used in numerous important fields, such as heating, ventilating, air-conditioning system, micro-electronics, transportation, manufacturing, and nuclear engineering. Cooling or heating performances for thermal systems play a vital role in the development of energy-efficient heat transfer equipments, such as MEMS and NEMS (Micro and Nano Electro Mechanical Systems, respectively). Over the last years, it has been demonstrated that thermal conductivity of fluids containing metallic nanoparticles (nanofluids) is significant higher than that of pure fluids[30,31]. Additional benefits of nanofluids include high stability with low sedimentation, no clogging in micro-channels, reduction in pumping power and design of small heat exchanger systems[32].

A great amount of experimental research in this field has been recently reported in the literature. Eastman et al.[33] observed that Al_2O_3/water and CuO/water with 5% nanoparticle volume fraction increased the thermal conductivity by 29% and 60%, respectively. In addition, Xie et al.[34] showed that Al_2O_3/ethylene glycol of 5% nanoparticle volume fraction enhanced thermal

conductivity by 30%. Patel et al.[35] reported that Au/toluene and Au/water with 0.0013-0.011% nanoparticle volume fraction increased the thermal conductivity by 4-7% and 3.2-5%, respectively.

To explain the observed phenomena, many theoretical studies on the effective thermal conductivity in nanofluids have been proposed over the past few years and the various models can be grouped in two main categories[32]. The first one includes a static model for heat conductivity with stationary nanoparticles in multiphase systems, while the second group is based on a dynamic model for heat conductivity. Recently, Xu et al.[36] derived a new model to describe the heat conduction of nanofluids, based on the fractal distribution of nanoparticles and Brownian motion of nanoparticles for the heat convection between solids and liquids.

On the other hand, research conducted by different groups on heat transfer characteristics of nanofluids has shown little agreement[32]. In the natural convection of nanofluids inside a horizontal cylinder, Putra et al.[37] observed the paradoxical behavior of heat transfer due to different particle concentrations, types of the particles and different shapes of the containing cavity. Kim et al.[38] analyzed the convective instability driven by buoyancy and heat transfer characteristics of nanofluids and indicated that as the thermal conductivity and shape factor of nanoparticles decrease, the convective motion in a nanofluid sets in easily. In a laminar tube flow, Wen and Ding[39] showed the local heat transfer coefficient increased 41% and 46 % at *Re* = 1050 and 1600, respectively in the presence of nanoparticle volume fraction of 0.016. Jung et al.[40] reported that the heat transfer coefficient increased by 32% by dispersing 1.8% nanoparticles in a micro-rectangular channel with

Al_2O_3/water nanofluid. The computational studies reported in this area include two main approaches: (1) a two-phase model, in which both liquid and solid heat transfer behaviors are solved in the flow fields[41,42], and (2) a single-phase model, in which solid particles are considered to behave as a fluid, because the size of particles is small and easy to be fluidized[43-48]. The model of nanofluids in a cavity was first proposed by Khanafer et al.[43] and the authors investigated the natural convection effect on the enhancement of heat transfer. Tiwari et al.[44] further studied the forced convection effect with two-sided lid-driven differentially heated square cavity. A theoretical study on a heated cavity reported by Hwang et al.[49] showed that the heat transfer coefficient of Al_3O_2/water nanofluid is reduced when there is an increase in size of nanoparticles and a decrease in average temperature. Recently, Ho et al.[47] adopted four different models from the literature for effective viscosity and thermal conductivity of nanofluids, demonstrating the importance of dynamic viscosity.

In summary, the current computational studies show two limitations: the diameters of the nanoparticles suspended in the fluids are held as uniform and the thermal conductivity models adopted are independent of temperature. In one of the recent experimental studies[50], the authors indicated that the effect of temperature may play an important role in changing the effective thermal conductivity. Prompted by these considerations, in this study we address the effect of non-uniform nanoparticle size and temperature on Al_2O_3/water nanofluid to simulate natural convection in a square cavity. The thermal conductivity and the dynamic viscosity of the nanofluid are employed by Xu's model[36] and Jang's model[51], respectively. The Navier-Stokes and energy

equations are coupled with the nanoparticle fractal distributions, mean nanoparticle diameters, nanoparticle volume fraction, Prandtl number, and Grashof number to produce a systematic description of the phenomenon. Therefore, the findings of this study provide more information on the heat transfer characteristic of nanofluids and extend the parameters of the previously published enclosure model of Khanafer et al.[43].

2.2. Mathematical formulation

Figure 2.1 shows the schematic of the model adopted in this study. The origin of the Cartesian coordinate system is at the left corner of the bottom wall located at $y = 0$. The aspect ratio of this enclosure is defined as L/H and is assumed to be unity. Initially, the cavity is filled with Al_2O_3/water nanofluid at
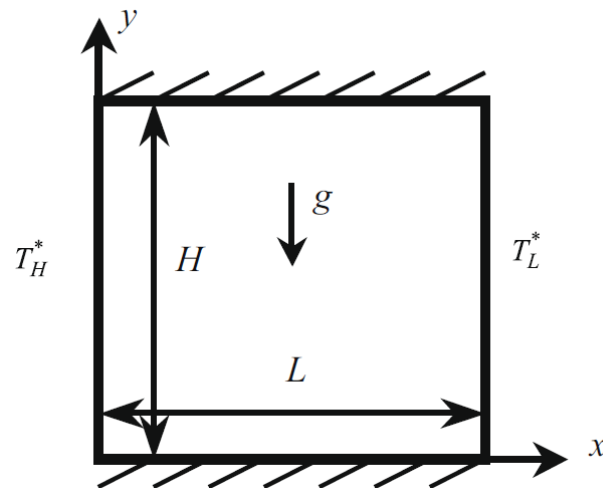
Figure 2.1. Schematic for the physical model with boundary conditions of the problem.

rest. Fluid motion is then induced by the buoyancy force with the temperature difference between two vertical walls at $x = 0$ and $x = L$. Hot and cold temperatures are kept continuously into the cavity via the vertical walls where

nanofluid temperature assumes the prescribed cold temperature $T^* = T_L^*$. The horizontal walls are adiabatic and impermeable to mass transfer. For the velocity field, the no-slip and no penetration conditions are imposed on the walls.

2.2.1. Assumptions

The mathematical equations describing the physical model are based on the following assumptions: (I) the thermophysical properties are constant except for the density in the buoyancy force (Boussinesq's hypothesis); (II) the fluid phase and nanoparticles are in a thermal equilibrium state; (III) nanoparticles are spherical and uniformly distributed in water; (IV) the variation of the number density in a particle size range of 5 to 250 nm follows a normal distribution; (V) the nanofluid in the cavity is Newtonian, incompressible, and laminar; and (VI) radiation heat transfer between the sides of the cavity is negligible when compared with the other mode of heat transfer.

2.2.2. Governing equations

The governing equations in dimensional form used in the present study are:

Continuity equation:

$$\frac{\partial u^*}{\partial x^*} + \frac{\partial v^*}{\partial y^*} = 0 \tag{1}$$

x-momentum equation:

$$\frac{\partial u^*}{\partial t^*} + u^* \frac{\partial u^*}{\partial x^*} + v^* \frac{\partial u^*}{\partial y^*} = \frac{-1}{\rho_{nf}} \frac{\partial p^*}{\partial x^*} + \frac{\mu_{eff}}{\rho_{nf}} \left(\frac{\partial^2 u^*}{\partial x^{*2}} + \frac{\partial^2 u^*}{\partial y^{*2}} \right) \tag{2}$$

y-momentum equation:

$$\frac{\partial v^*}{\partial t^*} + u^* \frac{\partial v^*}{\partial x^*} + v^* \frac{\partial v^*}{\partial y^*} = \frac{-1}{\rho_{nf}} \frac{\partial p^*}{\partial y^*} + \frac{\mu_{eff}}{\rho_{nf}} \left(\frac{\partial^2 v^*}{\partial x^{*2}} + \frac{\partial^2 v^*}{\partial y^{*2}} \right)$$
$$+ \frac{1}{\rho_{nf}} \left[(1-\phi)\rho_f \beta_f + \phi \rho_s \beta_s \right] g \left(T^* - T_L^* \right) \tag{3}$$

Energy equation:

$$\frac{\partial T^*}{\partial t^*} + u^* \frac{\partial T^*}{\partial x^*} + v^* \frac{\partial T^*}{\partial y^*} = \alpha_{nf} \left(\frac{\partial^2 T^*}{\partial x^{*2}} + \frac{\partial^2 T^*}{\partial y^{*2}} \right) \tag{4}$$

Vorticity equation and stream function:

$$\omega = \frac{\partial v^*}{\partial x^*} - \frac{\partial u^*}{\partial y^*} = -\left(\frac{\partial^2 \psi^*}{\partial x^{*2}} + \frac{\partial^2 \psi^*}{\partial y^{*2}} \right) \tag{5}$$

The effective physical properties of the nanofluid in the above equations are:

1. Viscosity:

$$\mu_{eff} = \mu_f (1 + 2.5\phi) \left[1 + \eta \left(\frac{d_p}{H} \right)^{-2\varepsilon} \phi^{2/3} (\varepsilon + 1) \right] \tag{6}$$

This well-validated model is presented by Jang et al.[51] for a fluid of viscosity containing a dilute suspension of small rigid spherical particles and accounting for the slip mechanism in nanofluids. The empirical constant ε and η are -0.25 and 280 for Al_2O_3, respectively.

2. Density:

$$\rho_{nf} = (1-\phi)\rho_f + \phi \rho_s \tag{7}$$

3. Heat capacitance:

$$\left(\rho C_p \right)_{nf} = (1-\phi) \left(\rho C_p \right)_f + \phi \left(\rho C_p \right)_s \tag{8}$$

4. Thermal diffusivity:

$$\alpha_{nf} = k_{nf} / \left(\rho C_p \right)_{nf} \tag{9}$$

5. Dimensionless stagnant thermal conductivity:

$$\frac{k_{stationary}}{k_f} = \frac{k_s + 2k_f - 2\phi(k_f - k_s)}{k_s + 2k_f + \phi(k_f - k_s)} \tag{10}$$

This model, introduced by Hamilton et al.[52], considers the nanoparticles in the liquid as stationary.

6. Total dimensionless thermal conductivity of nanofluids:

$$\frac{k_{nf}}{k_f} = \frac{k_{stationary}}{k_f} + \frac{k_c}{k_f} = \frac{k_s + 2k_f - 2\phi(k_f - k_s)}{k_s + 2k_f + \phi(k_f - k_s)}$$

$$+ c\frac{Nu_p d_f}{Pr} \frac{(2 - D_f)D_f}{(1 - D_f)^2} \frac{\left[\left(\frac{d_{max}}{d_{min}}\right)^{1 - D_f} - 1\right]^2}{\left(\frac{d_{max}}{d_{min}}\right)^{2 - D_f} - 1} \frac{1}{d_{avg}} \tag{11}$$

This model was proposed by Xu et al.[36] and it has been chosen to describe the thermal conductivity of nanofluids. The first term is the H-C model and the second term is the thermal conductivity based on heat convection due to Brownian motion. c is an empirical constant, which is relevant to the thermal boundary layer and dependent on different fluids (e.g. c = 85 for the deionized water and c = 280 for ethylene glycol) but independent of the type of nanoparticles. Nu_p is the Nusselt number for liquid flowing around a spherical particle and equal to two for a single particle in this work. The fluid molecular diameter d_f is taken as 4.5×10^{-10} m for water in this work. The Pr is the Prandtl number, ϕ and d_{avg} are the nanoparticle volume fraction and mean nano-particle diameter, respectively. The fractal dimension D_f is determined by

$$D_f = 2 - \frac{\ln\phi}{\ln(d_{min}/d_{max})} \tag{12}$$

where d_{max} and d_{min} are maximum and minimum diameter of nanoparticles, respectively. With the given/measured ratio of d_{min}/d_{max}, the minimum and maximum diameter of nanoparticles can be obtained with mean nanoparticle

diameter (d_{avg}) and ratio of minimum to maximum diameters from the statistical property of fractal media.

$$d_{max} = d_{avg} \cdot \frac{D_f - 1}{D_f} \cdot \left(\frac{d_{min}}{d_{max}} \right)^{-1} \qquad (13)$$

$$d_{min} = d_{avg} \cdot \frac{D_f - 1}{D_f} \qquad (14)$$

By scaling the dimensional variables, the dimensionless form of governing equations can be obtained using the following parameters:

$$x = \frac{x^*}{H}, \; y = \frac{y^*}{H}, \; u = \frac{u^*}{\alpha_f / H}, \; v = \frac{v^*}{\alpha_f / H}, \; t = \frac{\alpha_f t^*}{H^2}, \; p = \frac{p^*}{\rho_f \left(\alpha_f / H \right)^2}, \; T = \frac{T^* - T_L^*}{T_H^* - T_L^*},$$

$$\Omega = \frac{\omega H^2}{\alpha_f}, \; \psi = \frac{\psi^*}{\alpha_f}$$

Variables t, u, v, p, T, Ω, ψ are time, velocity components in x- and y-direction, pressure, temperature, vorticity, and streamline function, respectively.

The 2-D dimensionless equations for the conservation of total mass, momentum, and energy of the nanofluid can be written as:

Continuity equation:

$$\frac{\partial u}{\partial x} + \frac{\partial v}{\partial y} = 0 \qquad (15)$$

x-momentum equation:

$$\frac{\partial u}{\partial t} + u \frac{\partial u}{\partial x} + v \frac{\partial u}{\partial y} = \frac{-\rho_f}{\rho_{nf}} \frac{\partial p}{\partial x} + \frac{\mu_{eff}}{\rho_{nf} \nu_f} \frac{\Pr}{} \left(\frac{\partial^2 u}{\partial x^2} + \frac{\partial^2 u}{\partial y^2} \right) \qquad (16)$$

y-momentum equation:

$$\frac{\partial v}{\partial t} + u \frac{\partial v}{\partial x} + v \frac{\partial v}{\partial y} = \frac{-\rho_f}{\rho_{nf}} \frac{\partial p}{\partial y} + \frac{\mu_{eff}}{\rho_{nf} \nu_f} \frac{\Pr}{} \left(\frac{\partial^2 v}{\partial x^2} + \frac{\partial^2 v}{\partial y^2} \right) + \frac{(1 - \phi) \rho_f \beta_f + \phi \rho_s \beta_s}{\rho_{nf} \beta_f} \Pr^2 GrT$$

where $Gr = g\beta_f \left(T_H^* - T_L^*\right)H^3 / \upsilon_f^2$ is the Grashof number and defined as the ratio of the buoyancy to viscous force.

Energy equation:

$$\frac{\partial T}{\partial t} + u\frac{\partial T}{\partial x} + v\frac{\partial T}{\partial y} = \frac{\alpha_{nf}}{\alpha_f}\left(\frac{\partial^2 T}{\partial x^2} + \frac{\partial^2 T}{\partial y^2}\right) \tag{18}$$

Vorticity equation and stream function:

$$\Omega = \frac{\partial v}{\partial x} - \frac{\partial u}{\partial y} = -\left(\frac{\partial^2 \psi}{\partial x^2} + \frac{\partial^2 \psi}{\partial y^2}\right) \tag{19}$$

The initial conditions are:

$u = v = T = \psi = 0$ at $t = 0$ (20)

and the boundary conditions applied at t > 0 can be summarized as follows:

$u = v = \psi = \dfrac{\partial T}{\partial y} = 0$; at $y = 0$ and 1 for 0 < x < 1,

$T = 1$, $u = v = \psi = 0$; at $x = 0$ for $0 \leq y \leq 1$,

$T = 0$, $u = v = \psi = 0$; at $x = 1$ for $0 \leq y \leq 1$ (21)

2.2.3. Nusselt number

The Nusselt number, *Nu*, is expected to depend on a number of factors such as thermal conductivity, heat capacitance, viscosity, and flow structure of nanofluids, and volume fraction, dimensions, and fractal distributions of nanoparticles. The local variation of the Nusselt number of the fluid can be expressed as:

$$Nu = -\frac{k_{nf}}{k_f}\frac{\partial T}{\partial x} \tag{22}$$

By integrating the local Nusselt number over the left wall, the average Nusselt

number along the left wall is given as:

$$\overline{Nu} = \int_0^1 Nu\,dy \tag{23}$$

2.3. Numerical method

Equations 15-19 are discretized on a structured grid. The velocity components (u, v) and the scalar variables (pressure, temperature, vorticity, and streamline function) are located at the center of the control volume in a non-staggered manner. The governing equations are solved numerically by a weighting function scheme[53]. The Non-Staggered Artificial Pressure for Pressure-Linked Equation (NAPPLE) algorithm[54] is used to convert the continuity Eq. (15) into a pressure linked equation. Compared with other algorithms of staggered grid systems, this method has the advantage of high computational efficiency and simple grid structure. The solutions of discretized equations are obtained using a Semi-Implicit Solver (SIS)[55] and iterated until convergence. θ_{new} are the new solutions obtained from the SIS iteration and θ_{max} and θ_{min} are the maximum and minimum values of θ_{new}. The prescribed tolerance TOL = 10^{-6} is defined as:

$$\underset{k=1...m}{Max}\left|\frac{\theta_{k,new} - \theta_{k,old}}{\theta_{max} - \theta_{min}}\right| \leq TOL \tag{24}$$

where m is the last point in the computational domain. For a better convergence rate, the guess solution θ_k is modified by employing a successive over-relaxation (SOR) factor:

$$\theta_{k+1} = \theta_k + SOR\left(\theta_{k+1} - \theta_k\right) \tag{25}$$

At each time step, the converged solution is used as the initial condition for the following time step. The method employed to solve the time differential terms

49

is an unconditionally stable fully implicit scheme.

2.4. Algorithm validation

The validity of the numerical approach has been assessed by grid-independence and by comparisons with the results in the literature on steady 2-D square cavity flows of buoyancy-driven laminar heat transfer. To capture the rapid changes in the dependent variables, in this study we implement the non-uniform grid system with more nodes accumulated near the walls. Different non-uniform grids of 41×41, 81×81, 121×121, and 161×161 are examined for $Gr = 10^5$, $Pr = 6$, $\phi = 0.05$, $d_{avg} = 5$ nm, and $d_{min}/d_{max} = 0.001$ and we observe that the further refinement from 121×121 grid is not necessary. The average Nusselt number is 9.45, 9.51, 9.52, and 9.52 for 41×41, 81×81, 121×121, and 161×161 points, respectively. Therefore, a 121×121 grid is chosen to calculate the flow and heat transfer behavior over the range of operational parameter values considered.

To ensure the accuracy and validity of the new model, we analyze a system composed of pure fluid in an enclosure with $Pr = 0.7$ and different Ra numbers. This system has been studied by other research groups, including Tiwari and Das[44], Davis[56], Markatos and Pericleous[57], and Hadjisophocleous et al.[58]. Table 2.1 shows the comparison between the results obtained with the new model and the values presented in the literature. The quantitative comparisons for the average Nusselt numbers along the hot wall and the maximum velocity values and their corresponding locations indicate an excellent agreement. In addition, we investigate a differentially heated square enclosure with different volume fractions of nanoparticles and compared the

Table 2.1. Comparison of pure fluid solutions with previous works in an enclosure for Pr = 0.7 with different Rayleigh numbers.

	Present	Tiwari And Das[44]	Davis[56]	Markatos and Pericleous[57]	Hadjisophocleous et al.[58]
(a)$Ra = 10^3$					
u_{max}	3.597	3.642	3.649	3.544	3.544
y	0.819	0.804	0.813	0.832	0.814
v_{max}	3.690	3.7026	3.697	3.593	3.586
x	0.181	0.178	0. 178	0.168	0.186
$\overline{Nu}$	1.118	1.0871	1.118	1.108	1.141
(b)$Ra = 10^4$					
u_{max}	16.158	16.1439	16.178	16.18	15.995
y	0.819	0.822	0.823	0.832	0.814
v_{max}	19.648	19.665	19.617	19.44	18.894
x	0.112	0.110	0.119	0.113	0.103
$\overline{Nu}$	2.243	2.195	2.243	2.201	2.29
(c)$Ra = 10^5$					
u_{max}	36.732	34.30	34.73	35.73	37.144
y	0.858	0.856	0.855	0.857	0.855
v_{max}	68.288	68.7646	68.59	69.08	68.91
x	0.063	0.05935	0.066	0.067	0.061
$\overline{Nu}$	4.511	4.450	4.519	4.430	4.964
(d)$Ra = 10^6$					
u_{max}	66.46987	65.5866	64.63	68.81	66.42
y	0.86851	0.839	0.85	0.872	0.897
v_{max}	222.3395	219.7361	217.36	221.8	226.4
x	0.03804	0.04237	0.0379	0.0375	0.0206
$\overline{Nu}$	8.757933	8.803	8.799	8.754	10.39
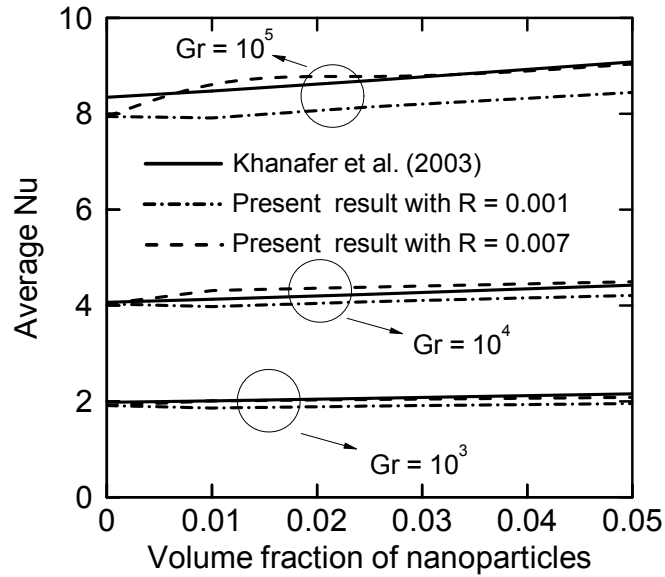
Figure 2.2. Comparison of average Nusselt numbers between Khanafer et al.[43] and present result for $Pr = 6.2$ and $d_{avg} = 10$ nm with $Gr = 10^3$, $Gr = 10^4$, and $Gr = 10^5$.

average Nu numbers obtained with the new model with the results reported in the literature by Khanafer et al.[43]. As shown in Figure 2.2, the new model is able to reproduce previous results and the effect of non-uniform nanoparticle size.

In order to evaluate the effectiveness of Xu's model, Figure 2.3 shows the characteristic of the effective thermal conductivity, which is a function of the practical parameters including $R = d_{min}/d_{max}$, d_{avg} and Prandtl number. In the Figure 2.3 (a), it is found that R has a relatively large effect for small mean nanoparticle diameters. Besides, from the Eq. (11), the temperature effect of nanofluids is described in terms of Prandtl number. As shown in Figure 2.3 (b), the Prandtl numbers are 6 and 2.66 for temperature 300 and 340K, respectively and consequently the presence of nanoparticles has a strong effect on heat conductivity of the nanofluid at high temperature. Thus, compared with the traditional H-C model with the assumption of uniform
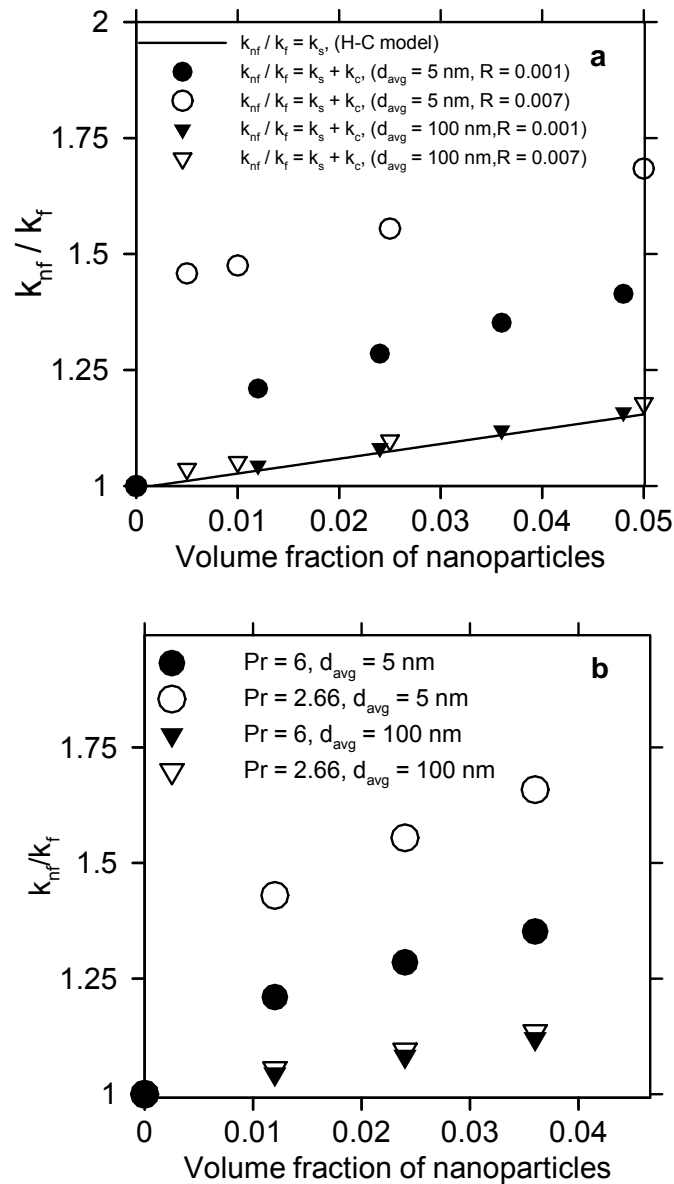
Figure 2.3. Dimensionless effective thermal conductivity of Al_2O_3/water nano-fluid versus volume fraction (ϕ) of nanoparticles with different mean nano-particle diameters and fractal distributions: (a) Pr = 6 and (b) R = 0.001.

nanoparticle size, Xu's model including more variables related to nanofluids shows better flexibility in predicting the heat transfer characteristic.

2.5. Results and discussion

As stated in the previous sections, the overall objective of this current investigation is to explore the heat transfer behavior of natural convection

inside a cavity with Al_2O_3/water based nanofluid. Specifically, we will analyze steady-state flow fields, temperature fields, and heat transfer rate for various values of the Grashof number, Prandtl number, ratio of minimum to maximum nanoparticle diameter, mean nanoparticle diameter, and nanoparticle volume fraction. As reported in various studies[36,43-46,51], the ranges of variation of these parameters are $10^3 \leq Gr \leq 10^6$, $2.66 \leq Pr \leq 6$, $0.001 \leq R \leq 0.007$, 5 nm $\leq d_{avg} \leqslant$ 250 nm, and $0 \leqslant \phi \leqslant 0.05$. Table 2.2 shows the thermophysical properties of fluid and solid phases.

Table 2.2. Thermophysical properties of different phases.

Properties	Fluid phase (Water, 300K)	Fluid phase (Water, 340K)	Solid phase (Al_2O_3)
c_p (J/kg-K)	4179	4188	850
ρ (kg/m^3)	997.1	879.4	3900
k (W/m-K)	0.61	0.66	46
β (K^{-1})	2.1×10^{-4}	5.66×10^{-4}	1.67×10^{-5}

The results below are organized as follows. In section 2.5.1 and 2.5.2, we report on effects of non-uniform nanoparticle diameters and mean nanoparticle diameter, respectively on the heat transfer. The effect of temperature on the nanofluid heat transfer is discussed in section 2.5.3 and the characteristics of the heat transfer as function of the nanoparticle fraction of the nanoparticles are analyzed in Section 2.5.4. Finally, Section 2.5.5 gives comparisons with the most recent experimental data.

2.5.1. Effect of non-uniform nanoparticle diameter

The effect of the fractal distributions on the heat transfer is reported below

in terms of the ratio of minimum to maximum nanoparticle diameters, while the mean diameter, nanoparticle volume fraction and Prandtl number are fixed at 5 nm, 5%, and 6, respectively. It is worth mentioning that from Eq. (12), the fractal dimension D_f derived from Brownian motion in the nanofluid is inversely proportional to $R = d_{min}/d_{max}$ and this implies that the R value provides a measure of the importance of the non-uniform nanoparticle structures. The steady-state variation of the velocity at the mid-section of the cavity is analyzed for $Gr = 10^4$ and $Gr = 10^5$.

(a) $Gr = 10^4$

(b) $Gr = 10^5$
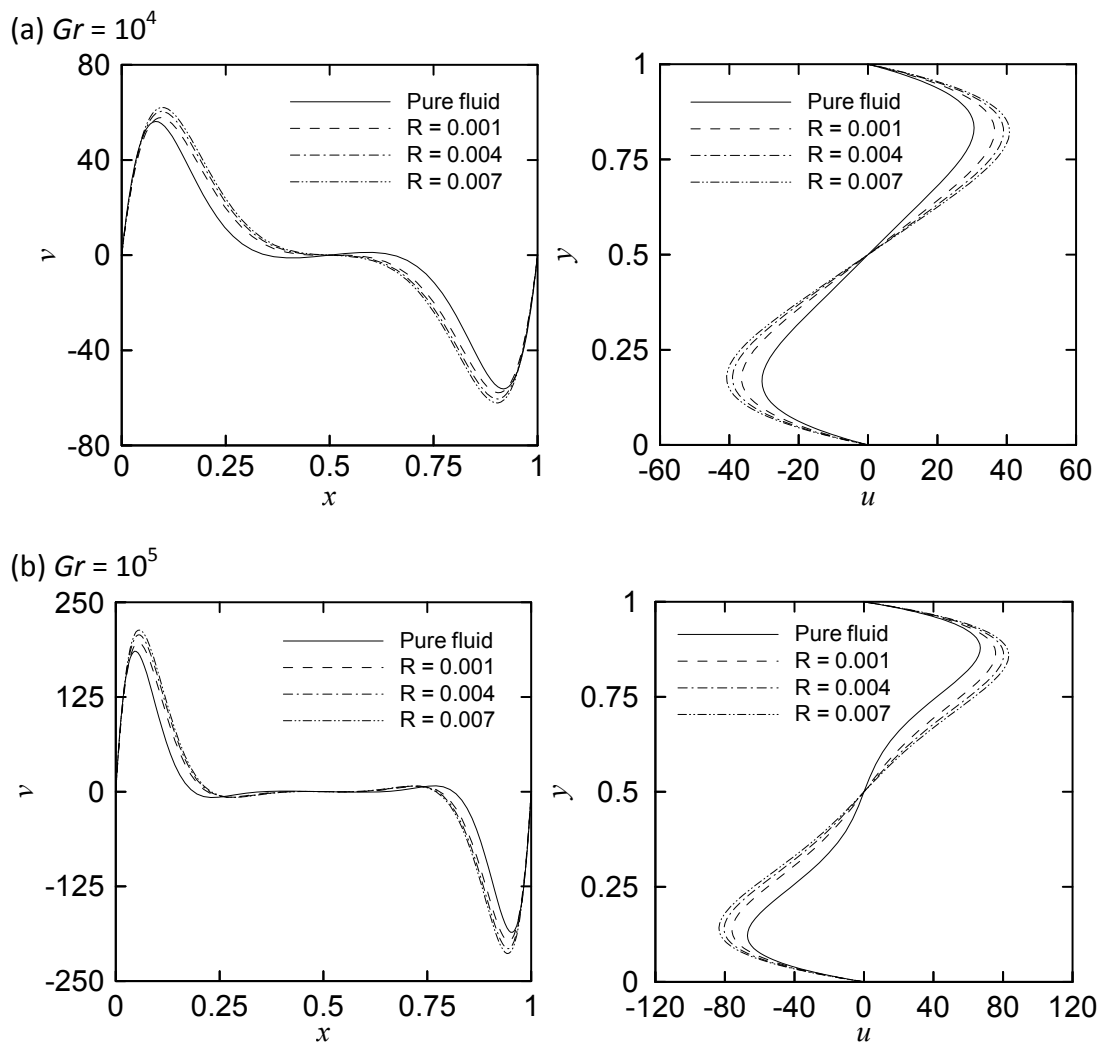
Figure 2.4. Velocity profiles at enclosure centerline for different values of $R = d_{min}/d_{max}$ with $Pr = 6$, $d_{avg} = 5$ nm, and $\phi = 0.05$.

(a) d_{max}= 1.807 µm, d_{min} = 1.807 nm, k_{nf}/k_f =1.424

(b) d_{max}= 0.203 µm, d_{min} = 1.419 nm, k_{nf}/k_f =1.684

(c) d_{max}= 1.807 µm, d_{min} = 1.807 nm, k_{nf}/k_f =1.424
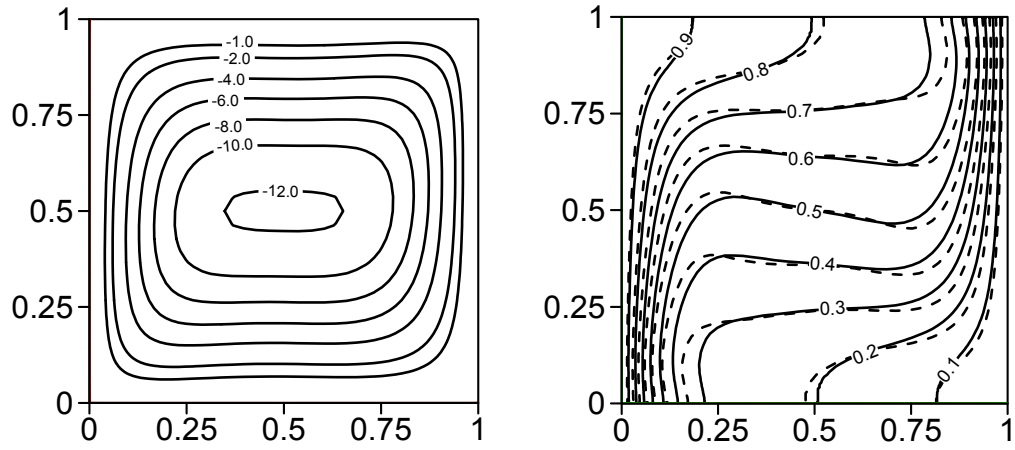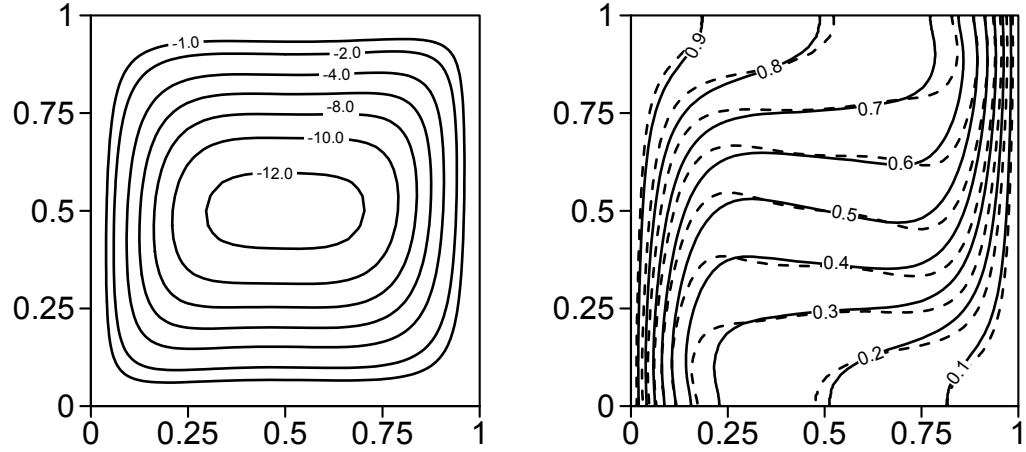
(d) $d_{max}= 0.203$ μm, $d_{min} = 1.419$ nm, $k_{nf}/k_f = 1.684$
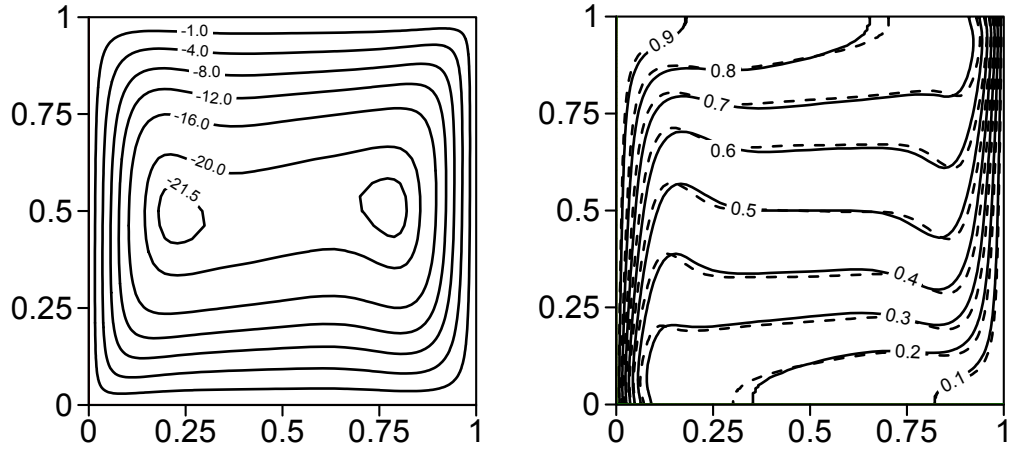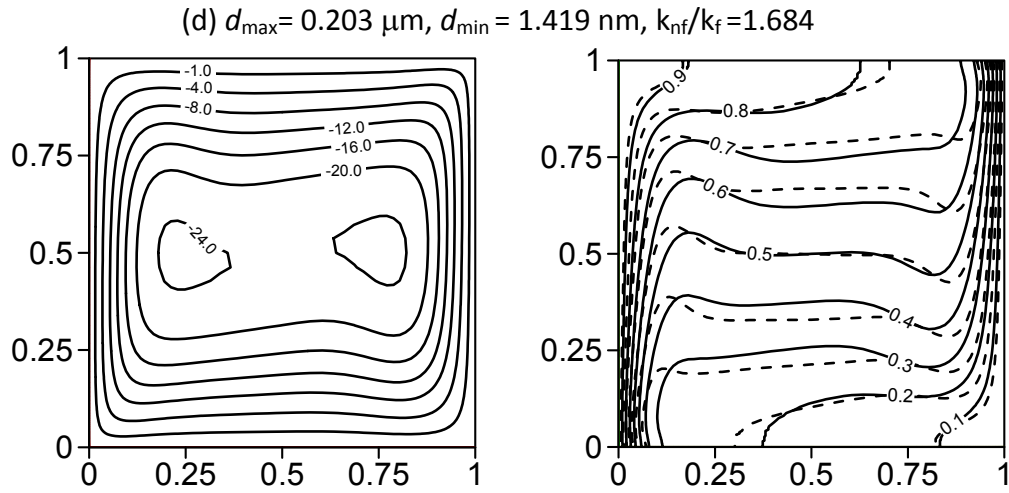
Figure 2.5. Streamlines and comparison of isotherm contours between nanofluids (—) and pure fluid (- - -) with different values of (a) $R = 0.001$, $Gr = 10^4$; (b) $R = 0.007$, $Gr = 10^4$; (c) $R = 0.001$, $Gr = 10^5$; (d) $R = 0.007$, $Gr = 10^5$ for $Pr = 6$, $d_{avg} = 5$ nm, and $\phi = 0.05$.

Figure 2.4 shows that the heat convection of the nanofluid increases remarkably with the uniformity of particle size (R) due to an increase in the energy transport through the fluid. The phenomenon can be explained based on the theory of Brownian motion that relates small particles to high velocity.

Figure 2.5 illustrates the effect of uniformity of particle size (R) on the steady-state variation of the streamlines and isotherms for $Gr = 10^4$ and $Gr = 10^5$. The intensity of flow activities was documented by recording the values of streamline contours. In this physical model, the flow patterns are characterized by a primary recirculating clockwise vortex that occupies the bulk of the cavity. As R increases from 0.001 to 0.007, the flow patterns remain quite the same with enhanced the absolute circulation strength due to relatively high velocity of the fluid flow. To explain this phenomenon, we determine the maximum and minimum diameters from Eq. (13 and 14). It is interesting to note that for a fixed mean nanoparticle diameter, the maximum and minimum diameter of

nanoparticles are both decreased by relatively high R values (Figure 2.5). This analysis basically implies that at a constant volume fraction, the heat convection is better enhanced by relatively small nanoparticles with more uniform size. Therefore, with these nanoparticle structures, the value of dimensionless thermal conductivity k_{nf}/k_f increases by 18.26% from $R = 0.001$ to 0.007. The comparisons of the pure fluid and nanofluid isotherms show that vertical stratification of the isotherms breaks down with an increase in R at relatively high Grashof numbers. This behavior can be attributed to the increase in contribution of thermal conductivity and gravity.
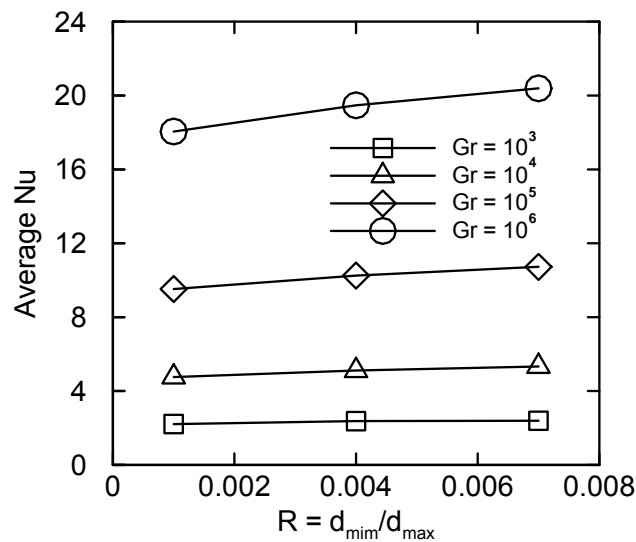
Figure 2.6. Variation of average Nu numbers with the ratio $R = d_{min}/d_{max}$ for constant values of Gr numbers with $Pr = 6$, $d_{avg} = 5$ nm, and $\phi = 0.05$.

The average Nusselt number for these conditions is calculated using Eq. (23) and the result reported in Figure 2.6 shows that the higher the Gr number, the larger the heat transfer. Over the range of R values studied, the average Nusselt number increases 7.9% and 12.94% for $Gr = 10^3$ and $Gr = 10^6$, respectively. As a consequence, the nanofluids enhance heat transfer in both

large and small buoyancy conditions.

2.5.2. Effect of mean nanoparticle diameter

To study the effect of the mean nanoparticle diameter on the heat transfer, we vary the diameter between 5 nm and 250 nm, while R, Pr, and ϕ are fixed at 0.001, 6, and 0.05, respectively. The results of velocity profiles are shown in Figure 2.7. As the mean nanoparticle diameter increases, the corresponding

(a) $Gr = 10^3$
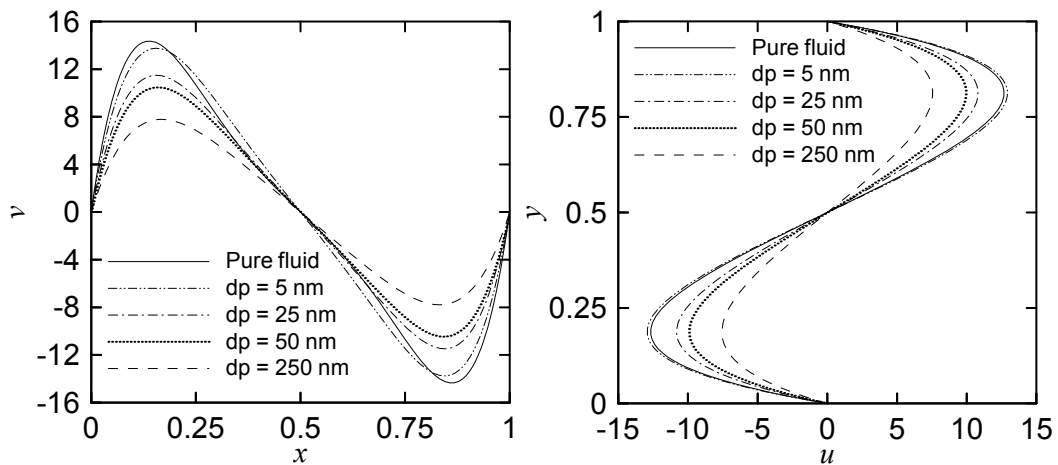
(b) $Gr = 10^6$
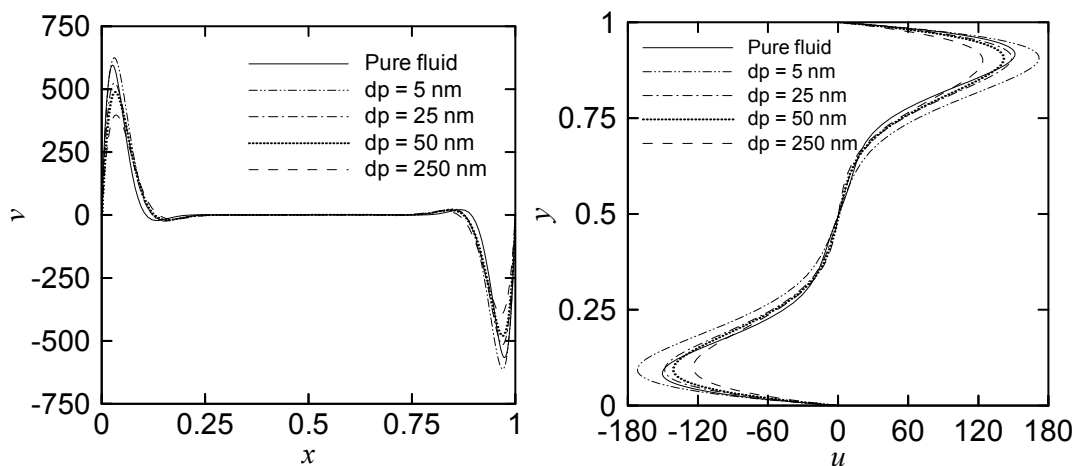
Figure 2.7. Velocity profiles at enclosure centerline for different values of d_{avg} with $Pr = 6$, $R = 0.001$, and $\phi = 0.05$.

flow velocity decreases and hence the heat transfer enhancement is reduced.

Notice that the fluids suspended with Al_2O_3 nanoparticles mitigate fluid flow in the cavity except for d_{avg} = 5 nm as compared to the pure fluid. This phenomenon is mainly caused by the effective dynamic viscosity, which dominates the heat transfer characteristic of nanofluid flow as the k_{nf}/k_f reaches unity.

Figure 2.8 shows the streamline and temperature contours for d_{avg} = 5 and 250 nm with Gr =10^3 and 10^6. Similarly to the results reported in Figure 2.5, the streamline patterns are not significantly affected by the mean nanoparticle diameters. However, the value of absolute circulation strength decreases with

(a) d_{max} = 1.807 μm, d_{min} = 1.807 nm, k_{nf}/k_f =1.424

(b) d_{max} = 90.391 μm, d_{min} = 90.391 nm, k_{nf}/k_f =1.157

(c) d_{max} = 1.807 μm, d_{min} = 1.807 nm, k_{nf}/k_f =1.424

(d) d_{max} = 90.391 μm, d_{min} = 90.391 nm, k_{nf}/k_f =1.157
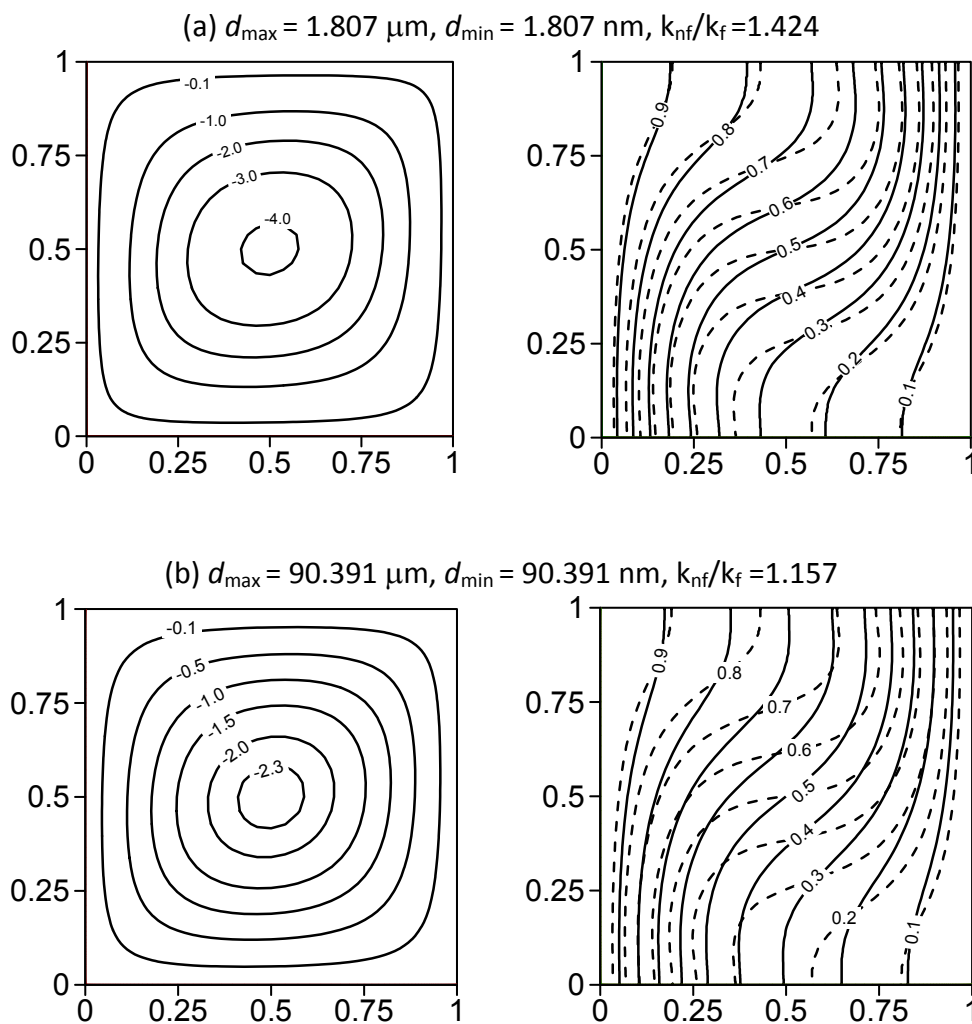
Figure 2.8. Streamlines and comparison of isotherm contours between nanofluids(—) and pure fluid(- - -) with different values of (a) d_{avg} =5 nm, Gr = 10^3; (b) d_{avg} = 250 nm, Gr = 10^3; (c) d_{avg} = 5 nm, Gr = 10^6; (d) d_{avg} = 250 nm, Gr = 10^6 for Pr = 6, R = 0.001, and ϕ = 0.05.

an increase in the mean nanoparticle diameter. The effective thermal conductivity increases 23.8% as the mean nanoparticle diameter is reduced from 250 to 5 nm. Consequently, decreasing the diameters of nanoparticles has qualitatively the same effect increasing uniformity of particle size (R).

Figure 2.9 shows the average Nusselt number computed with different mean nanoparticle diameters for various Grashof numbers. It is evident that the average Nusselt number varies significantly with the mean nanoparticle
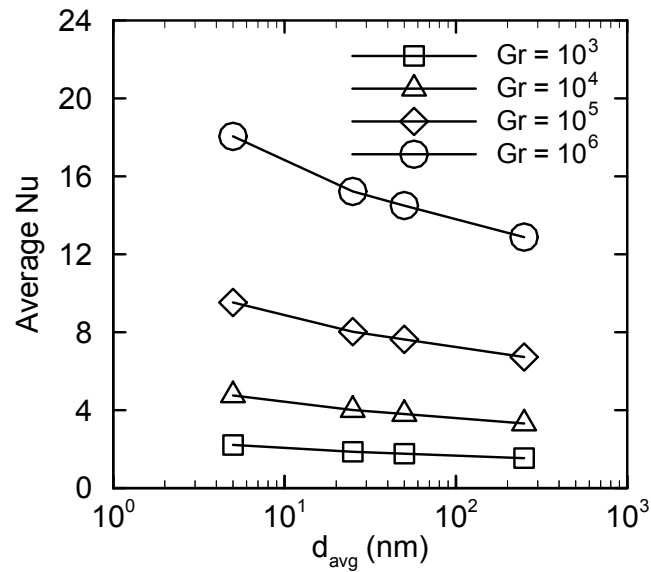
Figure 2.9. Variation of average *Nu* numbers with the mean nanoparticle diameters for constant values of *Gr* numbers with *Pr* = 6, *R* = 0.001, and ϕ = 0.05.

diameter between 5 and 50 nm. By decreasing the mean diameters of nanoparticles from 250 to 5 nm, the heat transfer with different Grashof numbers increases 44.3% and 40.2% for Gr = 10^3 and Gr = 10^6, respectively.

2.5.3. Effect of nanofluid temperature

In the previous section, we determine that the physical properties of nanoparticles have a significant effect on the heat transfer of natural convection, as the diameter of nanoparticles is decreased. There is interplay of between momentum equations and effective thermal conductivity as the nanofluid temperature is increased. For natural convection, it is known that the Nusselt number is proportional to the Prandtl number for pure fluids. However, Eq. (11) reveals that the effective thermal conductivity is inversely proportional to the Prandtl number and hence, the heat transfer characteristics of nanofluids as function of temperature are not immediately clear.

(a) d_{max} = 1.808 μm, d_{min} =1.808 nm, k_{nf}/k_f =1.773

(b) d_{max} = 0.203 μm, d_{min} =1.419 nm, k_{nf}/k_f =2.359

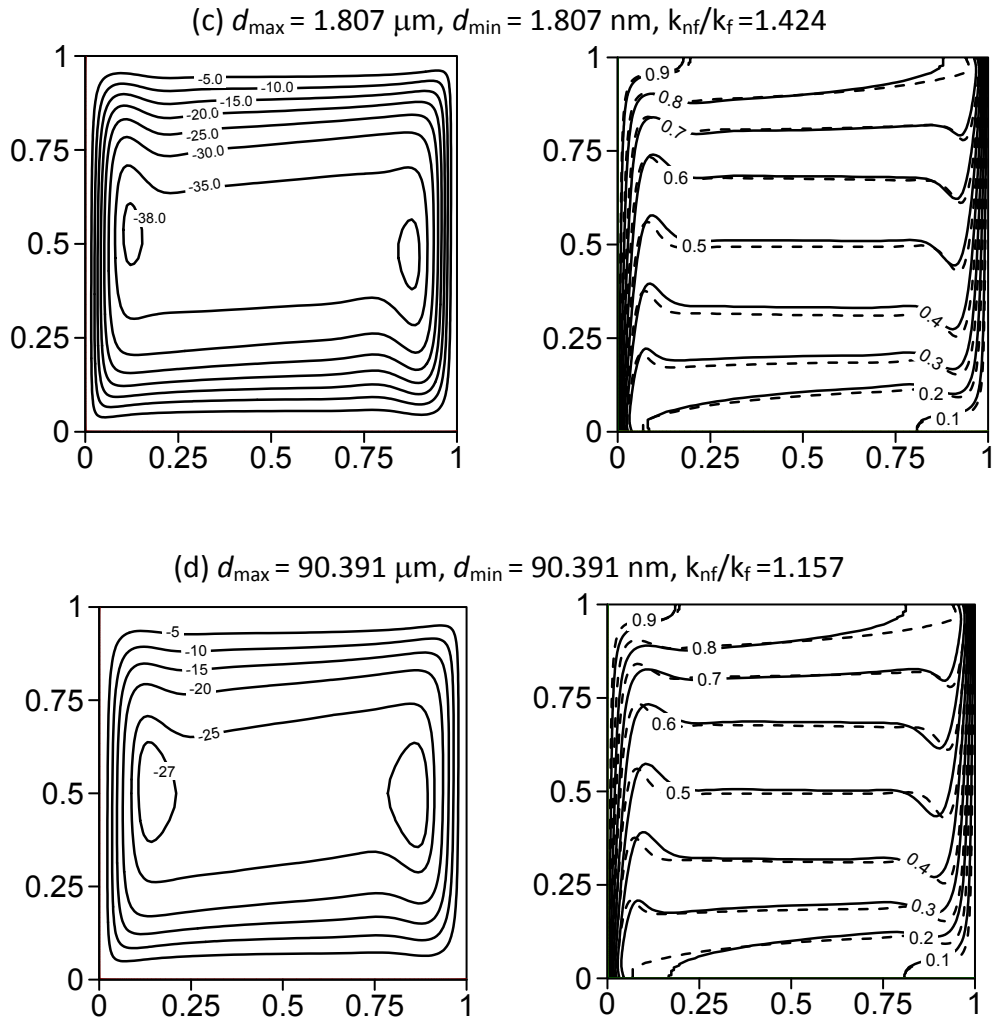(c) d_{max} = 90.391 μm, d_{min} = 90.391 nm, k_{nf}/k_f =1.169
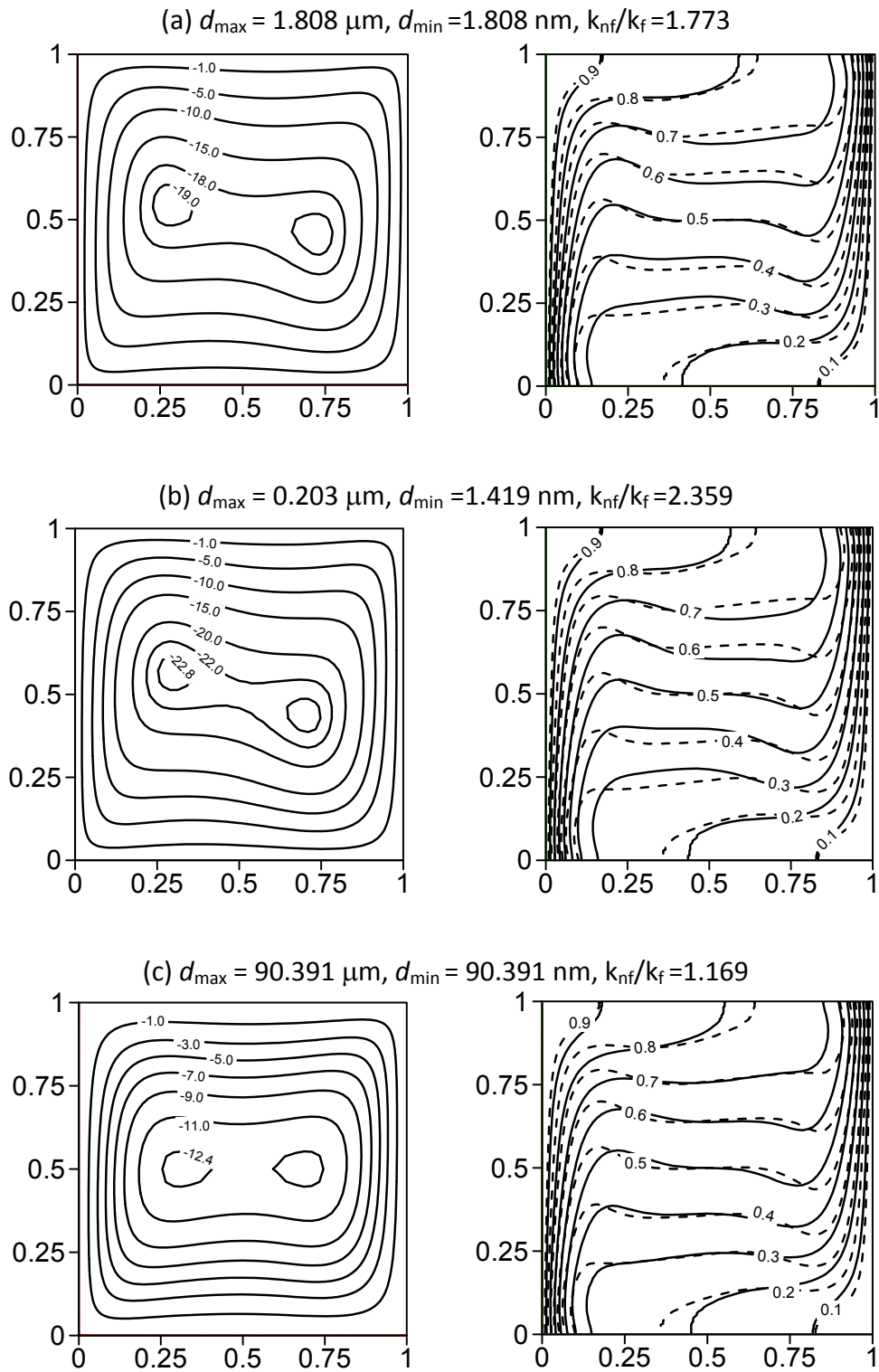
Figure 2.10. Streamlines and comparison of isotherm contours between nanofluids (—) and pure fluid (- - -) with different values of (a) R = 0.001, d_{avg} = 5 nm; (b) R = 0.007, d_{avg} = 5 nm; (c) R =0.001, d_{avg} = 250 nm for Gr = 10^5 and ϕ = 0.05.
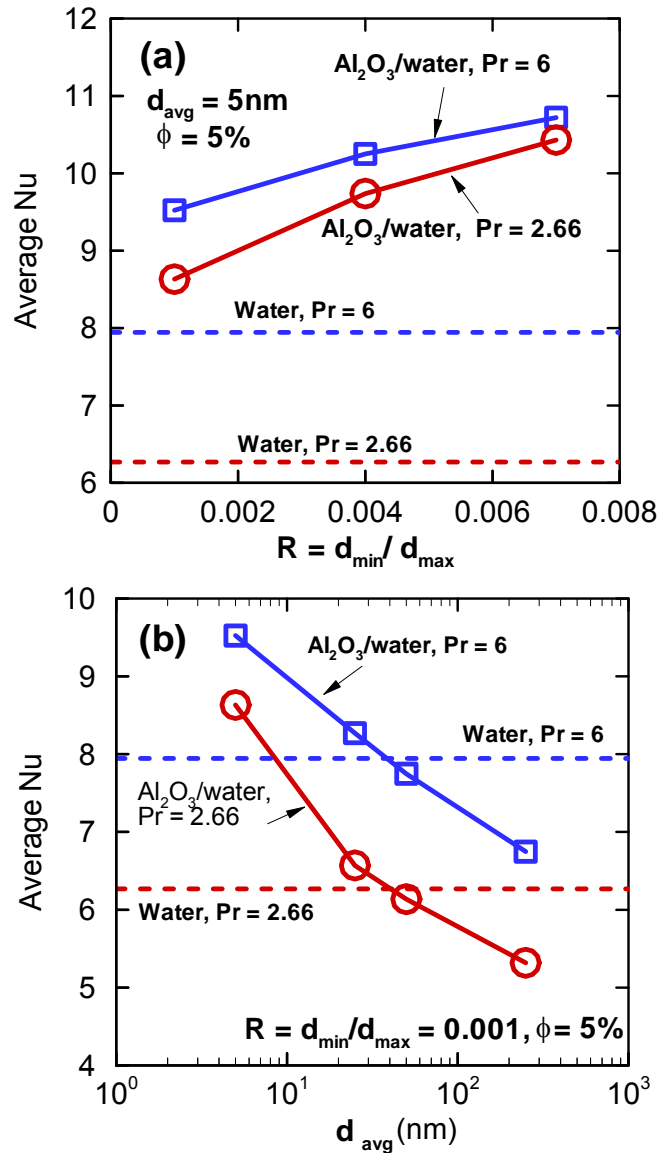
Figure 2.11. (a) Variation of average Nu numbers with the ratio $R = d_{min}/d_{max}$ at $Gr = 10^5$ for different values of Pr numbers. (b) Variation of average Nu number with the mean nanoparticle diameters at $Gr = 10^5$ for different values of Pr numbers. The Prandtl (Pr) numbers of 2.66 and 6 correspond to the temperature of 340 and 300 K, respectively.

In this section, the effect of temperature on the heat transfer is studied considering $Gr = 10^5$ and varying R and d_{avg} at $Pr = 2.66$ and $\phi = 0.05$. The effects of R on the predicted streamlines and isotherms are displayed in Figure 2.10 (a) and (b) for $Pr = 2.66$ and $d_{avg} = 5$ nm. As R changes from 0.001 to 0.007, the flow patterns with two prime vortices are similar and the isotherm

contours illustrate the significant variations due to the relatively low Prandtl number. Compared with the results reported in Figure 2.5 (c) and (d), the effect of R is more important at relatively high temperature. Similarly, Figure2.10 (a) and (c) demonstrate that the effect of mean nanoparticle diameter significantly influences streamlines and isotherms.

Figure 2.11 (a) shows the average Nusselt number as a function of R for transfer enhancement at Pr = 2.66 is approximately 40% more effective than that at Pr = 6. Similarly, Figure 2.11 (b) presents the average Nusselt number as a function of d_{avg} for different Prandtl numbers. It is evident that heat transfer enhancement at Pr = 2.66 is 50% stronger than that at Pr = 6.

2.5.4. Effect of nanoparticle volume fraction

In this section we analyze the effect of the nanoparticle volume fraction ϕ (from 0 to 0.05) on the heat transfer characteristics. Figure 2.12 (a) and (b) report the effect of the particle size uniformity (R) and particle mean diameter (d_{avg}), respectively on the average Nu number. For both cases, the Grashof numbers are varied from 10^3 to 10^6, while the Prandtl number is fixed at Pr = 6.

In Figure 2.12 (a) the effect of R versus the average Nusselt number is plotted for d_{avg} = 5 nm. The results indicate that as R changes from 0.001 to 0.007, the average Nusselt number rapidly increases for different Grashof numbers. Similarly, Figure 2.12 (b) presents the average Nusselt number versus ϕ with various mean nanoparticle diameters. As d_{avg} is increased to 50 nm, the average Nusselt number of nanofluids becomes lower than that of pure fluids for different Grashof numbers. This mitigation of heat transfer is mainly attributed to the effective dynamic viscosity, which is predominant in the

natural convection of the nanofluid for low effective thermal conductivity. Overall, the analysis also defines the operating range where Al_2O_3/water nanofluid can be considered effectively in determining the level of heat transfer augmentation.
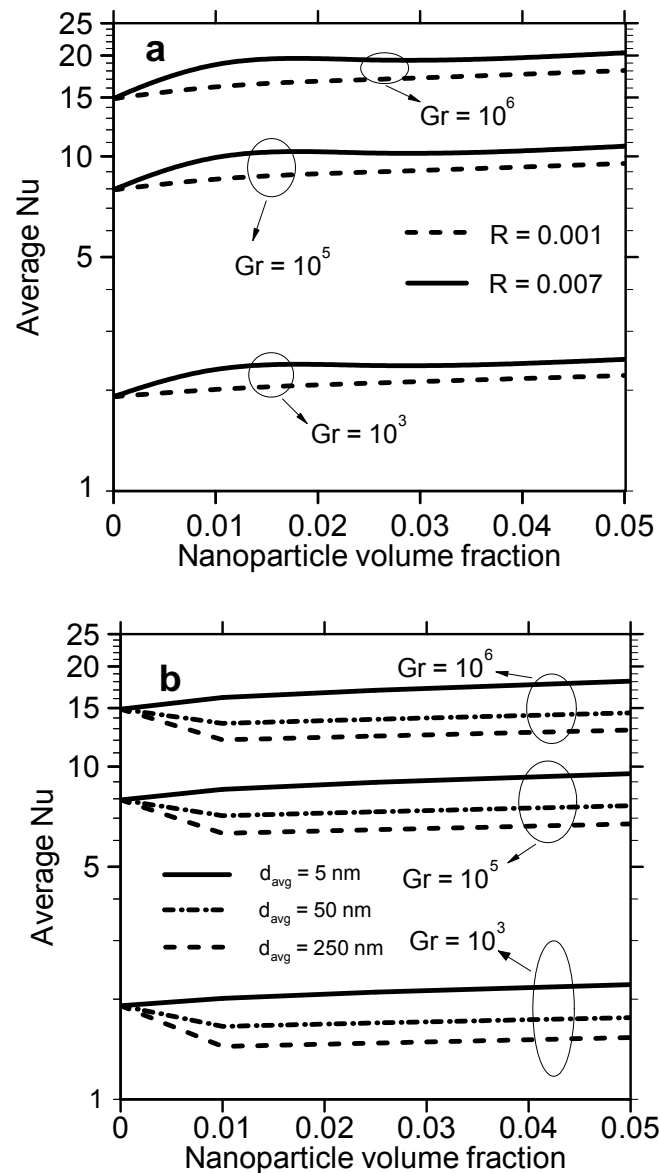
Figure 2.12. Variation of average *Nu* number with ϕ for (a) different values of *R* and *Gr* numbers at *Pr* = 6 and d_{avg} = 5 nm; (b) different values of d_{avg} and *Gr* numbers at *Pr* = 6 and *R* = 0.001.

2.5.5. Comparison with experimental results

In this section the numerical results for the average Nusselt number are compared with the most recent experimental investigations reported in the literature[59] (see Figure 2.13). The Rayleigh numbers are varied from 4.28×10^3
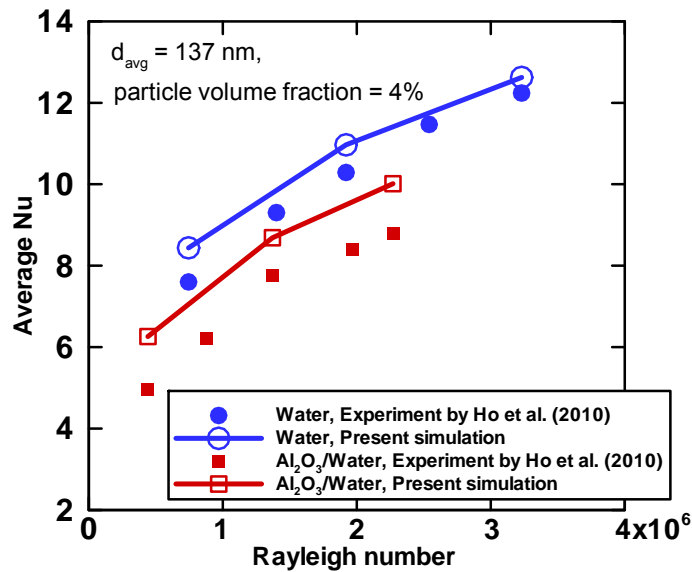
Figure 2.13. Comparison of the numerical simulation results with the experimental data of Ho et al.[59].

to 3.22×10^6, while the Pr, d_{avg} and R are fixed at 6, 137 nm and 0.001, respectively. It is seen that the present model predicts the trend of variation of the experimental data reasonably well. The agreement further confirms the role of the effective dynamic viscosity and thermal conductivity in relation to heat transfer enhancement and suppression.

2.6. Conclusions

The current investigation is concerned with heat and fluid flow of natural convection in a cavity filled with Al_2O_3/water nanofluid that operates under

differentially heated walls. The results of this work illustrate that the heat transfer characteristics of the nanofluid inside the cavity can be enhanced as the ratio of minimum to maximum nanoparticle diameter is increased from 0.001 to 0.007 or the mean nanoparticle diameter is decreased from 250 to 5 nm. These phenomena can be attributed to the dominant effect of the Brownian motion caused by heat convection. However, the heat transfer performance of the nanofluid compared with the pure fluids becomes less significant as the dimensionless total thermal conductivity of the nanofluid is close to unity due to the increase of the nanoparticle sizes. This contradictory effect of nanofluids is mainly caused by effective dynamic viscosity.

The increase of nanofluid temperature is found to augment both the effects of the non-uniform nanoparticle diameter and mean nanoparticle diameter inside the cavity. For small and large Grashof numbers, the cases behave closely in the heat transfer enhancement of nanofluids because the heat conduction is dominated by high thermal conductivity of nanofluids.

The results for the effect of nanoparticle volume faction establish the range of operating nanoparticle parameters where transport activities can be manipulated. Future work is recommended to extend to the current investigation to a model with concentration distributions of nanoparticles. This model shall aid in examining the contribution of the effect of particle migration in augmenting the heat transfer in the present configuration.

CHAPTER 3

A LATTICE BOLTZMANN STUDY OF AEROSOL PARTICLE TRANSPORT AND DEPOSITION

3.1. Introduction

The transport of aerosol particles in laminar and turbulent flows is encountered in a wide range of natural as well as industrial processes or operations such as atmospheric dispersal of pollutants, deposition of contaminants and drug on respiratory surfaces, trapping of soot in gas exhaust pipes, sampling radioactive aerosols, and micro-contamination control in semiconductor fabrication, etc. The phenomena of interest in these areas include particle deposition rates on objects, particle dispersion and preferential accumulation of particles, etc.

Currently, there are two approaches for Particle Phase modeling, namely Lagrangian (particle trajectory) methods and the Eulerian (two-fluid) methods. In the Lagrangian approach, trajectories and velocities of each particle are calculated by integrating the particle momentum equation. In the Euler approach, the transport equation of particle phase is solved to obtain particle concentration distributions. The advantage of the Lagrangian approach over Eulerian models in studies of aerosol particles is the fact that each particle can be handled independently, and, hence, the forces working on each particle can be written down directly.

To obtain reliable solutions using Lagrangian particle-tracking models, however, a large number of particles are generally required on fine grid meshes in numerical simulations[60-62], which has detrimental implications for CPU run times. Therefore, an accurate numerical scheme allowing highly efficient parallel implementation is essential for the Lagrangian particle-tracking approach. Recently, the lattice Boltzmann method (LBM) has emerged as an efficient alternative for simulating and modeling complicated physical and chemical systems[63-64]. Compared with conventional methods used in computational fluid dynamics, the LBM is more efficient for the current trend of massive computations and easier to solve complex flows, such as porous media flows, multi-phase flows, magnetic flows, particulate suspensions, flows over rough boundaries and so on. In addition, the LBM has been recently extended to model turbulent flows[65]. In terms of numerical reliability, several comparative studies have demonstrated excellent performance of the LBM in numerical accuracy compared to conventional schemes[66-69].

Many LB studies of obstructed flows have been proposed over the past few years and various models can be grouped in two main categories. The first one includes problems of flows over a single bluff body and has been simulated in several studies[70-73]. The second group of problems relates to flows around multiple bluff bodies. Surmas et al.[74] presented a fluid flow model around two identical cylinders aligned in tandem and side-by-side arrangements. They analyzed the significance of bluff body wake interference at Reynolds number of 200. Agrawal et al.[75] simulated a flow around two square prisms placed side-by-side at Reynolds number of 73 and investigated the effect of the gap ratio between two obstacles on the fluid-flow structures.

Recently, the review of two cylinders in cross flows by Sumner[76] raised concern regarding complexity of flow fields around multiple-cylinder configurations. The author concluded that the staggered configuration, although most commonly found in engineering applications, has received less research attention. Niu and Zhu[77] reported a three-dimensional numerical study of flows around two identical square prisms in staggered arrangements. Sarkar et al.[78] studied the mixed convection behind two square prisms in staggered arrangements at Reynolds number of 100 and found the maximum heat transfer at the second obstacle for a particular obstacle spacing. Most recently, Berbish[79] performed an experimental and numerical analysis for heat transfer and flow features around four elliptic prisms in staggered arrangements. The author demonstrated that the heat transfer characteristics of the obstacles were correlated in terms of Reynolds numbers and obstacle spacing ratios.

Several experimental studies have examined dispersion behaviors of aerosol particles in shear flows[80-84] and deposition of aerosol particles on a single object[85-87]. It has been identified that the effect of inertial impaction on the motion of particles in a fluid flow is characterized by the Stokes number, defined as the ratio of particle response time to a characteristic flow time. The Stokes number is proportional to the square of a particle diameter so that increasing the particle size leads to increased particle deposition. During the last decades, the development of numerical fluid-flow models coupled to particle phase equations opened new ways to investigate transport of aerosol particles in obstructed fluid flows. In an early study, Li et al.[88] numerically studied deposition of aerosol particles in a turbulent duct flow over a single

obstacle mounted on the bottom wall. The authors evaluated the capture efficiency of rectangular and trapezoidal blocks for different Stokes numbers. Different authors[60,62,89] analyzed influences of various vortex structures on the transport of aerosol particles in wakes behind a single obstacle. In these studies, the forces considered in the Lagrangian particle equation were lift, drag and gravity effects. Haugen and Kragset[90] used a direct numerical simulation to study aerosol particle impaction on a cylinder in a cross flow as a function of Stokes and Reynolds numbers. Brandon and Aggarwal[91] and Salmanzadeh et al.[92] modeled deposition and dispersion of aerosol particles on a rectangular prism in a channel flow without Brownian motion and both demonstrated particle deposition efficiencies on the front side of the obstruction as a function of Stokes numbers. More recently, Jafari et al.[93] were the first to use the LB method, together with the Lagrangian particle equation of motion, to simulate a particle-laden flow over a square prism at Reynolds number of 200. The authors showed that Brownian motion affects the deposition efficiency of submicron particles on the block and motion of particles behind the obstacle is significantly influenced by the vortex shedding. A numerical model of aerosol particle transport in a channel flow over two square prisms in tandem has been recently developed to determine the effect of the gap between two blocks on obstruction capture efficiencies[94]. The forces considered in the Lagrangian model were drag, gravity and buoyancy effects.

Although particle-laden flows in obstructed channels have been extensively studied in the past, relatively little is known about the effects of obstruction arrangements on the transport of aerosol particles with Brownian motion. In the present study, we have further examined the effects of multiple

obstacles and block-to-block spacings on particle dispersion and disposition by simulating particle-laden flows around square prisms placed in a rectangular channel. An incompressible Lattice Boltzmann model coupled with Lagrangian tracking of many thousand discrete particles is used to produce a systematic description of the phenomenon. Therefore, the findings of this study provide more information on the fluid-particle characteristics in two phase coherent vortex structures and extend the applicability of the LBE method in particle Lagrangian simulations.

3.2. Mathematical model

Figure 3.1 shows the schematic of the model adopted in this study with boundary conditions and coordinates. The origin of the Cartesian coordinate system is at the left corner of the bottom wall located at $y = 0$. The bluff bodies, with each side of length B, are placed in a rectangular channel. The channel width (H) and the length are taken as $4B$ and $30B$, respectively. T is the transverse spacing and L is the longitudinal spacing between the centers of two consecutive obstacles. The upstream distance of the first obstacle is $10B$.
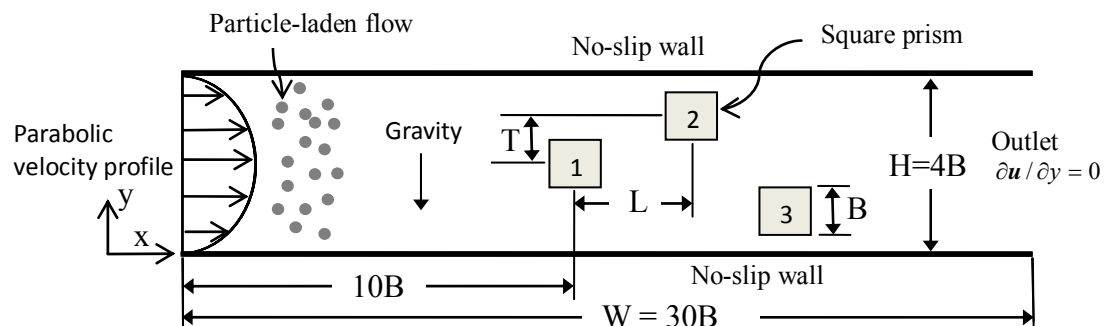
Figure 3.1. Schematic for the physical model with boundary conditions of the problem.

The staggered configuration is employed for the arrangement of the multiple blocks placed in the channel (Figure 3.1). Initially, the gas, without particles, is at rest anywhere in the channel. The fluid motion is then generated by a parabolic velocity profile with a maximum velocity (u_{max}) at inflow. After the flow reaches a steady state or time-periodic state (Kármán vortex street), particles of given size and density are injected with a random distribution at the inlet of the channel. For the velocity field, no-slip/zero-penetration conditions are imposed on the walls of the channel, and standard pressure outlet conditions are used at the channel exit.

3.2.1. Assumptions

The mathematical equations describing the physical model are based on the following assumptions: (I) particles are spherical and of uniform size and density; (II) the third dimension of this 2D channel is equal to the particle diameter; (III) particle-laden flows are considered dilute enough (particle volume fractions less than 10^{-6}) so that the effect of particles on the fluid flow is negligible; (IV) particle-particle interactions are neglected; (V) particles are removed from the flow field once they impact obstacles or channel walls.

3.2.2. Gas-phase equations

The incompressible lattice Boltzmann model proposed by He and Luo[95] is used to solve the incompressible Navier–Stokes equations for the fluid velocity. All quantities given in physical units of time (s) and length (m) are non-dimensionalized as follows:

$$x = \frac{x^*}{B}, \quad t = \frac{t^*}{B / c_0}, \quad u = \frac{u^*}{c_0}, \quad v = \frac{v^*}{c_0}, \quad P = \frac{p^*}{c_0^2 \rho_g}, \quad \upsilon_g = \frac{\upsilon_g^*}{Bc_0}, \tag{1}$$

Variables x, t, u, v and P are spatial coordinate, time, velocity components in x- and y- direction and pressure, respectively. The parameter υ_g is the kinematic viscosity.

The evolution equation for the flow field using the pressure distribution function is expressed as:

$$p_\alpha(x + c \cdot e_\alpha \cdot \Delta t, t + \Delta t) = p_\alpha(x,t) - \tau_f^{-1} \cdot \left[p_\alpha(x,t) - p_\alpha^{eq}(x,t) \right] \tag{2}$$

$$p_\alpha^{eq} = w_\alpha \left\{ P + P_0 \left[3 \frac{(e_\alpha \cdot u)}{c} + \frac{9}{2} \frac{(e_\alpha \cdot u)^2}{c^2} - \frac{3}{2} \frac{u^2}{c^2} \right] \right\} \tag{3}$$

where $c = \Delta x / \Delta t$ is the streaming speed and $P_0 = \rho_0 / c_s^2$ is the pressure at room temperature. Δx, Δt, ρ_0, c_s and τ_f are the lattice grid spacing, time step, density at room temperature, sound speed and dimensionless relaxation time, respectively. p_α^{eq} is the corresponding equilibrium distribution function. For the 9-bit lattice Bhatnagar-Gross-Krook (LBGK) model in two-dimensional square lattice space, the sound speed c_s is $c / \sqrt{3}$ and e_α is given by

$$e_\alpha = \begin{cases} (0,0), \alpha = 1 \\ (\cos[(\alpha - 1)\pi / 2], \sin[(\alpha - 1)\pi / 2]), \alpha = 2,3,4,5 \\ (\cos[(\alpha - 5)\pi / 2 + \pi / 4], \sin[(\alpha - 5)\pi / 2 + \pi / 4]), \alpha = 6,7,8,9 \end{cases} \tag{4}$$

where the weights $w_1 = 4/9, w_{2,3,4,5} = 1/9$ and $w_{6,7,8,9} = 1/36$. The macro-scopic variables for the fluid pressure and velocity are calculated by $P = \sum_{\alpha=1}^{9} p_\alpha$, $P_0 u = \sum_{\alpha=1}^{9} p_\alpha e_\alpha$, respectively. Through multiscaling expansion, the incompressible Navier–Stokes equations can be derived from this LBGK model with a kinematic viscosity:

$$v_g = \frac{2\tau_f - 1}{6} c^2 \Delta t \qquad (5)$$

The flow Reynolds number is defined as $Re = u_{max} B / v_g$.

For the present simulations, a parabolic velocity profile is prescribed at the channel entrance. At the channel exit, $\partial u / \partial x = 0$ is used as the outlet boundary condition. On the upper and lower walls, as well as on the obstacle
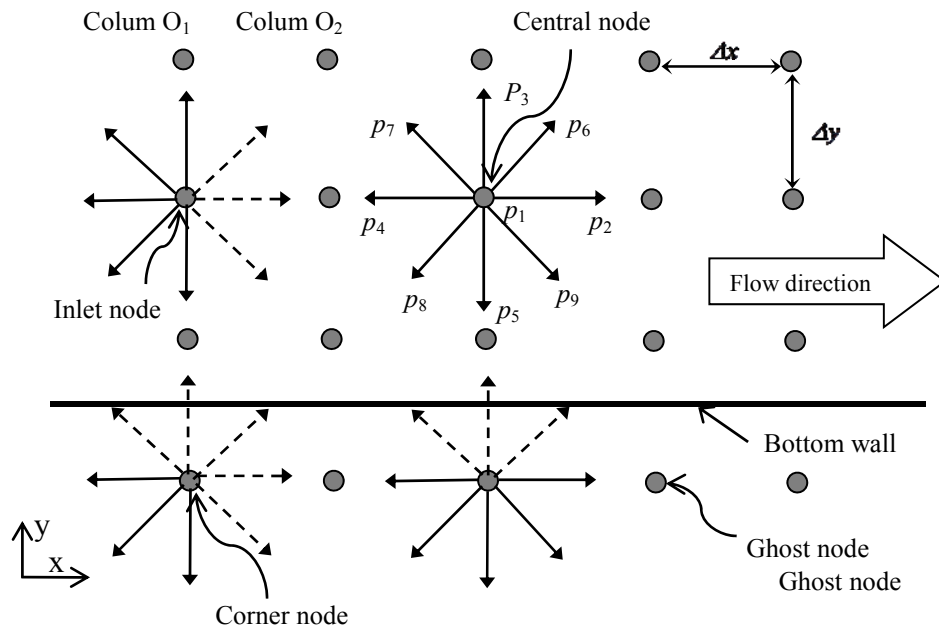
Figure 3.2. Boundary conditions of the inlet and bottom wall for the distribution function. Solid lines are known conditions and dashed lines are unknown ones.

boundaries, no-slip boundary conditions are applied, respectively. To implement these boundary conditions in the LBM, the unknown distribution functions at boundary nodes have to be determined, see Figure 3.2. At the nodes of the inlet boundary, the unknown distribution functions p_2, p_6 and p_9 are derived from the following equation[96]:

$$p_{2,6,9}(O_1,t) = p_{2,6,9}{}^{eq}(u(O_1),t) + (1 - \tau_f^{-1}) \cdot [p_{2,6,9}(O_2,t) - p_{2,6,9}{}^{eq}(O_2,t)] \qquad (6)$$

At the inlet bottom node, the unknown distribution functions are expressed as[97]:

$$p_2 = p_4, \quad p_3 = p_5, \, p_6 = p_8, \, p_9 = p_7,$$

$$p_7 = 0.5(P - p_1) - (p_4 - p_5 - p_8) \tag{7}$$

Using the halfway bounce-back scheme[97], the outgoing distribution functions at a wall or obstacle node $p_{\tilde{\alpha}}^{out}$ are given by $p_{\tilde{\alpha}}^{out} = p_{\alpha}^{in}$, where p_{α}^{in} is the incoming distribution functions and $\tilde{\alpha}$ and α denote directions opposite to each other. The outlet nodes and other corner nodes can also be handled in the procedure described above. A second-order finite difference scheme is used to get the velocity at the outlet boundary:

$$\left.\frac{\partial \boldsymbol{u}}{\partial x}\right|_{i,I} = \frac{4\boldsymbol{u}_{i,2} - \boldsymbol{u}_{i,3} - 3\boldsymbol{u}_{i,1}}{2\Delta x} \tag{8}$$

The vorticity Ω is determined from the calculated velocity field for one flow simulation via the vorticity equation:

$$\Omega = \frac{\partial v}{\partial x} - \frac{\partial u}{\partial y} \tag{9}$$

3.2.3. Particle equation of motion

In this study, a detailed particle dynamics model based on a Lagrangian formalism[93] is adopted to describe their trajectories. The governing equations for the instantaneous particle location (x_p^*, y_p^*) and velocity (u_g^*, v_g^*), in dimensional form, are as follows:

$$\frac{\mathrm{d}x_p^*}{\mathrm{d}t} = u_p^* \quad , \quad \frac{\mathrm{d}y_p^*}{\mathrm{d}t} = v_p^* \tag{10}$$

$$\rho_p V_p \frac{d\boldsymbol{u}_p^*}{dt} = -\frac{3\pi\mu_g d_p}{C}\left(\boldsymbol{u}_p^* - \boldsymbol{u}_g^*\right) + \left(\rho_p - \rho_g\right)V_p \boldsymbol{g} + \boldsymbol{F}_L + \boldsymbol{F}_B \tag{11}$$

where V_p is the volume of a single particle, ρ_p is the particle density, d_p is the particle diameter, μ_g is the gas dynamic viscosity. The first term on the right-hand side of Eq. (11) is the drag force due to the relative velocity of the particle with respect to the carrier fluid. The Cunningham correction factor C is defined by[98-99]:

$$C = 1 + \frac{2\lambda_g}{d_p}\left[1.252 + 0.399\exp\left(-1.1\frac{d_p}{2\lambda_g}\right)\right] \tag{12}$$

where

$$\lambda_g = \upsilon_g\left(\frac{\pi \mathrm{M}_g}{2RT_g}\right)^{0.5} \tag{13}$$

is the mean free path of air molecules and R, M_g and T_g are universal gas constant, molecular mass of air and gas temperature, respectively. The second term on the right-hand side of Eq. (11) is the gravitational force and the third term is the Saffman lift force due to the gradient in the shear flow as defined by[100-101]:

$$F_{L,x} = 1.615\rho_g\upsilon_g^{0.5}d_p^2\left(u_g^* - u_p^*\right)\sqrt{\frac{dv_g^*}{dx}}\,\mathrm{sign}\left(\frac{dv_g^*}{dx}\right)$$

$$F_{L,y} = 1.615\rho_g\upsilon_g^{0.5}d_p^2\left(v_g^* - v_p^*\right)\sqrt{\frac{du_g^*}{dy}}\,\mathrm{sign}\left(\frac{du_g^*}{dy}\right) \tag{14}$$

where the local fluid velocities (u_g^*, v_g^*) are calculated by interpolation among the velocity data provided by the LB fluid model. The last term on the right-hand side of Eq. (11) is the Brownian force based on frequent collisions between the ultrafine particles and the gas molecules. The Brownian motion is modeled as a Gaussian white noise stochastic process suggested by Li and

Ahmadi[102,104] and Zare et al.[103]:

$$F_B = G_i \left(\frac{6\pi \mu_g d_p \kappa T_g}{C \Delta t} \right)^{0.5} \tag{15}$$

where $\kappa = 1.38 \times 10^{-23} \, \text{J/K}$ is the Boltzmann constant and $G_i \, (i = 1, 2)$ are pairs of independent Gaussian random numbers with zero means and unit variance. These Gaussian random numbers are generated at each time step and given by:

$$G_1 = \sqrt{-2\ln(U_1)} \cos(2\pi U_2)$$

$$G_2 = \sqrt{-2\ln(U_1)} \sin(2\pi U_2) \tag{16}$$

In Eq. (13), U_1 and U_2 are uniform random numbers between 0 and 1. The ordinary differential equations represented by Eq. (10) and (11) are integrated analytically over each time step[105]. To measure the interplay between the travel of the particle and fluid flow within an obstacle, the Stokes number (Stk), defined as the ratio of particle response time (t_p) to a characteristic flow time (t_g), is used[91]:

$$Stk = \frac{t_p}{t_g} = \frac{d_p^2 \varepsilon \, Re}{18 B^2} \tag{17}$$

where ε is the ratio of particle density to gas density. Finally, the particle deposition efficiency, as defined by:

$$\eta = \frac{\text{Number of deposited particles on the solid surface}}{\text{Number of particles injected into the flow}} \tag{18}$$

is expected to depend on physical properties of particles and carrier fluids, types of flow field structure and obstacle geometry.

3.3. Algorithm validation

The validity of the LB model has been assessed by grid-independence and by comparisons with the results in the literature on flows around a square prism. The Reynolds numbers considered are such that the flow is characterized by unsteady two-dimensional shedding of vortices in the wake of the block. In these simulations, the frequency of vortex shedding is reported in dimensionless form as the Strouhal number, defined as $Str = f \cdot B / u_{max}$, where f is the frequency of oscillation, obtained by fast-Fourier-transform (FFT) of the velocity history at downstream of the block. Different uniform grids of 121x901, 161x1201, 242x1801 are examined for the blockage ratio (B / H) of 0.25 and Reynolds number of 150. The Strouhal numbers are 0.1895, 0.1904 and 0.1904 for the grid points of 121x901, 161x1201, and 242x1801, respectively. It is observed that the further refinement from the grid of 161x1201 does not result in improvement.

In the present study, however, the finest grid level is chosen to capture the dynamic characteristics of particle motion over the range of operational parameter values considered. Figure 3.3 shows the comparison between the results obtained with the grid of 242x1801 points and the values available in the literature[69,93,106]. The comparisons for the Strouhal number dependence on Reynolds number and their corresponding blockage ratios indicate a reasonable agreement. Although the predicted Strouhal numbers at the blockage ratio of 0.25 are slightly higher than the previous reference values, the present model shows less discrepancy between LBM and FEM (Finite Element Method) than that obtained by the LBM of Jafari et al.[93].

To ensure the accuracy and validity of current particle-laden flow models,

21 aerosol particles entering the projected area of the obstacle surface at the
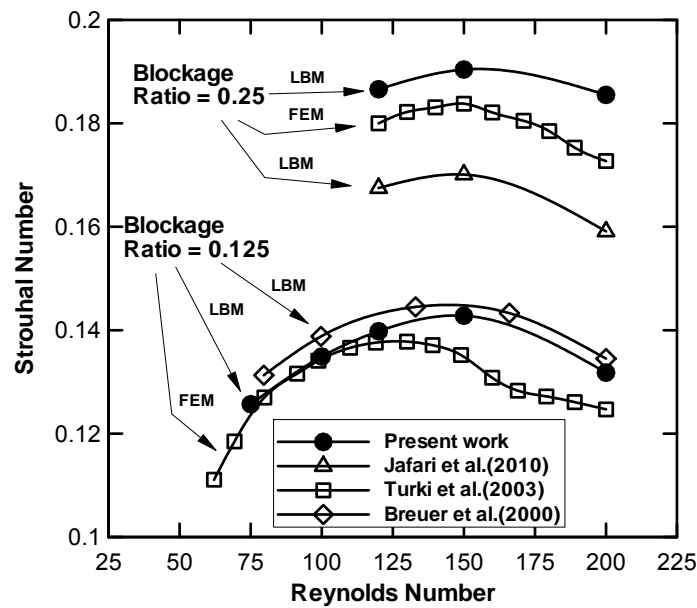

Figure 3.3. Variation of Strouhal number with Reynolds number for laminar channel flow over a square prism. Comparison of Finite Element method (FEM) and Lattice Boltzmann method (LBM) results.
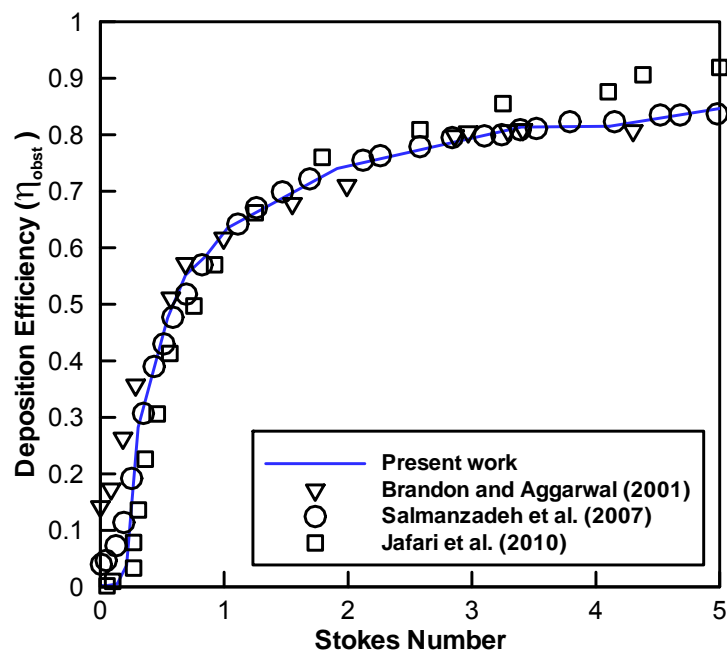

Figure 3.4. Comparison of particle deposition efficiency versus Stokes number from present results and previously published data for aerosol transport over a square prism at $B/H = 0.25$.
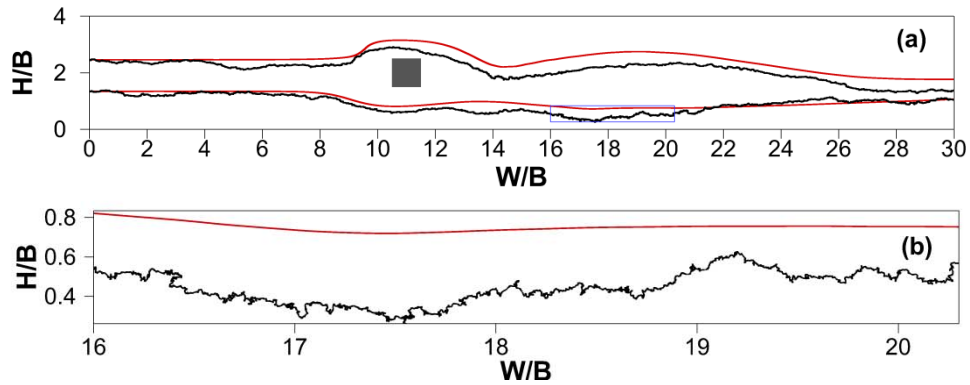
Figure 3.5. Comparison of particle trajectories in a channel flow with a square prism for d_p = 1 nm. (a) The entire computational domain; (b) A zoom-in view for one particle trajectory shown in the open rectangular of Fig. (a). Black line, with Brownian motion; Red line, without Brownian motion.

channel inlet are uniformly injected every 50 time step, and the resulting particle deposition efficiencies on the obstacle are compared with those obtained from other authors[91-93] by using different particle phase equations. Figure 3.4 shows the computed deposition efficiencies as a function of Stokes number for a blockage ratio of 0.25. At Stk less than approximately 0.2, where the Brownian force increasingly dominates, the predicted values agree well with those estimated by the model of Jafari et al.[93] which takes into account the effect of Brownian motion. At the region where the inertial impaction is dominant ($Stk > 0.4$), the simulation results are also in good agreement with those predicted by the models[91,92] without Brownian motion. To further illustrate the importance of the Brownian force acting on the particles, trajectories of two nanoparticles with and without the Brownian motion effect are displayed in Figure 3.5 for a blockage ratio of 0.25. It is clear that all particle paths have followed roughly the same patterns of flow streamlines, but the particles with Brownian excitations are tending to dissociate along the direction of gas flow rather like the particles without Brownian excitations.

3.4. Results and discussion

As stated in the previous sections, the overall objective of this current investigation is to explore the deposition and transport behavior of aerosol particles in miniature channel flows as a function of block arrangements and Stokes numbers. Specifically, we will analyze particle distributions and deposition efficiencies for various values of block numbers, longitudinal and transverse spacings between two blocks, and Stokes numbers. Numerical simulations have been done for spherical monodisperse aerosol particles with diameters of 15 μm, 10 μm, 500 nm, 10 nm and 1 nm, respectively, and the particle-fluid density ratio of 1.7. The particle parameters used are essentially the same as those in references[103,107] with a slight modification. In all of the following, we have set the blockage ratio to 0.25 and fluid Reynolds number to 100. These two constants yield five Stokes numbers (1.05×10^{-5}, 1.68×10^{-4}, 4.21×10^{-3}, 1.05×10^{-1} and 2.37×10^{-1}) from Eq. (17) with the given particle diameters and ε. Initially, the computations are started without particles until a time-periodic flow is achieved. The procedure to generate the particle-laden flow is the same as Section 3 except that the particles are randomly inserted at the upstream section of channel with zero initial velocity. To ensure the independence of numerical solutions from the particle number, there are totally 42,000 particles introduced into the channel at the end of each simulation. The temporal step size used in the computation is less than the particle relaxation time to avoid any influence on the flow and particle field. The results are found to be repeatable except for some slight variations caused by the initial random particle distributions or random Brownian forces.

3.4.1. Effect of staggered blocks

To study the effect of staggered blocks on the aerosol particle deposition and dispersion, we vary the number of blocks (*N*) in a cross flow of gas from 1 to 3, while the particle size is specified in the range from 1 nm ≤ d_p ≤ 15 μm. The centers of block 1, block 2 and block 3 in staggered arrangement (Figure 3.1) are located at (x, y) = (10, 2), (12, 3) and (14, 1), respectively. Three types of obstructions constructed for channel flow systems are characterized by the presence of (I) block1, 2 and 3, (II) block1 and 2, and (III) block1.
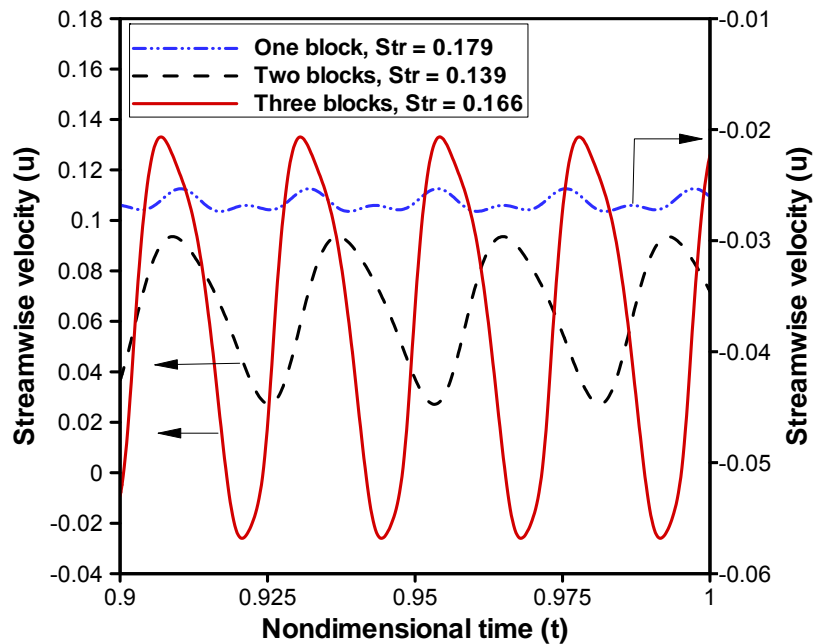
Figure 3.6. Time trace of the streamwise velocity stored downstream at *x* = 1.2 from the rear side of the square prism. For the channels with two and three blocks placed, the location of the steamwise velocity is behind the second and third block, respectively.

Figure 3.6 shows the time-dependent evolution of fluid streamwise velocity in wakes. It is clear that the amplitude of velocity fluctuations increases with the number of blocks. Moreover, the oscillation frequency of the fluid

streamwise velocity is found to be minimum when the number of blocks is set

to *N* = 2, its Strouhal number being approximately 22% and 16% lower than in

the case of *N* = 1 and 3, respectively.
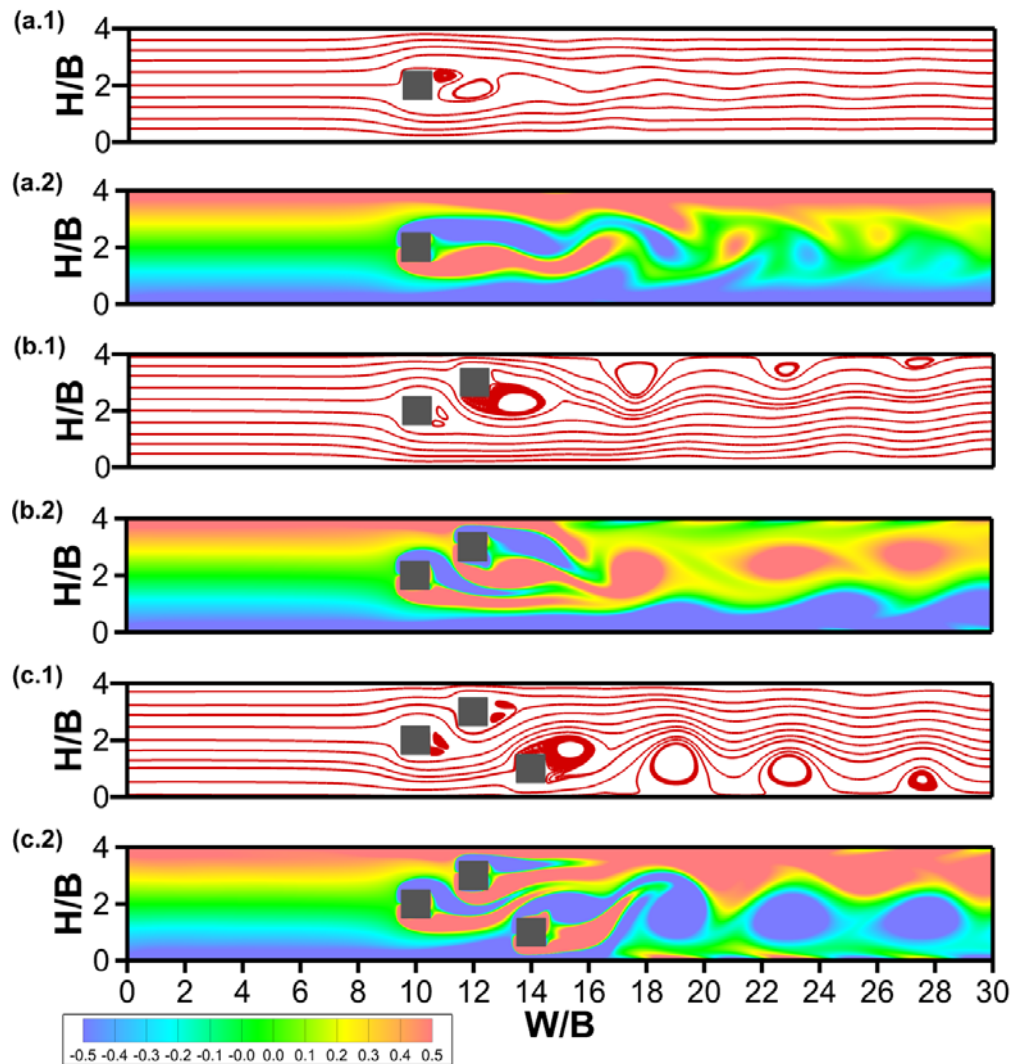
Figure 3.7. Instantaneous streamtraces and vorticity contours of the gas flow in a channel with: (a) one block; (b) two blocks; and (c) three blocks. Images are captured at the time of the maximum streamwise velocity in one vortex shedding cycle.

Figure 3.7 illustrates the effect of staggered blocks on the time-periodic

state variation of the gaseous-phase streamtraces and vorticity contours at the

time of the peak streamwise velocity in one vortex-shedding cycle. In this

physical model, the flow patterns depicted by streamtraces are characterized by the temporal development of the near-wake recirculation zones that form downstream of the blocks. Unlike the flow pattern observed in the case of the single block (Figure 3.7a1), the enlarged recirculation zone attached to the corner of last staggered block (Figure 3.7b1 and c1) increases the strength of the eddy transport and hence creates recirculation zones moving down-stream along the channel wall. Furthermore, different patterns of vortex shedding (Figure 3.7a2, b2 and c2) are observed between the case of a single block and staggered blocks. Figure 3.7a2 shows the alternate shedding of vortices from two sides of the block. This vortex shedding phenomenon, however, is not the results of the staggered blocks as the vortices generated from the leading edge near the channel wall are suppressed (Figure 3.7 b2 and c2). In the case of $N = 3$, vortices generated from block 1 and 2 are suppressed and added up with the vortices generated at block 3. This roll-up process extends the boundary zones between two vortex structures and may increase the effect of stretching and folding on the behavior of particles in the boundary of the vortex structures[60,62].

The effects of staggered blocks on the predicted particle dispersion are displayed in Figure 3.8 and 3.9 for different particle sizes. Each instantaneous image of particle distributions corresponds to flow field of Figure 3.7. For the micron particles, it can be seen from Figure 3.8 that the deposition of particles on the lower wall and the front side of blocks is appreciable and the dispersed particles have characteristics of preferential concentration along the boundary regions of vortex structures. The particles are continuously centrifuged out of a vortex because the micron particle and fluid response time scales are of

similar order ($Stk \sim O(1)$). In the presence of y-direction gravity effect, the dispersion process of d_p = 15 μm exhibits more progressive lateral sedimentation in the upper section of the channel as compared to that of d_p =
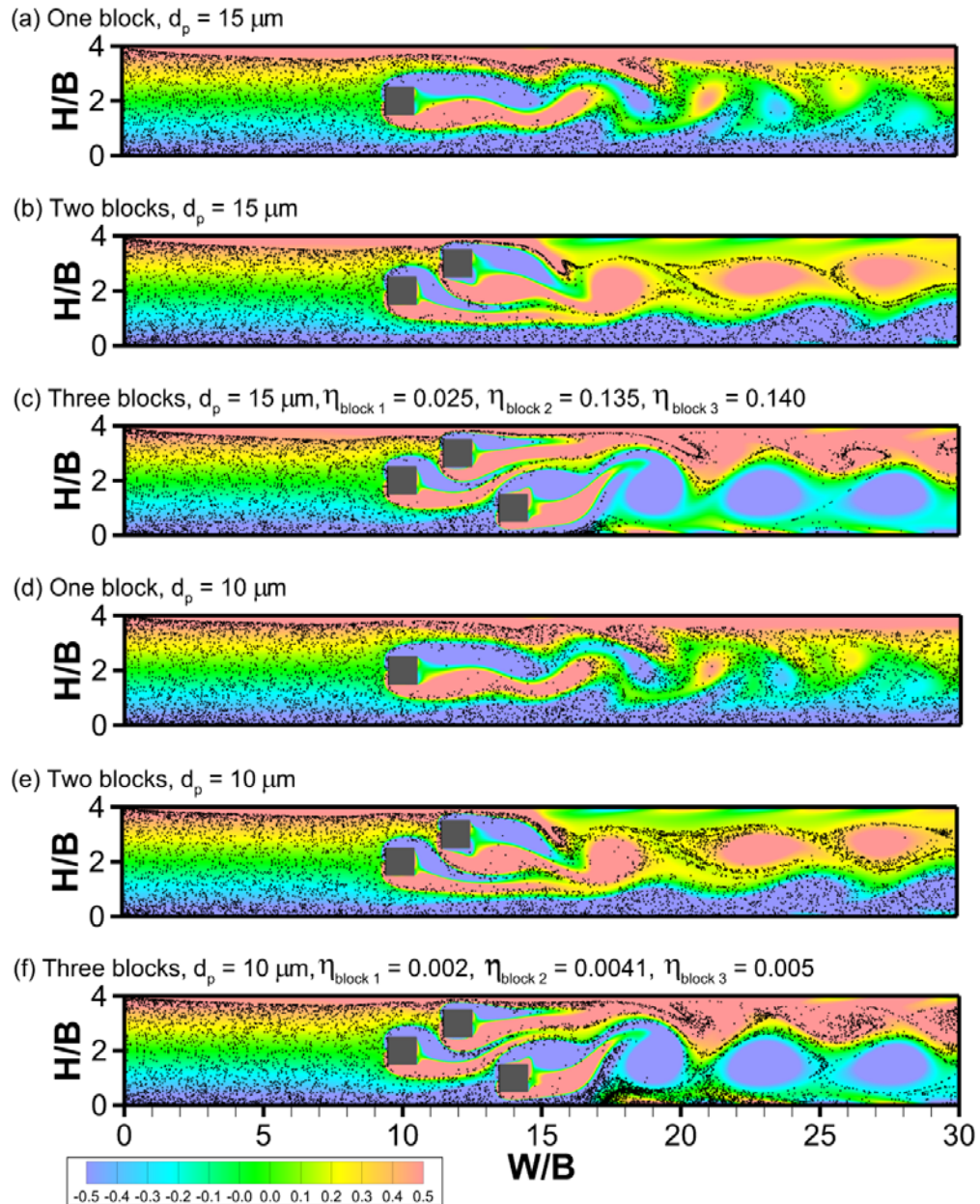
Figure 3.8. Instantaneous particle distribution and vorticity contours of the gas flow in a channel with different values of: (a) d_p = 15 μm, one block; (b) d_p = 15 μm, two blocks; (c) d_p = 15 μm, three blocks; (d) d_p = 10 μm, one block; (e) d_p = 10 μm, two blocks; and (f) d_p = 10 μm, three blocks. Images are captured at the time of the maximum streamwise velocity in one vortex shedding cycle (after 42,000 particles have been injected).
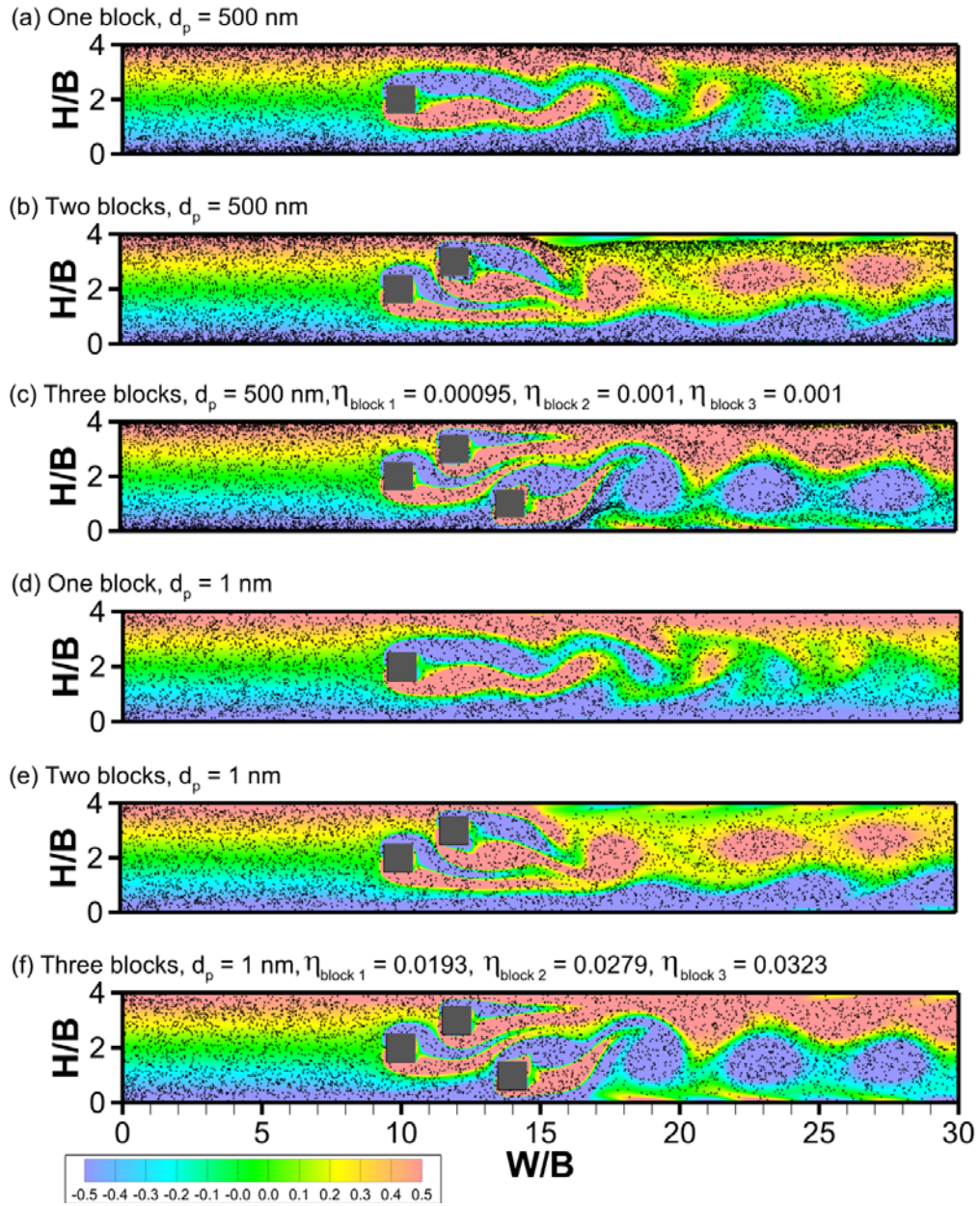
Figure 3.9. Instantaneous particle distribution and vorticity contours of the gas flow in a channel with different values of: (a) d_p = 500 nm, one block; (b) d_p = 500 nm, two blocks; (c) d_p = 500 nm, three blocks; (d) d_p = 1 nm, one block; (e) d_p = 1 nm, two blocks; and (f) d_p = 1 nm, three blocks. Images are captured at the time of the maximum streamwise velocity in one vortex shedding cycle (after 42,000 particles have been injected).

10 μm. For the submicron particles (Figure 3.9), particles are not affected significantly by the gravity force and centrifugal force of vortices. Because of the low Stokes numbers, particles have sufficient time to respond to the impact of gas molecules and behave like fluid tracers. Thus, the conglomeration of the

particles in the boundary regions of vortices is barely visible and particles are uniformly distributed in space. Under these conditions, the deposition of submicron particles occurs not only on the front side of the blocks but also along the sides of the blocks. It is seen that the quantity of dispersed particles in the case of d_p = 1 nm (Figure 3.9d, e and f) is smaller when compared with that of d_p = 500 nm (Figure 3.9a, b and c). This phenomenon is due to the increased Brownian motion in the case of ultrafine particles (d_p = 1 nm).

In the case of d_p = 15 μm (Figure 3.8c), the particle deposition efficiencies on block 2 and 3 are approximately six times greater than that of block 1. This enhanced deposition of particles on the staggered blocks can be explained by the increased velocity of particle-laden flow in the narrowed spaces between the walls and blocks. However, as seen in Figure 3.8f, 3.9c and 3.9f, this geometrical influence becomes smaller when the particle size is reduced from 15 μm to 1 nm (Figure 3.8f). This finding can be interpreted by realizing that inertial impaction of particles on the blocks is not expected to have a significant effect on the deposition of such particles, with a diameters d_p ≤ 10 μm[108-109].

Variations of the predicted particle deposition efficiencies versus particle diameters for different numbers of blocks placed in the channel are shown in Figure 3.10. The particle deposition efficiencies on the obstructions (η_{obst}), walls ($\eta_{upper\,wall}$, $\eta_{lower\,wall}$) are calculated using Eq. (18) and the total deposition efficiency of particles is obtained by $\eta_{total} = \eta_{obst} + \eta_{wall}$. In general, all particle deposition efficiencies (η_{obst}, $\eta_{lower\,wall}$, η_{total}) exhibit a clear minimum at 10^2 nm ≤ d_p ≤ 10^3 nm for different numbers of blocks placed except for $\eta_{upper\,wall}$, which is inversely proportional to the size of the particles (Figure 3.10b). This
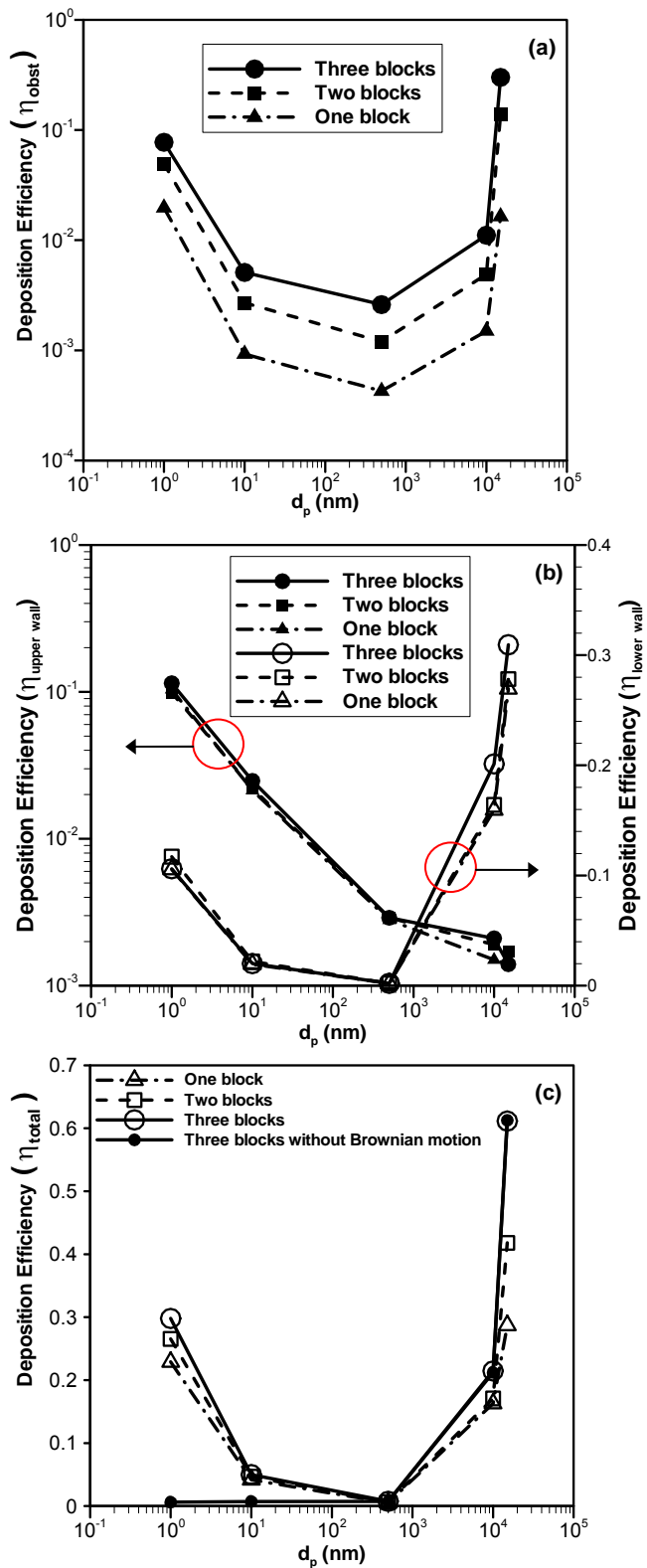
Figure 3.10. Deposition efficiency as a function of particle diameter for different numbers of blocks placed in the channel. Particles deposited on the (a) obstructions, (b) walls and (c) both obstructions and walls.

decrease of $\eta_{\text{upper wall}}$ at $d_p \geq 10^3$ nm is related to the fact that the gravity acceleration along direction (-y) increases sharply when the micron particles are introduced into the channel (Figure 3.8). Figure 3.10(a) shows that increasing the number of blocks in staggered arrangements enhances the deposition of particles on obstructions. However, as seen in Figure 3.10(b), the deposition efficiency of submicron particles on the channel wall is less influenced by the number of blocks than that of micron particles. For the total deposition efficiency of particles (Figure 3.10c), the effect of staggered blocks on particle deposition is significantly increased as the particle diameter is increased in the micron region and reduced in the submicron region. This deposition enhancement, as would have been expected from the results obtained[110], is mainly due to the dominance of inertial impaction and Brownian motion for large micron and small submicron particles, respectively. It is noteworthy that without Brownian motion, the submicron particles do not preferentially deposit on any solid surface; as shown, their deposition efficiencies appear to be relatively low and independent on the variation of particle sizes (Figure 3.10c). As a consequence, from the analysis of Figure 3.10, the multiple blocks in staggered arrangement have a significant influence of particle deposition enhancement for both micron particles and ultrafine particles.

3.4.2. Effects of various longitudinal and transverse spacings

In the previous section we saw how multiple obstacles could provide a significant influence on the deposition efficiency of micron particles (10 μm $\leq d_p$ $\leq$ 15 μm) and ultrafine particles (1 nm $\leq d_p \leq$ 10 nm) on walls and obstructions.

We now move to the more specific categories of staggered arrangements and our goal is to evaluate whether the block-to-block spacing is sensitive to the particle deposition.

In this section, we investigate the effect of longitudinal spacings (L/B) and transverse spacings (T/B), respectively, on particle deposition in a channel flow over two blocks. In the case of different longitudinal spacings, the position of the block 1 (Figure 3.1) is fixed at $x = 10$ and $y = 1.5$, while the range of different longitudinal locations of block 2 at $y = 2.5$ are chosen as $11.25 \le x \le 14$ corresponding to the parameter range $1.25 \le L/B \le 4$.

Figure 3.11 shows the variation of the total deposition efficiency with L/B for different particle sizes at $T/B = 1$. It is evident that the total deposition efficiency of $d_p = 15$ μm varies significantly with L/B in the range $1.25 \le L/B \le 2$ and exhibits a maximum at $L/B = 1.5$. In order to understand this peculiar behavior, images of instantaneous particle distributions for $d_p = 15$ μm at $L/B =$
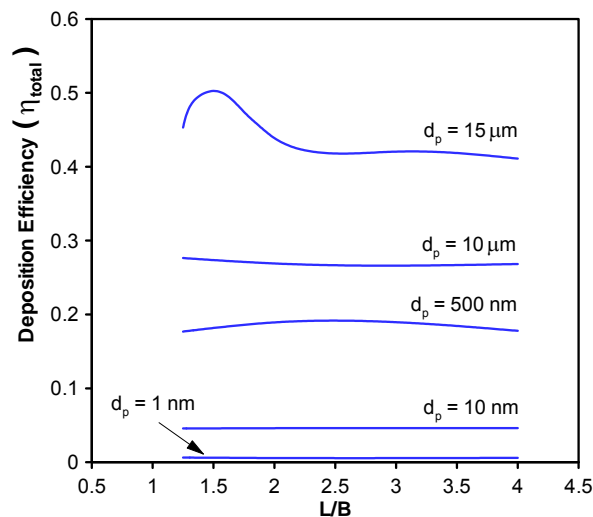

Figure 3.11. Variation of deposition efficiency on obstructions and walls with the longitudinal spacing between the centers of two blocks for different particle sizes at $T/B = 1$.

Figure 3.12. Instantaneous particle distribution in a channel with different values of: (a) L/B = 1.25; (b) L/B = 1.5; and (c) L/B = 4, for T/B = 1 and d_p = 15 μm. Images are captured at the time of the maximum streamwise velocity in one vortex shedding cycle (after 42,000 particles have been injected).

1.25, 1.5 and 4 as well as their corresponding particle deposition efficiencies on block 1 and 2 and walls are compared to each other in Figure 3.12. It is seen that the number of particles deposited on block 2 is increased as the longitudinal spacing slightly increases to where the maximum value of η_{total} is reached. The image in Figure 3.12 (a) shows more particles slipping through the interstitial space between the blocks than that in Figure 3.12 (b) because of the rapid increase in flow velocity between the blocks in Figure 3.12 (a). At L/B = 4 (Figure 3.12c), where the space between the blocks is large, particles pass through the bottom of block 2 due to gravity and hence the quantity of deposited particles is reduced. In the case of different transverse spacings, the parameter range $0 \leq T/B \leq 1$ is yielded by varying the transverse position of block 1 and 2, from y = 2 to 1.5 and y = 2 to 2.5, respectively. The position of
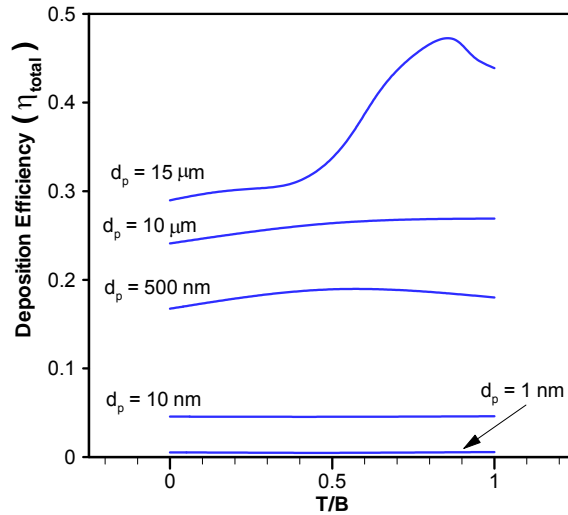
Figure 3.13. Variation of deposition efficiency on obstructions and walls with the transverse spacing between the centers of two blocks for different particle sizes at L/B = 2.
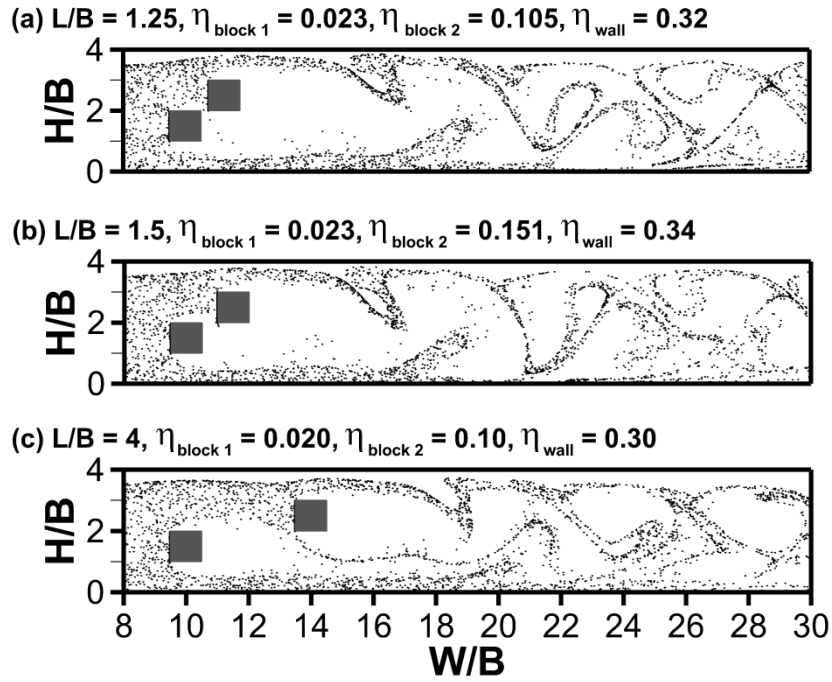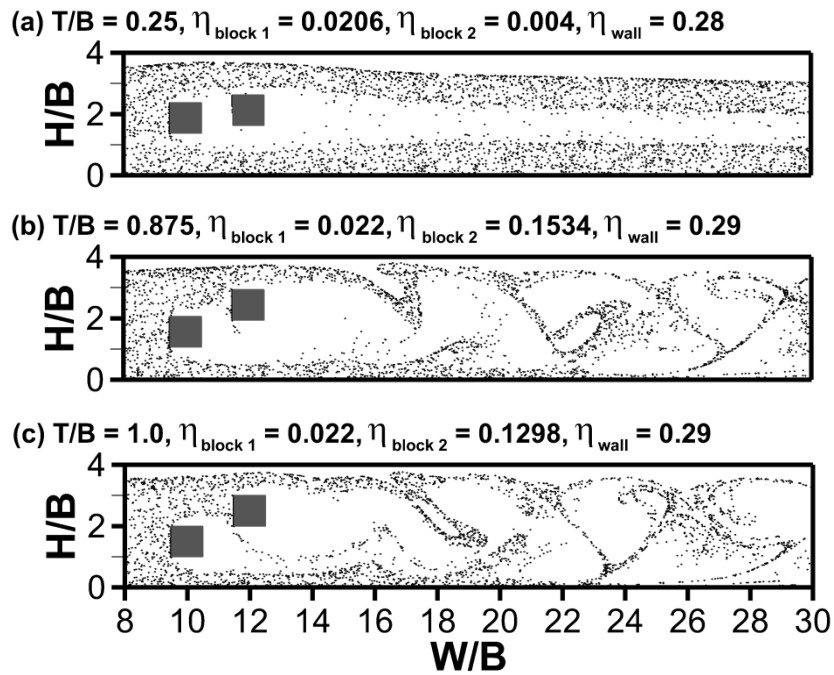

Figure 3.14. Instantaneous particle distribution in a channel with different values of: (a) $T/B = 0.25$; (b) $T/B = 0.875$; and (c) $L/B = 0.022$, for $L/B = 2$ and $d_p = 15$ μm. Images are captured at the time of the maximum streamwise velocity in one vortex shedding cycle (after 42,000 particles have been injected).

block 1 and 2 along the *x* direction is exactly the same as in Section 3.4.1. Figure 3.13 displays the variations of the total deposition efficiency versus *T*/*B* for different particle sizes at *L*/*B* = 2. Similar to the results reported in Figure 3.11, this pattern of variations shows further that the total deposition efficiency increases sharply at *T*/*B* ≅ 0.5 and its maximum occurs at *T*/*B* = 0.875.

Figure 3.14 also elucidates different patterns of particle distribution due to different transverse spacings. As the blocks are staggered from *T*/*B* = 0.25 to 0.875, deposition of particles on block 2 is dramatically increased. It is observed, however, that the number of particles trapped in block 2 is slightly reduced as the block is mostly immersed in the particle-laden flow (Figure 3.14 c). Overall, the analysis also defines the operating range where staggered blocks can be considered effectively in determining the level of particle deposition augmentation.

3.5. Conclusions

In this article, an incompressible lattice Boltzmann model is employed to investigate the transport of aerosol particles and their deposition efficiency in a two-dimensional channel flow around multiple square prisms in staggered arrangements. The validation results demonstrate that the proposed model is in better agreement with the data obtained from conventional computational techniques than that of the previously proposed LB model.

Qualitatively, the total particle deposition efficiency has the same functional dependency on the Stokes number (particle size) for different number of blocks placed in the channel. The results of this work illustrate that the particle deposition characteristics in the channel flow around staggered

blocks can be enhanced as the particle size increases in the micron scale range or decreases in the submicron scale range. These phenomena are due to the fact that inertial impaction and Brownian motion are the dominant mechanisms for the transport of micron and submicron particles, respectively. The study also examines the effect of block-to-block spacings on the deposition of aerosol particles by individually varying the longitudinal and transverse space between two blocks. It is found that for 15 μm particles, both longitudinal and transverse spacing not only influence the behavior of particle deposition but also yield maximum deposition efficiencies of particles. Overall, simulation results establish the range of operating obstacle parameters where deposition rates can be manipulated. Future work is recommended to extend the current investigation to include particle-particle interaction and the effect of particle motion on the fluid flow. This model will aid in examining the contribution of the effect of particle clouds on the particle deposition and distributions in the present configuration.

BIBLIOGRAPHY

1. Violi A, Yan S, Eddings EG, Sarofim F, Granata S, Faravelli T, Ranzi E. Experimental formulation and kinetic model for JP-8 surrogate mixtures. Combustion Sci Technol 2002 NOV-DEC;174(11-2):399-417.

2. Fisher EM, Pitz WJ, Curran HJ, Westbrook CK. Detailed chemical kinetic mechanisms for combustion of oxygenated fuels. Proceedings of the Combustion Institute 2000;28:1579-86.

3. Gail S, Thomson MJ, Sarathy SM, Syed SA, Dagaut P, Dievart P, Marchese AJ, Dryer FL. A wide-ranging kinetic modeling study of methyl butanoate combustion. Proceedings of the Combustion Institute 2007; 31:305-11.

4. Metcalfe WK, Dooley S, Curran HJ, Simmie JM, El-Nahas AM, Navarro MV. Experimental and modeling study of C5H10O2 ethyl and methyl esters. Journal of Physical Chemistry a 2007 MAY 17;111(19):4001-14.

5. Huynh LK, Violi A. Thermal decomposition of methyl butanoate: Ab initio study of a biodiesel fuel surrogate. J Org Chem 2008;73(1):94-101.

6. Westbrook CK, Pitz WJ, Curran HJ. Chemical kinetic modeling study of the effects of oxygenated hydrocarbons on soot emissions from diesel engines. Journal of Physical Chemistry a 2006;110(21):6912-22.

7. Dooley S, Curran HJ, Simmie JM. Autoignition measurements and a validated kinetic model for the biodiesel surrogate, methyl butanoate. Combust Flame 2008;153(1-2):2-32.

8. Lai JYW, Lin KC, Violi A. Biodiesel combustion: Advances in chemical kinetic modeling. Progress in Energy and Combustion Science 2011; 37(1):1-14.

9. Kohse-Hoinghaus K, Osswald P, Cool TA, Kasper T, Hansen N, Qi F, Westbrook CK, Westmoreland PR. Biofuel combustion chemistry: From ethanol to biodiesel. Angewandte Chemie-International Edition 2010;49 (21):3572-97.

10. Curran HJ, Gaffuri P, Pitz WJ, Westbrook CK. A comprehensive modeling study of iso-octane oxidation. Combust Flame 2002;129(3):253-80.

11. Barckholtz TA. Modeling the negative temperature coefficient in the low temperature oxidation of light alkanes. Abstracts of Papers of the American Chemical Society 2003;226:013-FUEL.

12. Farooq A, Davidson DF, Hanson RK, Huynh LK, Violi A. An experimental and computational study of methyl ester decomposition pathways using shock tubes. Proceedings of the Combustion Institute 2009;32:247-53.

13. Beatrice C, Bertoli C, Giacomo ND. New findings on combustion behavior of oxygenated synthetic diesel fuels. Combustion Sci Technol 1998;137 (1-6):31-50.

14. Yamane K, Kawasaki K, Sone K, Hara T, Prakoso T. Oxidation stability of biodiesel and its effects on diesel combustion and emission characteristics. International Journal of Engine Research 2007 JUN; 8(3):307-19.

15. Haas MJ, Scott KM, Alleman TL, McCormick RL. Engine performance of biodiesel fuel prepared from soybean soapstock: A high quality renewable fuel produced from a waste feedstock. Energy Fuels 2001 SEP-OCT;15(5):1207-12.

16. Osmont A, Yahyaoui M, Catoire L, Goekalp I, Swihart MT. Thermochemistry of C-O, (CO)-O, and (CO)-C bond breaking in fatty acid methyl esters. Combust Flame 2008 OCT;155(1-2):334-42.

17. Mueller CJ, Pickett LM, Siebers DL, Pitz WJ, Westbrook CK, Martin GC, Effects of oxygenates on soot processes in DI diesel engines: Experiments and numerical simulations, Tech. rep., Society of Automotive Engineers INC. 2003.

18. El-Nahas AM, Navarro MV, Simmie JM, Bozzelli JW, Curran HJ, Dooley S, Metcalfe W. Enthalpies of formation, bond dissociation energies and reaction paths for the decomposition of model biofuels: Ethyl propanoate and methyl butanoate. Journal of Physical Chemistry a 2007 MAY 17; 111(19):3727-39.

19. Curran HJ, Gaffuri P, Pitz WJ, Westbrook CK. A comprehensive modeling study of n-heptane oxidation. Combust Flame 1998 JUL;114(1-2):149-77.

20. Dagaut P, Ali KH. Kinetics of oxidation of a LPG blend mixture in a JSR: Experimental and modeling study. Fuel 2003 MAR;82(5):475-80.

21. Horning DC, Davidson DF, Hanson RK. Study of the high-temperature autoignition of n-alkane/O-2/Ar mixtures. J Propul Power 2002 MAR-APR; 18(2):363-71.

22. Gardiner WC. Combustion Chemistry. New York: Springer-Verlag. 1984.

23. Kee RJ, Rupley FM, Miller JA, Coltrin ME, Grcar JF, Meeks E, et al. CHEMKIN Release 4.1, Reaction Design, San Diego, CA 2006.

24. Gail S, Sarathy SM, Thomson MJ, Dievart P, Dagaut P. Experimental and chemical kinetic modeling study of small methyl esters oxidation: Methyl (E)-2-butenoate and methyl butanoate. Combust Flame 2008 DEC; 155(4):635-50.

25. Hoffman SR, Abraham J. A comparative study of n-heptane, methyl decanoate, and dimethyl ether combustion characteristics under homogeneous-charge compression-ignition engine conditions. Fuel 2009 JUN;88(6):1099-108.

26. Walton SM, Wooldridge MS, Westbrook CK. An experimental investigation of structural effects on the auto-ignition properties of two C-5 esters. Proceedings of the Combustion Institute 2009;32:255-62.

27. Hakka MH, Glaude PA, Herbinet O, Battin-Leclerc F. Experimental study of the oxidation of large surrogates for diesel and biodiesel fuels. Combust Flame 2009;156(11):2129-44.

28. Lin KC, Lai JYW, Violi A, Insights into the differences in oxidation pathways of methyl butanoate and n-Butane, in: Proceedings of the 6th U.S. National Combustion Meeting, 2009.

29. Herbinet O, Pitz WJ, Westbrook CK. Detailed chemical kinetic oxidation mechanism for a biodiesel surrogate. Combust Flame 2008 AUG; 154(3): 507-28.

30. Choi SUS. Enhancing thermal conductivity of fluids with nanoparticles. In: Siginer DA, Wang HP (Eds.). Developments and Applications of NonNewtonian Flows, vol. FED-231/MD-66. 1995 ASME, Berlin; 99–105.

31. Choi SUS, Zhang ZG, Keblinski P.. Nanofluids. Encyclopedia of Nanoscience and Nanotechnology 6 2004; 757–773.

32. Murshed SMS, Leong KC, Yang C. Thermophysical and electrokinetic properties of nanofluids - A critical review. Appl Therm Eng 2008 DEC; 28 (17-18):2109-25.

33. Eastman JA, Choi US, Li S, Thompson LJ, Lee S. Enhanced thermal conductivity through the development of nanofluids. Nanophase and Nanocomposite Materials Ii 1997;457:3-11.

34. Xie HQ, Wang JC, Xi TG, Liu Y, Ai F, Wu QR. Thermal conductivity enhancement of suspensions containing nanosized alumina particles. J Appl Phys 2002 APR 1;91(7):4568-72.

35. Patel HE, Das SK, Sundararajan T, Sreekumaran Nair A, George B, Pradeep T. Thermal conductivities of naked and monolayer protected metal nanoparticle based nanofluids: Manifestation of anomalous enhancement and chemical effects. Appl Phys Lett 2003 OCT 6;83(14): 2931-3.

36. Xu J, Yu B. A new model for heat conduction of nanofluids based on fractal distributions of nanoparticles (vol 39, pg 4486, 2006). Journal of Physics D-Applied Physics 2008 JUL 7;41(13):139801.

37. Putra N, Roetzel W, Das SK. Natural convection of nano-fluids. Heat and Mass Transfer 2003 SEP;39(8-9):775-84.

38. Kim J, Kang YT, Choi CK. Analysis of convective instability and heat transfer characteristics of nanofluids. Phys Fluids 2004 JUL; 16(7): 2395-401.

39. Wen DS, Ding YL. Experimental investigation into convective heat transfer of nanofluids at the entrance region under laminar flow conditions. Int J Heat Mass Transfer 2004 NOV;47(24):5181-8.

40. Jung JY, Oh HS, Kwak HY. Forced convective heat transfer of nanofluids in microchannels. In: Proceedings of ASME Int. Mech. Eng. Congress and Exposition (IMECE 2006), Chicago, USA, 2006.

41. Wen D, Ding Y. Effect of particle migration on heat in suspensions of nanoparticles flowing through minichannels. Microfluid. Nanofluid. 1(2005);183–189.

42. Mirmasoumi S, Behzadmehr A. Effect of nanoparticles mean diameter on mixed convection heat transfer of a nanofluid in a horizontal tube. Int J Heat Fluid Flow 2008 APR;29(2):557-66.

43. Khanafer K, Vafai K, Lightstone M. Buoyancy-driven heat transfer enhancement in a two-dimensional enclosure utilizing nanofluids. Int J Heat Mass Transfer 2003 SEP;46(19):3639-53.

44. Tiwari RK, Das MK. Heat transfer augmentation in a two-sided lid-driven differentially heated square cavity utilizing nanofluids. Int J Heat Mass Transfer 2007 MAY;50(9-10):2002-18.

45. Abu-Nada E. Application of nanofluids for heat transfer enhancement of separated flows encountered in a backward facing step. Int J Heat Fluid Flow 2008 FEB;29(1):242-9.

46. Akbari M, Behzadmehr A, Shahraki F. Fully developed mixed convection in horizontal and inclined tubes with uniform heat flux using nanofluid. Int J Heat Fluid Flow 2008 APR;29(2):545-56.

47. Ho CJ, Chen MW, Li ZW. Numerical simulation of natural convection of nanofluid in a square enclosure: Effects due to uncertainties of viscosity and thermal conductivity. Int J Heat Mass Transfer 2008 AUG; 51(17-18): 4506-16.

48. Abu-Nada E, Oztop HF. Effects of inclination angle on natural convection in enclosures filled with Cu-water nanofluid. Int J Heat Fluid Flow 2009

AUG;30(4):669-78.

49. Hwang KS, Lee J, Jang SP. Buoyancy-driven heat transfer of water-based Al2O3 nanofluids in a rectangular cavity. Int J Heat Mass Transfer 2007SEP;50(19-20):4003-10.

50. Li CH, Peterson GP. Experimental investigation of temperature and volume fraction variations on the effective thermal conductivity of nanoparticle suspensions (nanofluids). J Appl Phys 2006 APR 15; 99(8): 084314.

51. Jang SP, Lee J, Hwang KS, Choi SUS. Particle concentration and tube size dependence of viscosities of Al2O3-water nanofluids flowing through micro and minitubes. Appl Phys Lett 2007 DEC 10;91(24):243112.

52. Hamilton RL, Crosser OK. Thermal conductivity of heterogeneous 2-component systems. Industrial & Engineering Chemistry Fundamentals 1962;1(3):187,&.

53. Lee SL. Weighting function scheme and its application on multi-dimensional conservation equations. Int J Heat Mass Transfer 1989 NOV;32 (11):2065-73.

54. Lee SL. A strongly implicit solver for 2-dimensional elliptic differential equations. Numerical Heat Transfer Part B-Fundamentals 1989;16(2): 161-78.

55. Lee SL, Tzong RY. Artificial pressure for pressure-linked equation. Int J Heat Mass Transfer 1992 OCT;35(10):2705-16.

56. Davis GD. Natural-convection of air in a square cavity - a bench-mark numerical-solution. Int J Numer Methods Fluids 1983;3(3):249-64.

57. Markatos NC, Pericleous KA. Laminar and turbulent natural-convection in an enclosed cavity. Int J Heat Mass Transfer 1984;27(5):755-72.

58. Hadjisophocleous GV, Sousa ACM, Venart JES. Prediction of transient natural-convection in enclosures of arbitrary geometry using a nonorthogonal numericalmodel. Numerical Heat Transfer 1988;13(3): 373-92.

59. Ho CJ, Liu WK, Chang YS, Lin CC. Natural convection heat transfer of alumina-water nanofluid in vertical square enclosures: An experimental study. International Journal of Thermal Sciences 2010 AUG; 49(8): 1345-53.

60. Yu KF, Lau KS, Chan CK. Numerical simulation of gas-particle flow in a single-side backward-facing step flow. J Comput Appl Math 2004 FEB 1; 163(1):319-31.

61. Kosinski P, Kosinska A, Hoffmann AC. Simulation of solid particles behaviour in a driven cavity flow. Powder Technol 2009 APR 24; 191(3): 327-39.

62. Yao J, Zhao Y, Hu G, Fan J, Cen K. Numerical simulation of particle dispersion in the wake of a circular cylinder. Aerosol Science and Technology 2009;43(2):174-87.

63. Chen S, Doolen GD. Lattice boltzmann method for fluid flows. Annu Rev Fluid Mech 1998;30:329-64.

64. Aidun CK, Clausen JR. Lattice-boltzmann method for complex flows. Annu Rev Fluid Mech 2010;42:439-72.

65. Chen HD, Kandasamy S, Orszag S, Shock R, Succi S, Yakhot V. Extended boltzmann kinetic equation for turbulent flows. Science 2003 AUG 1;301 (5633):633-6.

66. Al-Jahmany YY, Brenner G, Brunn PO. Comparative study of lattice boltzmann and finite volume methods for the simulation of laminar flow through a 4 : 1 planar contraction. Int J Numer Methods Fluids 2004 NOV 30;46(9):903-20.

67. Al-Zoubi A, Brenner G. Comparative study of thermal flows with different finite volume and lattice boltzmann schemes. Int J Mod Phys C 2004 FEB;15(2):307-19.

68. He XY, Doolen GD, Clark T. Comparison of the lattice Boltzmann method and the artificial compressibility method for Navier-Stokes equations. J Comput Phys 2002 JUL 1;179(2):439-51.

69. Martinez DO, Matthaeus WH, Chen S, Montgomery DC. Comparison of spectral method and lattice Boltzmann simulations of 2-dimensional hydrodynamics. Phys Fluids 1994 MAR;6(3):1285-98.

70. Breuer M, Bernsdorf J, Zeiser T, Durst F. Accurate computations of the laminar flow past a square cylinder based on two different methods: Lattice-Boltzmann and finite-volume. Int J Heat Fluid Flow 2000 APR; 21(2):186-96.

71. Guo WB, Wang NC, Shi BC, Guo ZL. Lattice-BGK simulation of a two-dimensional channel flow around a square cylinder. Chin Phys 2003 JAN; 12(1):67-74.

72. Liu Y, So RMC, Cui ZX. Bluff body flow simulation using lattice Boltzmann equation with multiple relaxation time. Comput Fluids 2006 SEP-NOV; 35(8-9):951-6.

73. Guo Z, Liu H, Luo L, Xu K. A comparative study of the LBE and GKS methods for 2D near incompressible laminar flows. J Comput Phys 2008

MAY 1;227(10):4955-76.

74. Surmas R, dos Santos LOE, Philippi PC. Lattice Boltzmann simulation of the flow interference in bluff body wakes. Future Generation Comput Syst 2004 AUG;20(6):951-8.

75. Agrawal A, Djenidi L, Antonia RA. Investigation of flow around a pair of side-by-side square cylinders using the lattice Boltzmann method. Comput Fluids 2006 DEC;35(10):1093-107.

76. Sumner D. Two circular cylinders in cross-flow: A review. J Fluids Struct 2010 AUG;26(6):849-99.

77. Niu JL, Zhu ZJ. Numerical study of three-dimensional flows around two identical square cylinders in staggered arrangements. Phys Fluids 2006 APR;18(4):044106.

78. Sarkar S, Dalal A, Biswas G. Mixed convective heat transfer from two identical square cylinders in cross flow at Re=100. Int J Heat Mass Transfer 2010 JUN;53(13-14):2628-42.

79. Berbish NS. Heat transfer and flow behavior around four staggered elliptic cylinders in cross flow. Heat Mass Transf 2011 MAR; 47(3): 287-300.

80. Fessler JR, Eaton JK. Turbulence modification by particles in a backw-ard-facing step flow. J Fluid Mech 1999 SEP 10;394:97-117.

81. Lazaro BJ, Lasheras JC. Particle dispersion in the developing free shear-layer .1. unforced flow. J Fluid Mech 1992 FEB;235:143-78.

82. Longmire EK, Eaton JK. Structure of a particle-laden round jet. J Fluid Mech 1992 MAR;236:217-57.

83. Eaton JK, Fessler JR. Preferential concentration of particles by turbu-lence. Int J Multiphase Flow 1994 AUG;20:169-209.

84. Wen F, Kamalu N, Chung JN, Crowe CT, Troutt TR. Particle dispersion by vortex structures in plane mixing layers. J Fluids Eng-Trans ASME 1992 DEC;114(4):657-66.

85. Loehden D, Walsh PM, Sayre AN, Beer JM, Sarofim AF. Generation and deposition of fly-ash in the combustion of pulverized coal. J Inst Energy 1989 JUN;62(451):119-27.

86. Kasper G, Schollmeier S, Meyer J, Hoferer J. The collection efficiency of a particle-loaded single filter fiber. J Aerosol Sci 2009 DEC;40(12): 993-1009.

87. Heim M, Wengeler R, Nirschl H, Kasper G. Particle deposition from

aerosol flow inside a T-shaped micro-mixer. J Micromech Microengineering 2006 JAN;16(1):70-6.

88. Li A, Ahmadi G, Bayer RG, Gaynes MA. Aerosol-particle deposition in an obstructed turbulent duct flow. J Aerosol Sci 1994 JAN;25(1):91-112.

89. Li X, Zhou H, Cen K. Influences of various vortex structures on the dispersion and deposition of small ash particles. Fuel 2008 JUN; 87(7):1379-82.

90. Haugen NEL, Kragset S. Particle impaction on a cylinder in a crossflow as function of stokes and reynolds numbers. J Fluid Mech 2010 OCT 25; 661:239-61.

91. Brandon DJ, Aggarwal SK. A numerical investigation of particle deposition on a square cylinder placed in a channel flow. Aerosol Science and Technology 2001 APR;34(4):340-52.

92. Salmanzadeh M, Rahnama M, Ahmadi G. Particle transport and deposition in a duct flow with a rectangular obstruction. Particul Sci Technol 2007;25(5):401-12.

93. Jafari S, Salmanzadeh M, Rahnama M, Ahmadi G. Investigation of particle dispersion and deposition in a channel with a square cylinder obstruction using the lattice boltzmann method. J Aerosol Sci 2010; 41 (2):198-206.

94. Moshfegh A, Farhadi M, Shams M. Numerical simulation of particle dispersion and deposition in channel flow over two square cylinders in tandem. J Dispersion Sci Technol 2010;31(6):852-9.

95. He XY, Luo LS. Lattice Boltzmann model for the incompressible Navier Stokes equation. Journal of Statistical Physics 1997 AUG;88(3-4):927-44.

96. Tang GH, Tao WQ, He YL. Thermal boundary condition for the thermal lattice boltzmann equation. Physical Review E 2005 JUL;72(1):016703.

97. Zou QS, He XY. On pressure and velocity boundary conditions for the lattice boltzmann BGK model. Phys Fluids 1997 JUN;9(6):1591-8.

98. Reist PC. Aerosol Science and Technology, 2nd ed. 1993 New York: McGraw-Hill.

99. Friedlander SK. Smoke Dust and Haze, 2nd ed. 2000 Oxford, UK: Oxford University Press.

100. Saffman PG. Lift on a small sphere in a slow shear flow. J Fluid Mech 1965;22:385.

101. Saffman PG. Correction. J Fluid Mech 1968;31:624.

102. Li A, Ahmadi G. Dispersion and deposition of spherical-particles from point sources in a turbulent channel flow. Aerosol Sci Technol 1992 MAY; 16(4):209-26.

103. Zare A, Abouali O, Ahmadi G. Computational investigation of airflow, shock wave and nanoparticle separation in supersonic and hypersonic impactors. J Aerosol Sci 2007 OCT;38(10):1015-30.

104. Li A, Ahmadi G. Deposition of aerosols on surfaces in a turbulent channel flow. Int J Eng Sci 1993 MAR;31(3):435-51.

105. Akbar MK, Rahman M, Ghiaasiaan SM. Particle transport in a small square enclosure in laminar natural convection. J Aerosol Sci 2009 SEP; 40(9):747-61.

106. Turki S, Abbassi H, Ben Nasrallah S. Two-dimensional laminar fluid flow and heat transfer in a channel with a built-in heated square cylinder. International Journal of Thermal Sciences 2003 DEC;42(12):1105-13.

107. Sosnowski TR, Moskal A, Gradon L. Mechanims of aerosol particle deposition in the oro-pharynx under non-steady airflow. Ann Occup Hyg 2007 JAN;51(1):19-25.

108. Guha A. Transport and deposition of particles in turbulent and laminar flow. Annu Rev Fluid Mech 2008;40:311-41.

109. Hinds WC Aerosol Technology: Properties, Behavior and Measurement of Airborne Particles. 1999 New York: Wiley.

110. Strom H, Andersson B. Simulations of trapping of diesel and gasoline particulate matter in flow-through devices. Topics in Catalysis 2009 DEC; 52(13-20):2047-51.